

---

# Temporal characterization of harmonic radiation generated by intense laser–plasma interaction

Yutaka Nomura

---



München 2008



---

# **Temporal characterization of harmonic radiation generated by intense laser–plasma interaction**

**Yutaka Nomura**

---

Dissertation  
an der Fakultät für Physik  
der Ludwig–Maximilians–Universität  
München

vorgelegt von  
Yutaka Nomura  
aus Chiba, Japan

München, den 03 April 2008

Erstgutachter: Prof. Dr. Ferenc Krausz

Zweitgutachter: Prof. Dr. Dietrich Habs

Tag der mündlichen Prüfung: 04 Juni 2008

# Abstract

Attosecond physics has become one of the most thriving field of science over the last decade. Although high-order harmonic generation from gaseous media is widely used as the source of attosecond pulses, a demand for more intense coherent extreme ultraviolet (XUV) and soft x-ray (SXR) radiation sources is growing. The process of high-order harmonic generation from plasma surfaces has attracted a strong interest as a promising candidate to meet this demand. Despite many theoretical predictions of the possibilities to generate intense attosecond pulses, experimental verifications are yet to come.

The main theme of this thesis is to characterize the temporal structure of the harmonics generated from plasma surfaces. To achieve this goal, several preparatory experiments are made first. The contrast of the laser pulse is one of the most critical parameters for the harmonic generation process and its improvement is demonstrated by using a plasma mirror. The properties of the generated harmonics are studied thoroughly to find the optimal condition for temporal characterization. These experiments provide the groundwork for the autocorrelation measurements of the pulse train. To characterize the temporal structure of the generated harmonics, the technique of the volume autocorrelation using two-photon ionization of helium is applied. The measured autocorrelation traces reveal attosecond structures within the XUV radiation generated from the plasma surfaces for the first time.

The observation of attosecond structures prove the potential of this harmonic generation process as a source of attosecond pulses. The process holds a promise to generate attosecond pulses with unprecedented intensities, which will open up a new regime of attosecond physics.



# Zusammenfassung

Die Attosekundenphysik hat sich im letzten Jahrzehnt zu einem der am schnellsten wachsenden Felder der Physik entwickelt. Obwohl die Erzeugung von hohen Harmonischen in Gasen in vielen Laboren Anwendung findet, wächst der Bedarf an intensiveren kohärenten Strahlungsquellen im extremen Ultraviolett (XUV) und weichen Röntgenbereich (SXR). Die Erzeugung von hohen Harmonischen an Plasma-Oberflächen ist ein vielversprechender Kandidat, um diese Anforderungen zu erfüllen. Obwohl die Möglichkeiten der Erzeugung von Attosekunden-Pulsen an Oberflächen in der Theorie gut untersucht und verstanden sind, steht der experimentelle Nachweis dieser Pulse noch aus.

Das Hauptthema dieser Arbeit ist eben dieser Nachweis einer zeitlichen Struktur in der Harmonischen Emission von Plasma-Oberflächen und deren Charakterisierung. Um dieses Ziel zu erreichen, wurden zunächst einige vorbereitende Experimente durchgeführt. Der Kontrast der verwendeten Laserpulse stellt einen der wichtigsten Parameter zur Erzeugung von Oberflächenharmonischen dar, und seine Verbesserung mittels eines Plasma-Spiegels wird in dieser Arbeit dargestellt. Die Eigenschaften der erzeugten Harmonischen werden gründlich untersucht, um die bestmöglichen experimentellen Bedingungen für die zeitliche Charakterisierung zu finden. Diese Experimente stellen die Grundlage für die Autokorrelationsmessungen des Pulszuges dar. Um die zeitliche Struktur der erzeugten Harmonischen zu messen, wird die Methode der Volumenautokorrelation angewendet. Als nichtlineares Medium dient die Zwei-Photonen-Ionisation von Helium. Die in dieser Arbeit gezeigten Autokorrelationskurven zeigen zum ersten mal Attosekunden-Strukturen in der XUV-Emission von Plasma-Oberflächen.

Der Nachweis dieser Strukturen zeigt, dass diese Methode zur Erzeugung von hohen Harmonischen das Potential besitzt als Quelle für Attosekunden-Pulse zu dienen. Darüber hinaus verspricht diese Quelle die Erzeugung von Attosekunden-Pulsen mit noch nie dagewesenen Intensitäten, die ein ganz neues Feld der Attosekundenphysik zugänglich machen.





# Contents

<b>Abstract</b>	<b>v</b>
<b>1 Introduction</b>	<b>1</b>
1.1 Intense attosecond pulse generation	1
1.2 High-intensity laser–plasma interaction	3
1.3 Outline of the thesis	4
<b>2 High-order harmonic generation from plasma–vacuum interface</b>	<b>7</b>
2.1 Introduction	7
2.2 Harmonic generation mechanisms	9
2.2.1 Relativistic oscillating mirror	9
2.2.2 Coherent wake emission	11
2.3 Route to intense attosecond pulses	12
2.3.1 Generation of a train of attosecond pulses	13
2.3.2 Generation of isolated attosecond pulses	13
2.4 Particle-in-cell simulation	17
<b>3 Plasma mirror with sub-10-fs pulses</b>	<b>21</b>
3.1 Plasma mirror	21
3.1.1 Background	21
3.1.2 Principle	23
3.2 Experimental configuration	23
3.2.1 Laser system	23
3.2.2 Experimental setup	24
3.3 Reflectivity of the plasma mirror	25
3.4 Refocusability of the reflected beam	29
3.5 Time-resolved reflectivity measurement with third-order correlation	31
3.6 Summary	35
<b>4 Experimental investigations of HHG from plasma–vacuum interface</b>	<b>37</b>
4.1 Experimental configuration	37
4.1.1 Laser system	37
4.1.2 Experimental chamber	39

4.1.3	Grazing-incidence spectrometer . . . . .	40
4.2	Spectral properties and selection . . . . .	43
4.2.1	Spectral selection using various filters . . . . .	43
4.2.2	Comparison of various targets . . . . .	44
4.2.3	Suppression of infrared . . . . .	48
4.3	Spatial profile . . . . .	50
4.4	Efficiency . . . . .	53
4.5	Summary . . . . .	56
<b>5</b>	<b>Volume autocorrelation of harmonics by two-photon ionization of helium</b>	<b>59</b>
5.1	Temporal characterization of XUV radiation . . . . .	59
5.1.1	Attosecond pulse characterization techniques . . . . .	59
5.1.2	Volume autocorrelation . . . . .	60
5.2	Experimental setup . . . . .	62
5.2.1	General setup . . . . .	62
5.2.2	Focus property in the interaction volume . . . . .	64
5.2.3	Time-of-flight setup . . . . .	65
5.3	Two-photon ionization of helium . . . . .	67
5.4	Coarse autocorrelation measurement . . . . .	71
5.5	Fine autocorrelation measurement . . . . .	74
5.6	Summary . . . . .	79
<b>6</b>	<b>Conclusions and outlook</b>	<b>81</b>
<b>A</b>	<b>Useful formulas</b>	<b>85</b>
A.1	Values related to Gaussian beam . . . . .	85
A.1.1	The Full Width Half Maximum . . . . .	85
A.1.2	Peak intensity and average intensity . . . . .	86
A.1.3	The RMS radius . . . . .	86
A.2	Second-order interferometric autocorrelation . . . . .	87
<b>B</b>	<b>Simulation of the focus from the split mirror at oblique incidence</b>	<b>89</b>
	<b>Bibliography</b>	<b>93</b>
	<b>Acknowledgments</b>	<b>105</b>
	<b>Curriculum Vitae</b>	<b>107</b>

# Chapter 1

## Introduction

### 1.1 Intense attosecond pulse generation

The generation of attosecond pulses [1] has opened up a new realm of physics, which became one of the most exciting field of science, ‘attosecond physics’ [2]. The pulses with unprecedented duration of a few hundred attoseconds ( $1 \text{ as} = 10^{-18} \text{ s}$ ) have enabled the time-resolved observation of many ultrafast phenomena. In fact, it has been demonstrated that these attosecond pulses can be exploited to measure the electric field of a light pulse [3], to time-resolve the electron tunneling process [4], and to observe the electron transport effect near the surface of a metal [5].

The generation of attosecond pulses to date were achieved through the process of high-order harmonic generation (HHG) in atomic media [6, 7]. The idea of ultrashort pulse generation comes from a technique of Fourier synthesis [8]. When a comb of equidistant frequencies is generated in the spectral domain with controlled relative phases, it leads to a train of sub-cycle pulses, which can be as short as a few hundred attoseconds. The process of gas HHG was considered to be a very promising candidate for this method [9, 10], and theories predicted that the generation of attosecond pulse trains is indeed possible [11]. It was also predicted that extracting a single attosecond pulse from a train is in principle possible by manipulating the polarization of the incident pulse [12]. On the other hand, more straightforward way of generating single attosecond pulses by using few-cycle pulses and selecting highest harmonic region was also proposed [13, 14]. Experimentally, both the generation of a train of attosecond pulses [15, 16, 17] as well as an isolated attosecond pulse [1, 18, 19] are successfully demonstrated.

If there is a problem in the process of gas HHG, that is its low conversion efficiency from the incident field into the extreme ultraviolet (XUV) radiation necessary for synthesizing attosecond pulses. To date, the generated attosecond pulses are not intense enough to allow autocorrelation or XUV-pump–XUV-probe measurements. In spite of many studies to improve the harmonic generation efficiency [20, 21, 22, 23], the highest conversion efficiency into XUV is approximately  $\sim 10^{-5}$  at 30 nm [24] and  $\sim 10^{-7}$  at 13 nm region [25, 26]. Increasing the intensity of the incident field leads to the ionization of the media and results in reduced harmonic generation efficiency. Therefore, the XUV output is limited by the conversion efficiency and the usable intensity.

From this reason, another approach to generate high-order harmonics from plasma surfaces started to draw special attention as a potential source of intense attosecond pulses [27]. The principle concept of this method is illustrated in Fig. 1.1. An intense laser pulse is focused onto the surface of a solid target, and generates a plasma there. From the interaction with the plasma, the reflected pulse gets modulated and gains high-frequency components. A certain part of these high-frequency components can be extracted with an appropriate filter to produce an isolated attosecond pulse or a train of attosecond pulses. The main advantage of this process is that plasma media allows much higher intensity than atomic media. In other words, the XUV output is not limited by the usable intensity of the incident field. Furthermore, it is predicted that higher incident intensity will lead to even higher conversion efficiency.

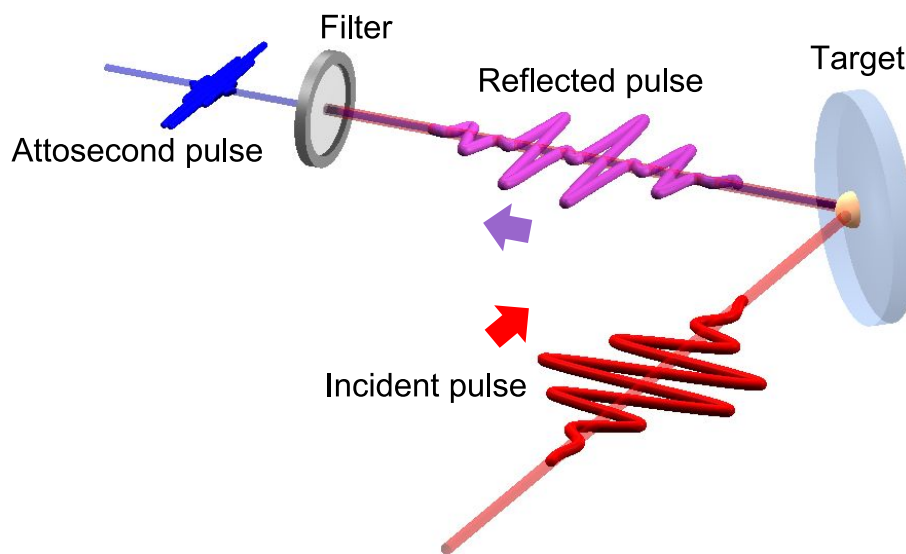


**Figure 1.1:** Scheme of attosecond pulse generation from solid surface. An intense laser pulse is focused onto a solid target and generates a plasma on the surface. Through the interaction with the plasma, the reflected pulse gets highly modulated. Attosecond pulses can be extracted with an appropriate filter.

Many experimental and theoretical studies were made over the past decade [28, 29, 30, 31, 32, 33, 34]. While theoretical studies have predicted many fascinating possibilities of this process, experimental studies are still at the investigation stage. One of the biggest challenges is to obtain laser pulses that satisfy the high requirements necessary for the interaction process; not only the required intensity is as high as  $\sim 10^{18} \text{W cm}^{-2}$  or more for the incident wavelength of  $\sim 800 \text{ nm}$  or  $\sim 1 \mu\text{m}$ , the incident pulse must be ‘clean’ so that it does not disturb the interaction surface prior to the arrival of the main pulse. This difficulty limited the scope of experimental work to simply generating harmonics, studying the effect of the laser parameters, and characterizing relatively simple properties such as spatial profiles. Despite many predictions of the possibility to generate attosecond pulses, no work has ever achieved observing the temporal structure of the generated harmonics.

In this thesis, the temporal characterization of the harmonics generated from the plasma surfaces is the main theme. This aims at observing the possible attosecond structures within the generated XUV radiation. A series of fundamental studies necessary for achieving the observation of the temporal structure will be also presented.

## 1.2 High-intensity laser–plasma interaction

The process of high-order harmonic generation from plasma surfaces (surface HHG) is based on the interaction between an intense electromagnetic field and a dense plasma. The physics of this process will be explained in Chapter 2. Here I will introduce several key parameters for describing this process.

An important parameter that characterizes the relativistic interaction is the normalized amplitude  $a$  of the vector potential, which is defined as

$$a = \frac{eA}{m_e c}, \quad (1.1)$$

where  $e$  is the charge of an electron,  $A$  the vector potential of the electromagnetic field,  $m_e$  the mass of an electron, and  $c$  the speed of light. When the value of this dimensionless parameter  $a$  reaches 1, the quiver velocity of electrons becomes comparable to the light speed. In other words, this parameter defines the relativistic threshold and  $a > 1$  means the interaction is relativistic, while  $a < 1$  means non-relativistic. The parameter  $a$  relates to the laser intensity  $I$  in a form

$$I\lambda^2 = 1.37 \times 10^{18} \text{ W cm}^{-2} \mu\text{m}^2 \times a^2, \quad (1.2)$$

where  $\lambda$  is the wavelength of the laser field. This means that intensity of  $I \sim 2 \times 10^{18} \text{ W cm}^{-2}$  is required to reach the relativistic regime at 800 nm.

Another important quantity is the plasma frequency  $\omega_p$  defined as

$$\omega_p = \sqrt{\frac{n_e e^2}{\epsilon_0 m_e}}, \quad (1.3)$$

where  $n_e$  is the electron number density and  $\epsilon_0$  is the vacuum permittivity. This is the frequency of the plasma oscillation and depends on the local density. The dispersion relation for electromagnetic waves within the plasma is affected by this value and expressed as

$$\omega^2 = \omega_p^2 + c^2 k^2, \quad (1.4)$$

where  $k$  is the wave vector. Since the value of  $k$  becomes imaginary for any frequency  $\omega$  below the plasma frequency  $\omega_p$ , a wave with a frequency  $\omega \leq \omega_p$  cannot penetrate into the plasma and will be reflected. The maximum density where a certain frequency can travel is called the critical density  $n_{\text{cr}}$  and expressed as

$$n_{\text{cr}} = \frac{\epsilon_0 m_e \omega^2}{e^2} \quad (1.5)$$

for a frequency  $\omega$ . In other words, the density of the plasma must be sufficiently high to reflect the incident pulse. For experiments of surface HHG, typically a solid target is used and thus a high plasma density is achieved that reflects the laser pulses.

A typical plasma density profile that the laser pulse interacts with is sketched in Fig. 1.2. Usually the target is ionized by the pedestal of the pulse, which leads to a hydrodynamic expansion of the plasma. This expansion is quantified by a characteristic distance called the scale length, which is defined as

$$L = n_e \left| \frac{dn_e}{dx} \right|. \quad (1.6)$$

If the density profile is exponential, it can be expressed as  $n_e(x) = n_{\max} e^{-x/L}$ . This value shows how ‘clean’ the plasma surface is, and turns out to be one of the most important factors in the process of surface HHG, because it directly affects the harmonic generation efficiency and other properties such as reflected beam profile. Therefore, the scale length should be kept approximately below  $L \sim 1\lambda$  to keep the interaction clean.

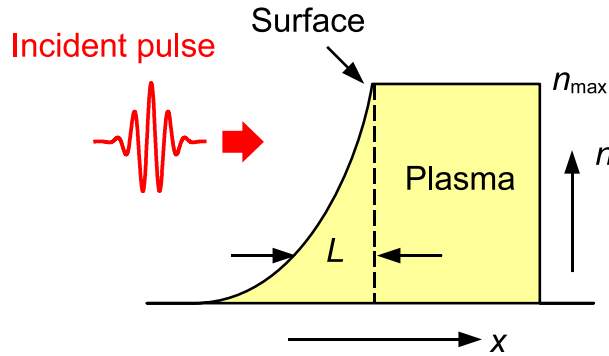


**Figure 1.2:** Typical plasma density profile the laser pulse interacts with. Because of the hydrodynamic expansion, the plasma has an exponential ramp in front, which is quantified by scale length  $L$ .

To keep the scale length short, the laser pulse must have a high contrast. The contrast of the laser pulse is defined by the ratio between the peak intensity and the prepulse/pedestal intensity. Since the damage threshold of typical dielectric material is  $\sim 10^{12} \text{ W cm}^{-2}$ , the contrast of the pulse with the focal intensity of  $\sim 10^{19} \text{ W cm}^{-2}$  must be kept as high as  $10^7$ , which is not a trivial task. Methods to improve the contrast will be discussed in Chapter 3.

### 1.3 Outline of the thesis

The central topic of this thesis is the experimental study of high-order harmonic generation from plasma-vacuum interface. The experiments were carried out in a very close collaboration with my colleague Rainer Hörlein. In fact, both of us were involved in all the experiments except for

the plasma mirror experiment presented in Chapter 3. While his work focuses on characterizing the properties of harmonic emission from different laser systems to find its potential as a source of coherent XUV radiation, my work aims at the characterization of the temporal structure of the generated harmonics.

In Chapter 2, the process of surface HHG will be introduced. After a brief overview of the history of surface HHG research, current understanding of the physical process of harmonic generation is presented. A feasibility of attosecond pulse generation from this process is also discussed by comparing it to the gas HHG process. The importance of the contrast is confirmed by numerical simulations.

In Chapter 3, improvement of the contrast—a critical parameter to the surface HHG process—is discussed. Experimentally, a plasma mirror was used to improve the contrast of sub-10-fs pulses. The properties of the plasma mirror are thoroughly characterized by measuring the throughput, refocusability, and time-resolved reflectivity.

In Chapter 4, the harmonics generated from plasma surfaces are characterized experimentally in the context of the applicational use in further experiments. Methods to select only the necessary spectral region is studied. The measurements of the beam profile and intensity of the reflected XUV beam prove the feasibility of temporal characterization experiment.

In Chapter 5, temporal characterization of the harmonics is presented. Several pulse characterization methods in the XUV region are reviewed first. After preparing the nonlinear detector by generating helium ions through the two-photon ionization process, the harmonics are characterized with the technique of volume autocorrelation. The temporal structure of the harmonics are deduced by analyzing the measured traces.

In Chapter 6, the experimental results are summarized and future prospects are discussed, including the ways to improve the current experimental setup and the possibility to generate isolated attosecond pulses.





# Chapter 2

## High-order harmonic generation from plasma–vacuum interface

In this chapter, high-order harmonic generation from plasma–vacuum interface is introduced. First, the history of surface HHG is reviewed and two different regimes for surface HHG are explained. Then, various possible methods to generate attosecond pulses are described. Finally, insight gained by so-called particle-in-cell simulation are presented.

### 2.1 Introduction

High-order harmonic generation from solid surfaces were first observed by using high-energy nanosecond pulses from CO<sub>2</sub> laser systems [35, 36, 37]. In these experiments, pulses with  $\sim 100$  J of energy at  $10.6 \mu\text{m}$  with  $\sim 1$  ns duration was focused to the intensity of  $\sim 10^{15} \text{ W cm}^{-2}$ , and harmonics up to 46th order ( $\sim 230$  nm) was observed. Theoretical studies attributed the harmonic generation mechanism to the nonlinear restoring force of the plasma and mode coupling into plasma oscillation [38, 39]. They also predicted that there would be a cutoff in the harmonic spectrum, whose position is determined by the plasma density.

Another decade was needed until the first observation of harmonics from plasma surfaces using femtosecond pulses produced from table-top Ti:sapphire laser systems [28, 40]. Typical parameters were  $\sim 100$  mJ of energy at  $\sim 800$  nm with  $\sim 100$  fs duration. Although the pulse energy was 3 orders of magnitude lower than that from CO<sub>2</sub> lasers, the pulse duration being shorter by 4 orders of magnitude allowed to achieve the intensity of  $\sim 10^{17} \text{ W cm}^{-2}$ . On the other hand, since the relativistic amplitude  $a$  scales as  $a^2 \propto I\lambda^2$ , higher intensity was compensated by the shorter wavelength, i.e., the value of  $a$  was comparable to that of CO<sub>2</sub> lasers. Nevertheless, it was shown that the surface harmonics can be generated with a much smaller, table-top laser systems.

In the meanwhile, numerical work with a particle-in-cell (PIC) simulation code found that there is no cutoff in the spectrum [41], which is in contrast with the prediction from previous studies. Harmonics beyond the predicted cutoff was also observed experimentally using a high-power, picosecond Nd:glass laser system with a focal intensity of  $\sim 10^{19} \text{ W cm}^{-2}$  at  $1053$  nm

[29]. A new theoretical model was proposed to explain these results, which is known as the oscillating-mirror model [30]. The model predicts that the harmonics are generated from fast moving reflective surface. This idea is first proposed by Bulanov *et al.* [42] and later formulated thoroughly [30, 43]. The appearance of the cutoff in the previous mode-coupling picture was attributed to low resolution of PIC simulation [41]. The oscillating-mirror model and the numerical simulation predicted that the harmonic generation could be extended well beyond the previously expected cutoff by increasing the laser intensity to the relativistic regime [41, 44]. This new prediction lead to growing interest into harmonic generation from plasma surfaces as a source of coherent XUV radiation.

Many experimental studies have followed. Several investigations have found that the harmonic generation process is strongly dependent on the plasma scale length [31, 45]. Harmonic generation efficiency was found to have an optimal scale length above zero, and then drop rapidly as the scale length increases [31, 46, 47]. In fact, improving the contrast of the incident laser pulse with a plasma mirror was found to be beneficial to the harmonic generation process [48]. Angular distribution of the generated harmonics was also studied. For picosecond laser pulses, the angular distribution was found to be near isotropic rather than specular [29, 49], which was attributed to surface rippling owing to the high ponderomotive pressure. On the other hand, XUV beam directed in the specular direction was observed for femtosecond laser pulses [45], where the interaction occurs faster than the plasma expands. The polarization dependence of the process was studied by several groups [29, 31, 45, 50, 51]. The harmonic generation efficiency was observed to be much lower for *s*-polarization when femtosecond pulses were used [31, 45], which was consistent with the prediction of the oscillating-mirror model [30]. When picosecond pulse was used, on the other hand, almost no difference was observed in harmonic generation efficiency by changing the polarization from *p* to *s* [29, 51], and the polarization of the generated XUV beam was also not consistent with the oscillating-mirror model. This discrepancy was explained by surface rippling and resulting polarization mixing [52]. Some studies have found that there were modulations in the harmonic spectra, which were attributed to the nonlinear oscillation of the plasma surface [53, 54].

Theoretical work has pursued the possibility of the harmonic generation process as a source of attosecond pulses. It was pointed out that the harmonics are inherently phase-locked and that leads to a train of attosecond pulses [55]. Another work proposed to focus a few-cycle pulses into a spot as small as the fundamental wavelength, which leads to generation of an isolated single attosecond pulse in a certain direction [56]. Analytical work similar to the oscillating-mirror model [57] has revealed that the harmonics spectra scales as a power law  $I_q \propto q^{-p}$ , where  $q$  is the harmonic order and  $p$  is a scaling parameter  $p \sim 2.5$ . From this slow power-law decay, they predicted that even a train of zeptosecond pulses could be produced. This scaling was verified by experimental observation of the harmonic spectrum matching the power law [33]. Even more precise model was developed by the same group [32] and the factor of power law was modified to  $p \sim 8/3$ . While this modification was minor and the experimental observation was still within the experimental error, this work predicted more important result: the cutoff position should scale as  $\sim \gamma^3$ , where  $\gamma$  is the relativistic  $\gamma$ -factor. This means that the highest harmonics generated from this process scales up very rapidly when the intensity of the incident field is increased. This scaling of the cutoff was also confirmed experimentally [58].

One more important thing to be mentioned is the recent study of harmonic generation in non-relativistic regime [34]. They found that there is a harmonic generation process efficient with non-relativistic intensity, which they named as coherent wake emission (CWE). The results predicted from their model are similar to the predictions from very early theoretical models, for example, the observation of the cutoff [38, 39]. Indeed, their model can be regarded as revisit to the old picture of mode coupling into plasma oscillation. An important thing is the new explanation they provided for the excitation mechanism of the plasma wave. Another important point is the clear indication of a mechanism different from the oscillating mirror [59, 60], which has been overlooked in the past.

## 2.2 Harmonic generation mechanisms

Harmonic generation mechanism from solid surfaces is categorized into two different regimes depending on the incident laser intensity: relativistic regime and non-relativistic regime. The former is known as relativistic oscillating mirror (ROM) model [30, 43], while the latter is named as coherent wake emission (CWE) [34].

### 2.2.1 Relativistic oscillating mirror

In this model, the source of harmonic generation is periodic Doppler shift from oscillating reflective surface of the plasma (Fig. 2.1). When the electromagnetic field is incident on a plasma surface, the electric field and/or the ponderomotive force pushes electrons back into the plasma. On the other hand, ions in the plasma do not move in femtosecond time scale, i.e., the ions are immobile if femtosecond pulses are incident. Thus, the electrons pushed back into the plasma by the incident pulse are pulled back mainly by the restoring force from the ions that remained at the original positions. This results in oscillation of the electrons, periodic to the frequency of the incident field. When the intensity of the incident pulse is high, the maximum velocity of the electrons approach the speed of light, and electron motion becomes relativistic. Since the incident electromagnetic pulse is reflected at the electron surface and this surface is moving relativistically, the incident field experiences an extreme Doppler shift, thus generating a frequency component much higher than the original.

The model predicts the polarization of the generated harmonics as well [30, 43]. The selection rules are summarized in Table 2.1. The selection rules can be derived by assuming that the collective motion of electrons is similar to figure-8 motion [61, 62] of a single electron in an electromagnetic wave. For  $p$ -polarized incident light, the electrons move in the plane of incidence. Both  $\omega_0$  motion and  $2\omega_0$  motion have component perpendicular to the surface—the direction without a symmetry—and thus all the harmonics are generated in  $p$ -polarization. For  $s$ -polarized incident light,  $\omega_0$  motion is parallel to the surface—the direction with a symmetry—and thus odd harmonics are generated in  $s$ -polarization. At the same time,  $2\omega_0$  motion has component perpendicular to the surface and thus all the harmonics of  $2\omega_0$  (all the even harmonics of  $\omega_0$ ) are generated in  $p$ -polarization. When circularly polarized pulse is used at normal incidence,

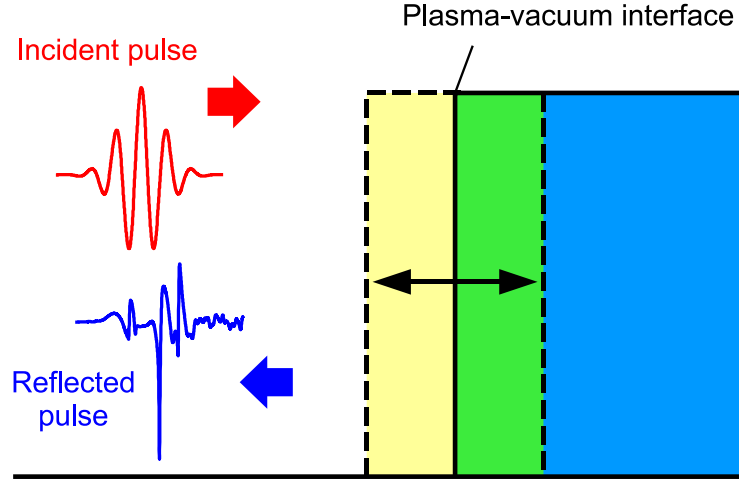


**Figure 2.1:** Schematic drawing of oscillating mirror. The electromagnetic field of the incident pulse drives the plasma–vacuum interface back and forth. The pulse experiences a huge Doppler shift upon the reflection on the oscillating surface, which leads to the generation of high frequency component.

no harmonic is generated because the ponderomotive force varies only slowly according to the envelope of the pulse and there is no fast oscillation of the electrons.

**Table 2.1:** Selection rules for polarization of harmonics.

Incident pulse	Odd harmonics	Even harmonics
<i>p</i> -polarization	<i>p</i>	<i>p</i>
<i>s</i> -polarization	<i>s</i>	<i>p</i>
circular polarization (normal)	—	—

To derive the scaling law and the cutoff position, it is necessary to follow a more precise model [32, 57]. Since the analytical treatment of the model is rather complicated, I will describe only the important points. Because of the relativistic Doppler effect, the fundamental frequency  $\omega_0$  is up-shifted to  $4\gamma_{\max}^2\omega_0$  [57], where  $\gamma_{\max}$  is the relativistic Lorentz factor of the oscillating plasma surface. There is another factor to be taken into account, and that is the effect of temporal confinement [32]. When the velocity of the plasma surface approaches the light speed, the value of  $\gamma$  forms a “ $\gamma$ -spike,” as shown in Fig. 2.2. The harmonics are generated efficiently when  $\gamma$ -parameter peaks up sharply, and the temporal width of this  $\gamma$ -spike scales as  $\Delta t \sim 1/\gamma_{\max}$ . In other words, the duration of the emitted pulse scales accordingly. Since this pulse is compressed by a factor  $4\gamma_{\max}^2$ , the time interval harmonics are emitted scales as  $\Delta t/4\gamma_{\max}^2 \sim 1/\gamma_{\max}^3$ . This means that there is a frequency component that scales as  $\sim \gamma_{\max}^3$ , which gives the scaling of the cutoff position. Full analytical treatment shows that the harmonic spectrum follows a scaling law of  $I_q \propto q^{-8/3}$ , where  $q$  is the harmonic order, and this scaling is satisfied up to a point  $q \sim \sqrt{8}\gamma^3$ ,

where it starts to deviate from the power law.

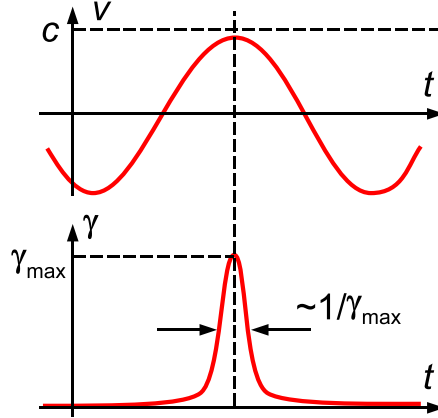


**Figure 2.2:** Motion of the plasma surface. As the velocity  $v$  approaches the light speed  $c$ , the  $\gamma$  parameter forms a sharp spike. The duration of the spike scales as  $\Delta t \sim 1/\gamma_{\max}$ .

### 2.2.2 Coherent wake emission

When the intensity of the incident laser field is not relativistic, the oscillating mirror does not generate harmonic efficiently and CWE [34] becomes dominant.

Figure 2.3 illustrates the process of CWE. The CWE is a process associated with plasma-wake oscillation. For this process to work, the incident electric field must have  $p$ -polarization. When a pulse is incident onto the surface of a plasma, the electric field of the pulse pulls electrons out from the plasma. Those electrons are driven back into the plasma by the same electric field and absorbed by the plasma—a process known as vacuum heating [63]. These electrons bunch in the plasma density gradient and constitutes a density wave inside the plasma. As the density wave travels, it triggers plasma oscillations in its wake. These plasma oscillations are converted back to electromagnetic waves at the point where the wave front of the wake turns around [64]. As the generated electromagnetic wave travels along the density gradient, it refracts and comes out of the plasma in the specular direction of the incident beam. Since this occurs within a fraction of a cycle, each wave generated is in a form of a pulse shorter than one cycle, possibly sub-femtosecond.

The CWE process has several interesting properties. As opposed to the ROM harmonic generation, this process is efficient down to the incident intensity of  $I\lambda^2 \sim 4 \times 10^{15} \text{ W cm}^{-2}$  [34], which corresponds to the normalized amplitude of  $a \sim 0.05$ . Therefore, CWE will be the dominant harmonic generation mechanism when the intensity is non-relativistic. Another important feature of CWE is that the harmonic spectra shows a clear cutoff at the maximum plasma frequency  $\omega_p$ , which is determined by the density of the plasma. The reason no harmonic is generated above  $\omega_p$  is because the generation process relies on the density wave in the plasma. This is in contrast with the spectra of ROM harmonics, where it shows a slow roll-over around

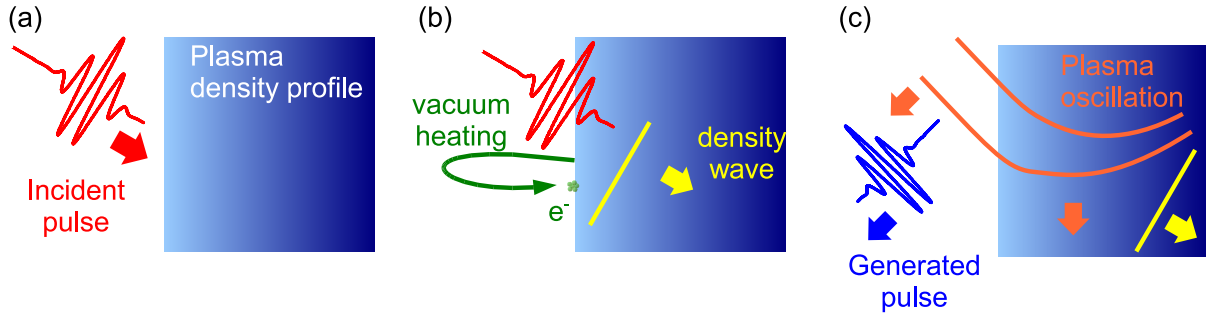


**Figure 2.3:** Schematic illustration of coherent wake emission. (a) The pulse enters the plasma density gradient with oblique incidence. (b) The electric field of the pulse pulls electrons from the plasma into vacuum and then drives them back into the plasma. The plasma gains the energy through the re-collision (vacuum heating) and plasma density wave is generated. (c) Plasma oscillation in the wake of the density wave generates a pulse back into the vacuum.

the frequency  $\sqrt{8}\gamma^3$ . It is also shown that the harmonics and a pulse train generated from CWE is chirped in two ways. One is a chirp generated within the density gradient, because the higher frequency component is generated from the higher-density part in the plasma and hence needs to travel more to come out of the plasma. The other is a chirp coming from the velocity of the electrons pulled out into the vacuum. Since the velocity of the electrons is dependent on the intensity of the incident pulse, the time they require to re-collide with the plasma surface depends on the intensity. In other words, it gains a chirp according to the intensity envelope of the pulse. The former introduces a chirp in a single attosecond pulse in a train, which is analogous to an atto chirp observed in gas HHG [65], while the latter changes the time spacing between individual pulses in a train, analogous to a harmonic chirp [65].

### 2.3 Route to intense attosecond pulses

One of the most appealing aspects of harmonic generation from solid surfaces is its potential to generate intense attosecond pulses [27]. In fact, the predicted harmonic generation efficiency is several orders of magnitude higher than that of gas HHG and thus attosecond pulses with very high intensity are expected. According to theoretical studies, the surface HHG process is capable of generating a train of attosecond pulses [55] or an isolated attosecond pulse [27, 56], analogously to the gas HHG. To date, the generation of attosecond pulses has been demonstrated only for gas HHG and no experimental work for surface HHG has been reported. In this section, I will describe methods to generate a train of attosecond pulses and an isolated attosecond pulses by reviewing the methods demonstrated in gas HHG and discussing the applicability of these methods to surface HHG.

### 2.3.1 Generation of a train of attosecond pulses

When several equidistant frequencies are phase-locked, superposing them will lead to a train of pulses much shorter than the cycle of the original frequencies [8]. Applying this idea to the harmonics was proposed to generate a train of attosecond pulses [9, 10]. One of the properties that makes harmonic generation process suitable for attosecond pulse generation is its broad spectral span of the generated harmonics. Even for harmonics from a monochromatic wave, the overall spectral bandwidth is as wide as  $\Delta\omega \sim 2N\omega$ , where  $N$  is the number of the synthesized harmonics. The expected pulse duration after the Fourier synthesis is  $\tau \sim 1/\Delta\omega \sim 1/2N\omega$ . Note that the factor of 2 appears only for gas HHG, where only odd harmonics are generated. For example, when a 800 nm fundamental wave ( $\omega = 2.35 \times 10^{15}$  Hz) is used, synthesizing three harmonics of gas HHG (five for surface HHG) can lead to an attosecond pulse train, where each pulse is as short as  $\sim 100$  as.

Above mentioned analysis assumed that the harmonics were phase locked, which is not necessarily the case in reality. In fact, it was found that the individual atoms are not phase locked in the gas HHG process [11]. On the other hand, it was also found that the propagation in the atomic media will result in the phase locking of the harmonics [11], which allows to generate of an attosecond pulse train. The generation of a train of attosecond pulses with gas HHG is also successfully demonstrated experimentally [16, 17].

Since the physical origin of harmonic generation from the plasma surface is different from that of gas HHG, the same question arises as to whether harmonics are phase locked and attosecond pulses can really be generated. Theoretical studies found that this is indeed the case and predicted that it is possible to generate a train of attosecond pulses [55, 66].

### 2.3.2 Generation of isolated attosecond pulses

Although a train of attosecond pulses can be used for applications such as spectroscopy, the interpretation of the measurement will not be straightforward because the measured data will be a convolution of information from each pulse in the train. Therefore, an isolated attosecond pulse would be more desirable. Generating single attosecond pulses is not an easy task, but fortunately it is possible to apply methods used in gas HHG experiments. Here I will describe two possibilities: using few-cycle pulses and polarization gating.

#### Use of few-cycle pulses

The most straightforward way to generate attosecond pulses is to use short driver pulses so that harmonics are generated only within one cycle [13, 14]. This method has been demonstrated in gas HHG experiments [1] and the attosecond pulses generated by this method have been used in several applications [3, 4, 67].

Figure 2.4 illustrates the principle of this method. When the incident pulse is short enough, the highest frequency component is generated only at the middle of the pulse, where the intensity is significantly higher than the other part of the pulses. Filtering out that highest-frequency part of the spectrum will lead to a single attosecond pulse. When the incident pulse is longer, on the

other hand, the high frequency component is generated over several cycles, i.e., filtering results in a train of attosecond pulses instead of a single attosecond pulse. It is also important to note that a shorter incident pulse can lead to a shorter attosecond pulse, because the threshold intensity at the middle will be lower and thus the spectral region that can be used to synthesize the attosecond pulse will be broader.

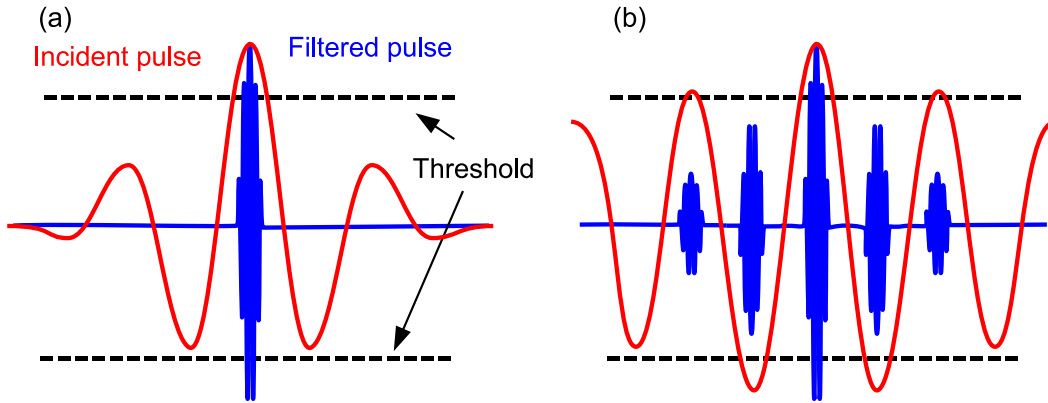


**Figure 2.4:** Principle of single attosecond pulse generation by a few-cycle pulse. Dashed lines show the threshold intensity for generating the high frequency component of interest. (a) When the incident pulse is short, only one cycle contributes to the generation of the high frequency component. Single attosecond pulses can be extracted by filtering out this frequency component. (b) When the incident pulse is longer, where the high frequency component is generated over several cycles, a train of attosecond pulses is generated instead. Note that these are symbolic drawings to show the idea. In reality, the generation timings of the attosecond pulses do not necessarily coincide the peaks of the fields.

It is possible to apply this method to the surface HHG process directly because the principle is the same; the high frequency component is generated only at the middle of the pulse where the intensity is high enough. There is a small difference that the high frequency component is generated twice per cycle for gas HHG, while once per cycle for surface HHG. This difference is actually advantageous in practice because the condition on the pulse duration is slightly relaxed. A feasibility of attosecond pulse generation for surface HHG using few-cycle pulses is thoroughly studied by numerical simulation [27], and they predict that the generation of 5 at pulse with the efficiency of  $2.2 \times 10^{-5}$  is possible by using an ordinary copper filter when the intensity is sufficiently high.

One important thing to consider is the effect of carrier-envelope phase (CEP), namely CEP offset [68] and absolute phase [69]. Figure 2.5 illustrates the concept of CEP offset and absolute phase. The absolute phase of the pulse is defined by the phase of the carrier with respect to the envelope. The absolute phase is not necessarily the same for all the pulses coming out of the laser system but shifts by a constant amount, which is the definition of the CEP offset. The effect of the CEP offset and the absolute phase is negligible for longer pulses where the process occurs over several cycles, because the harmonic yield is averaged over those cycles. On the other hand,



if the harmonic is generated only during one or two cycles, there is no averaging effect and the change in CEP results in a significant change in generated XUV pulses. In gas HHG, a cosine pulse produces a single attosecond pulse, while a sine pulse produces two attosecond pulses [70]. For surface HHG, numerical simulations predict an analogous behavior [27]. Therefore, it is necessary to control the CEP to generate isolated attosecond pulses.

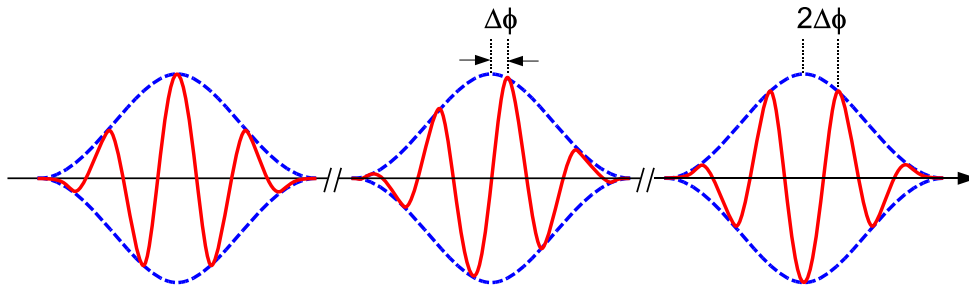


**Figure 2.5:** Schematic drawing of CEP offset and absolute phase. The absolute phase is the phase of the carrier with respect to the envelope. On those three pulses from left to right, the absolute phases are  $0$ ,  $\pi/2$ , and  $\pi$ , respectively. The absolute phase shifts by a constant amount  $\Delta\phi$  from one pulse to next, which is known as CEP offset.

### Polarization gating

Although the method mentioned in the previous subsection is straightforward, it is not easy to obtain the few-cycle pulses necessary for the method to work. It is even more difficult for surface HHG, where very high intensity is also required. Therefore, another method is proposed to utilize the ellipticity dependence of the gas HHG process [12], most commonly referred to as polarization gating. Since the efficiency of the gas HHG process drops dramatically when the polarization of the pulse becomes elliptical [71, 72], it should be possible to confine the harmonic generation time not only by the intensity but also with the polarization. The idea is to use an incident pulse with a changing polarization, so that only the central part is linearly polarized while the edges of the pulse are elliptically polarized (Fig. 2.6). This way, the harmonic generation efficiency will be high only in the ‘gate’ where the polarization is close to linear and thus harmonic generation can be confined to a single cycle.

Several methods have been proposed and tested to obtain pulses with changing polarizations, for example, combining two orthogonally-polarized pulses with different frequencies [12, 73], combining two pulses with counter-rotating polarizations [74, 75, 76], and using two Michelson interferometers [77]. Since the first method is rather difficult to implement experimentally because of the difficulty to obtain two synchronized pulses with different frequencies, I will describe only the other two methods.

Combining two pulses with counter-rotating polarizations can be achieved by first preparing two orthogonally polarized pulses with a delay and then sending both of them through a quarter-wave plate. When the axes of the quarter-wave plate is properly aligned, the two linearly

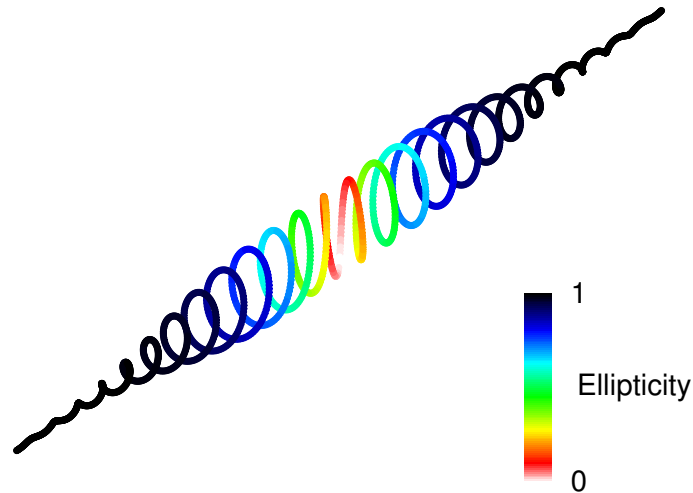


**Figure 2.6:** Pulse with changing polarization, used for polarization-gating technique. The instantaneous ellipticity is color-coded into the pulse. The polarization of the pulse is circular at one edge, and it gradually changes to linear polarization at the center, and then changes back to circular polarization of the opposite direction at the other edge.

polarized pulses turn into two pulses with counter-rotating polarizations. The delay between the two polarization component is usually introduced by a birefringent crystal rather than a Michelson interferometer to achieve a high throughput and high stability. This method has been applied not only to long pulses but also to 5 fs pulses and generation of a single attosecond pulse with the duration of 130 as has been reported [19, 78].

Although the method mentioned in the previous paragraph has advantages of simplicity and stability, it had a problem for pulses as long as  $\sim 50$  fs or longer. To achieve a short gate using a long pulse, a long delay between two orthogonal components is necessary. If the delay between the two components is too large, the overlap becomes very small, which makes the intensity at the middle drop rapidly and hence decreases the total efficiency significantly. The method called interferometric polarization gating, which uses two Michelson interferometers, has been proposed to overcome this problem [77]. The idea is to combine a pulse with high amplitude at the middle with a pulse with low amplitude at the middle orthogonally, thus making a linear polarization at the middle. Each of these pulses is synthesized with a Michelson interferometer. If the delay between the two pulses are aligned properly, a pulse with the polarization changing from circular to linear and back to circular is obtained, same as the previous method. A slightly modified scheme using two consecutive Mach-Zehnder interferometers was also proposed to improve the stability of the setup [79]. Although these method are more complicated compared to the two-crystal scheme, it has an advantage that the gate width can be made shorter with higher efficiency.

Since the process of harmonic generation is different, care must be taken to apply this method for surface HHG. It is especially important to note that the interaction at the plasma–vacuum interface is different between  $p$ - and  $s$ -polarizations, which makes it different from the gas HHG

process. A theory predicts that it is possible to introduce a similar kind of gating for a case of normal incidence by controlling the transverse component of the vector potential [80]. On the other hand, this is not very practical in experiments because the normal incidence means that the generated light will be reflected back in the direction of the incoming beam. A numerical study was made under more realistic condition of oblique incidences [81], and they predict that the technique of polarization gating can be certainly used to obtain a single attosecond pulse in a practical experimental scheme.

One more issue that cannot be neglected is the problem of nonlinear effects from the transmission in the optics such as wave-plates and beam splitters. Since very high intensity is necessary for the process of surface HHG, the value of  $B$ -integral [82] from a couple of optics can easily exceed the value of 1, which results in undesirable consequences such as formation of hot spots in the beam. It is not easy to avoid this problem. Making the optics thin to minimize the nonlinear effect is not as easy as it sounds because the beam used for surface HHG usually has a diameter as large as  $\sim 50$  mm, and it is difficult to manufacture very thin optics with this size. Manipulating the polarization before compressing the pulse is not as straightforward because the compressor is usually polarization sensitive and hence destroys the manipulated polarization. This problem makes it difficult to implement polarization gating for surface HHG, especially interferometric one because it needs many transmission optics. Therefore, extra care must be taken when applying polarization-gating technique to surface HHG.

## 2.4 Particle-in-cell simulation

One of the most powerful tool for studying the laser–plasma interaction is the particle code [83], more commonly known as particle-in-cell (PIC) simulation code. PIC codes can be used to simulate the interaction between the electromagnetic field and the charge particles.

The approach of the PIC simulation is rather simple. In an ordinary PIC code, the space is divided into many cells and each cell contains so-called macro particles. A macro particle is a collection of charged particles and treated as a single particle in the simulation. First, the charge and current density are calculated in each cell. Using this charge and current density, the electromagnetic field is obtained by solving the Maxwell equation in a self-consistent way. Then these fields are used to calculate the next charge and current distribution from the equation of motion. In other words, PIC codes uses only very fundamental equations and do not make any other assumptions. Therefore, simulations on PIC codes can be considered as numerical experiments.

To study the behavior of harmonic generation efficiency as the plasma scale length grows, I have made a series of simulation using a PIC code LPIC++ written by Lichters [30, 84]. This is a 1D3V (one spatial, three velocity dimensions) PIC code that allows to simulate the interaction between a laser pulse and a plasma in any angle of incidence for any polarizations. This code is basically one dimensional code and has an advantage that it requires less computation time compared to two dimensional or full three dimensional code, and has a disadvantage that it is not capable of simulating spatial effects. Nevertheless it is a useful tool for gaining insights into physical processes.

In the simulation, a two-cycle Gaussian pulse was used as the input pulse. This short pulse duration was chosen so that the computation time would be reasonably short. The pulse was incident onto the target with  $p$ -polarization at  $45^\circ$  incidence angle. The target density was set to 240 times the critical density. Figure 2.7 shows one of the typical harmonic spectra obtained from LPIC++. In this run, the amplitude of the incident pulse was  $a = 5$  and the plasma scale length was  $L = 0.1\lambda$ . The shape of the input pulse is shown in the inset of Fig. 2.7 as a blue curve. The reflected pulse is obtained as the curve in the same inset, and the spectrum is obtained by Fourier transforming it.

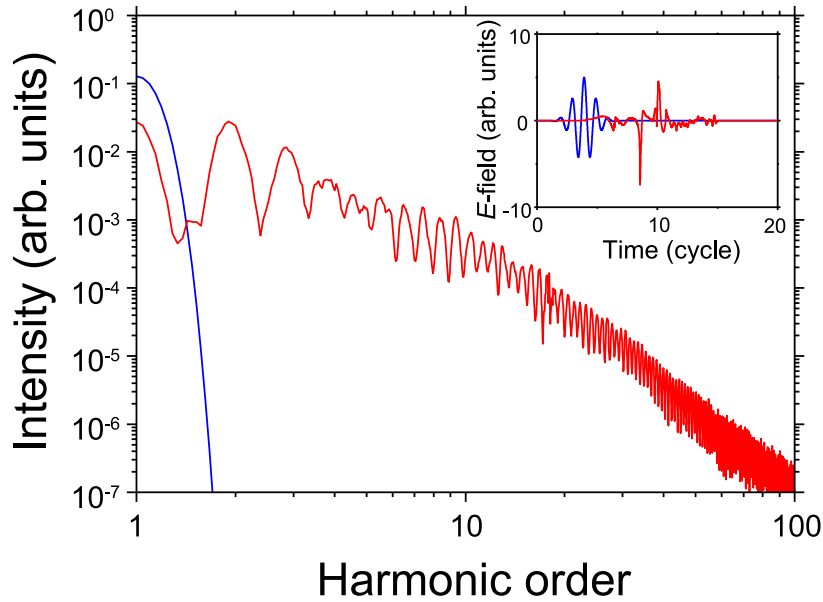


**Figure 2.7:** Harmonic spectrum obtained from PIC simulation (red curve) at  $a = 5$ ,  $L = 0.1\lambda$ . The blue curve shows the spectrum of the incident pulse. The inset shows the electric field of the incident (blue) and reflected (red) pulse.

A series of runs was made by changing the amplitude  $a$  and the scale length  $L$ . The efficiency of the harmonic generation between 10th order to 50th order, which corresponds approximately to the transmission of aluminum filter, was calculated from each spectrum. The result is shown in Fig. 2.8. Harmonic generation is not very efficient when the scale length is zero, i.e., when the plasma–vacuum boundary is sharp, and becomes most efficient around  $L \sim 0.2\lambda$ . This observation is consistent with the observation of other studies [31, 46, 47]. The low efficiency at zero scale length is explained by the huge force needed to overcome the restoring force in the dense plasma. An important thing to note is the sharp drop of the efficiency once the scale length exceeds the optimal region. Since the expansion of the plasma density profile to the scale length of  $\sim 0.5\lambda$  typically takes place in the order of  $\sim 10$  ps [45], it is very important for the process of surface HHG to suppress the preplasma generation before this time, i.e., the contrast in this time scale must be kept high. Improving the contrast in a few-picosecond time scale is not possible with electronic devices. One of the possible solutions is the plasma mirror, which is capable

of improving the contrast in sub-picosecond time scale, and I will discuss about it in the next chapter.

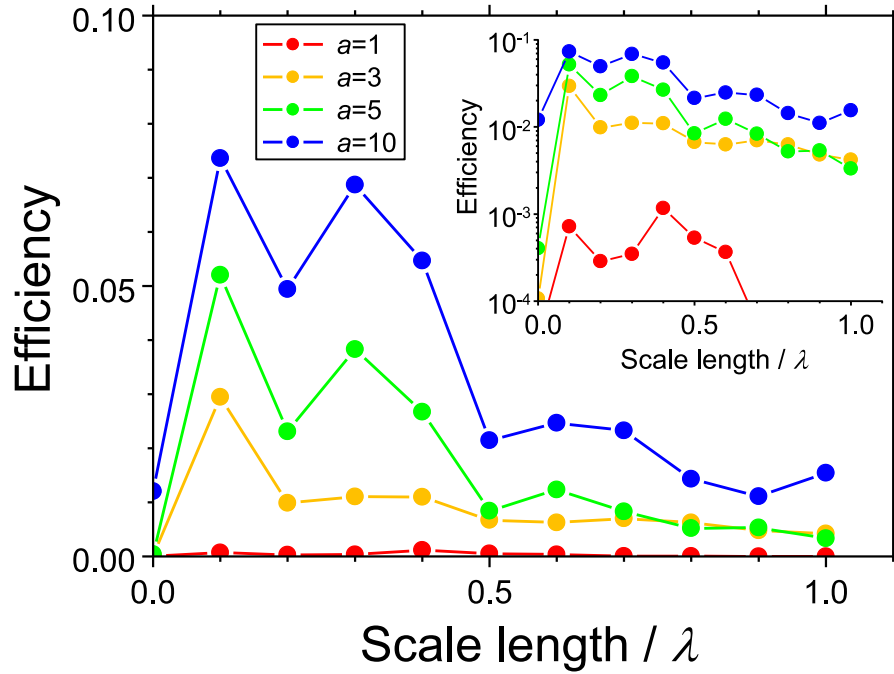


**Figure 2.8:** Harmonic generation efficiency as a function of scale length obtained for four different intensities. Harmonic generation is efficient around  $L \sim 0.2\lambda$ . The efficiency drops sharply when the scale length increases. The inset shows the same plot in log scale to show the same feature for  $a = 1$ .



# Chapter 3

## Plasma mirror with sub-10-fs pulses

The contrast of the laser pulse is one of the most important parameters in high-energy laser–plasma interaction. If the contrast is not high enough, this will result in a formation of preplasma, which impairs the interaction process. To achieve high contrast, one possibility is to use a plasma mirror, which is the main topic of this chapter. I will report on the performance of the plasma mirror with sub-10-fs pulses, namely the reflectivity of the device and the refocusability of the reflected beam. The temporal evolution of the reflectivity is revealed by a high-dynamic-range third-order correlation measurement.

### 3.1 Plasma mirror

#### 3.1.1 Background

A laser pulse generated by a chirped-pulse amplification (CPA) system [85] is typically not a perfect Gaussian and has features shown in Fig. 3.1. The main pulse is surrounded by pre/postpulses, pedestal generated from amplified spontaneous emission (ASE), and pedestal coming from imperfect compression. The contrast of the pulse is defined by the ratio between the intensity of the main pulse and the intensity of the prepulses/pedestal. When the intensity is low, the prepulses or pedestal play no significant role because they are usually several orders of magnitude less intense than the main pulse and their intensities are well below the damage threshold and plasma formation limit of the target.

The situation changes significantly when the energy of the laser pulse becomes high and reaches a certain level. When the prepulses/pedestal become intense enough, for example, intensity of  $\sim 10^{12} \text{ W cm}^{-2}$  for fused silica [86], they start to damage the material, i.e., plasma starts to generate. If the plasma is generated before the main pulse arrives, it will expand hydrodynamically. In other words, the main pulse will no longer interact with a clean, steep plasma density profile. This deformation of the plasma–vacuum interface changes the processes based on the interaction at the plasma–vacuum interface such as high-order harmonic generation from solid surfaces [27, 31, 48] and ion acceleration [87, 88], and often leads to unfavorable consequences. Therefore, it is extremely important for the high-intensity laser–plasma interaction processes to

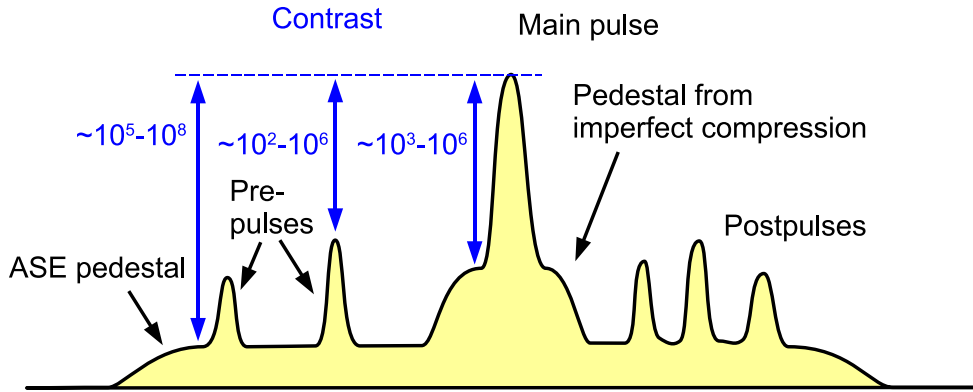


**Figure 3.1:** Typical pulse from chirped-pulse amplification (CPA) system. Aside from the main pulse, it generally has pre- and post-pulses. Pedestals usually come from amplified spontaneous emission (ASE) and imperfect compression. Contrast of the pulse is defined by the ratio between the intensities of the main pulse and prepulses/pedestal. Typical values of the contrast are indicated for prepulses and pedestals.

keep the prepulse/pedestal intensity low. For a pulse with the intensity of  $\sim 10^{19} \text{ W cm}^{-2}$ , for example, the contrast of  $10^7$  or higher is required to have an ideal interaction.

There are several ways to improve the contrast of the laser pulse. Some methods focus on improving the contrast of the pulse before stretching in the CPA system. The methods classified into this category includes nonlinear Sagnac interferometers [89], nonlinear polarization rotations [90, 91, 92], and cross-polarized-wave (XPW) generation [93, 94]. Since the energy applicable to these methods is limited and the throughput is rather low, further amplification is usually necessary. A scheme using double CPA stages was demonstrated [92], where the pulse was amplified with the first CPA stage to the energy level necessary for the nonlinear process of cleaning, sent through a nonlinear temporal filter to improve the contrast, and then amplified again with the second CPA stage. The plasma mirror [95], on the other hand, is used to improve the pulse after amplification and compression and provides higher throughput without limitation on the input energy. Since it is used after the whole CPA chain, the plasma mirror can be implemented in a laser system without any modification to the system itself. Other advantages include spatial filtering effects [95] and wide bandwidth acceptance.

Several investigations have been conducted to study the reflectivity of the plasma mirror [96, 97] and the spatial profile of the reflected beam [97, 98, 99]. Some studies have pursued the applicational possibility of the plasma mirror: improving the repetition rate by using a liquid jet as the target [100] and cascading two plasma mirrors to improve the contrast even further [99, 101].

All the studies mentioned above used pulses with 25 fs of duration or longer and no experiment has been done with sub-10-fs pulses. On the other hand, intense few-cycle pulses with a sufficiently high contrast would open up a new prospect for many applications [27, 102]. Therefore it has great significance to study the possibility to obtain high-contrast few-cycle pulses using a plasma mirror.



### 3.1.2 Principle

The principle of the plasma mirror is illustrated in Fig 3.2. First, the laser pulse is focused onto a material transparent for the laser wavelength. Since the material is transparent, the prepulse and the pedestal are transmitted. On the other hand, when the main pulse arrives on the target and the intensity exceeds the damage threshold of the material, the target is ionized and plasma is generated on the surface. As soon as the electron density in the plasma exceeds the critical density for the incident wavelength, its reflectivity for the incident pulse switches to a high value, i.e., the main pulse and everything afterward are reflected. This way, the reflectivity is maintained low for the prepulses and the pedestal, while increased by several orders of magnitude for the main pulse. In other words, the contrast of the pulse is increased by the ratio of the plasma reflectivity to cold reflectivity of the material. The contrast improvement is typically 2 to 3 orders of magnitude with AR coated targets or with a geometry close to Brewster's angle.

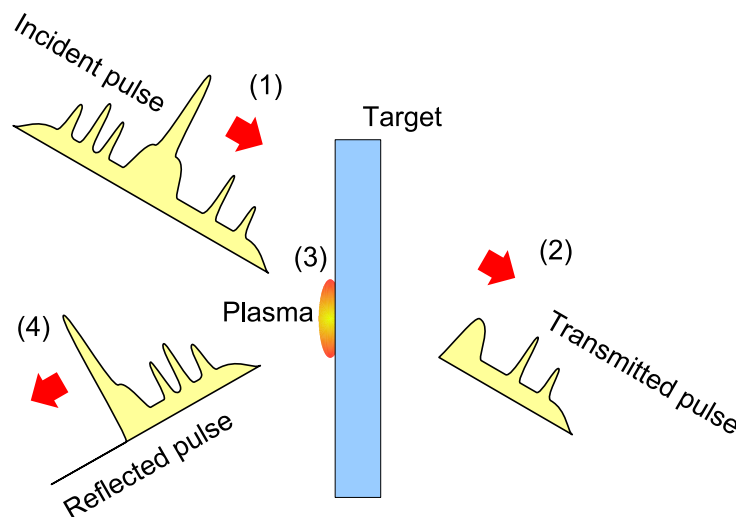


**Figure 3.2:** The principle of the plasma mirror. (1) The incident pulse is focused onto a transparent target. (2) The prepulses/pedestal are transmitted through the material. (3) Plasma is generated by the leading edge of the main pulse. (4) The rest of the pulse is reflected by the generated plasma.

## 3.2 Experimental configuration

### 3.2.1 Laser system

The experiment was conducted with a broadband Ti:sapphire laser system built at Vienna University of Technology [103], based on chirped-pulse amplification with three multi-pass amplifier stages and a hollow-core fiber compressor. The typical output parameters were an energy of 550  $\mu\text{J}$  at 1 kHz repetition rate, and a pulse duration of 7 fs at the central wavelength of

730 nm. Typical output spectrum is shown in Fig. 3.3(a). It extends from 600 nm to 900 nm and its Fourier-transform limit corresponds to 7 fs of pulse duration. Figure 3.3(b) shows a typical second-order autocorrelation trace measured with a second-order autocorrelator (Femtometer PC DAQ, Femtolasers). This trace also corresponds to the pulse duration of  $\sim 7$  fs.

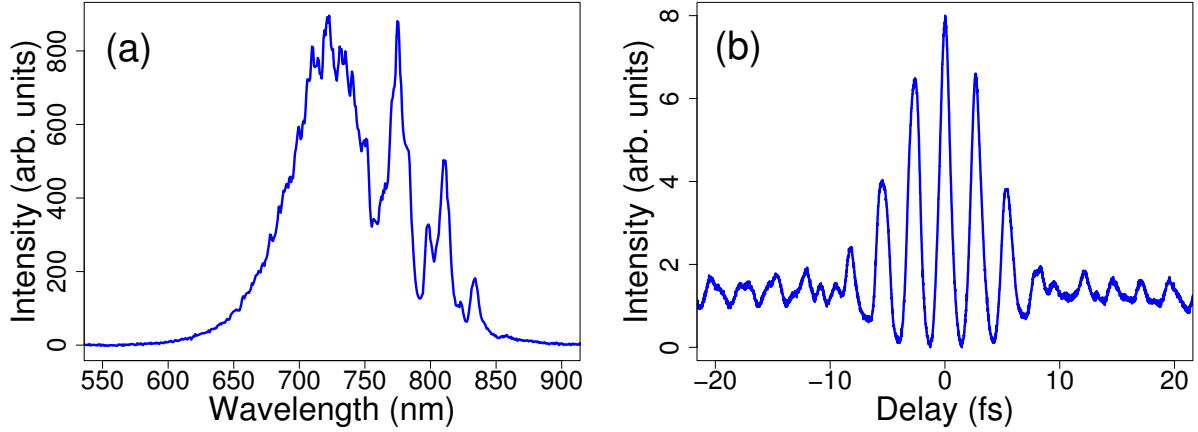


**Figure 3.3:** Typical output from the laser system used for plasma mirror experiment. (a) Spectrum extends from 600 nm to 900 nm. (b) Second-order autocorrelation of the output pulse, corresponding to the pulse duration of 7 fs.

### 3.2.2 Experimental setup

The experimental setup used for reflectivity measurement of the plasma mirror is shown in Fig. 3.4. After the compressor chamber, all the optics were placed in vacuum. The polarization of the beam was set to either  $p$  or  $s$  by changing the alignment of a periscope. The incident beam was expanded to the diameter of 50 mm with a telescope (not shown in the Figure). The beam was focused onto the surface of a target with a silver-coated,  $90^\circ$  off-axis parabola with the effective focal length<sup>1</sup> of  $f_{\text{eff}} = 150$  mm. The energy on target was typically  $350 \mu\text{J}$  to  $400 \mu\text{J}$ . The loss of the energy was due to several optics after the compressor chamber. A round BK7 glass plate with the diameter of 120 mm was used as a target. The target was mounted on two motorized linear translation stages (LM60, OWIS) and one motorized rotation stage (DRT65, OWIS). Rotation and translation along the surface was used to provide a fresh part of the target surface for each shot because each laser shot was intense enough to destroy a small surface of the target. A typical number of shots allowed on each target was  $\sim 2 \times 10^6$  with a spacing of  $\sim 50$  to  $100 \mu\text{m}$  between each spot. In other words, one target lasted approximately for an hour

<sup>1</sup>Here I use the term ‘effective focal length’  $f_{\text{eff}}$  to refer to the distance between the focus and the center of the off-axis parabola surface. This is because the focal length  $f$  of the parabola is defined by the distance between the focus and the bottom of the paraboloid. The relationship between  $f$  and  $f_{\text{eff}}$  is  $f_{\text{eff}} = f / \cos^2(\theta/2)$ , where  $\theta$  is the angle of the off-axis parabola.

at 1 kHz repetition rate. The other translation stage allowed to move the target parallel to the incident beam and was used for focal scan. Reflected beam was collected with an achromatic lens into a detector. Different detectors were used for different experiments, for example, a power meter was used for reflectivity measurement.

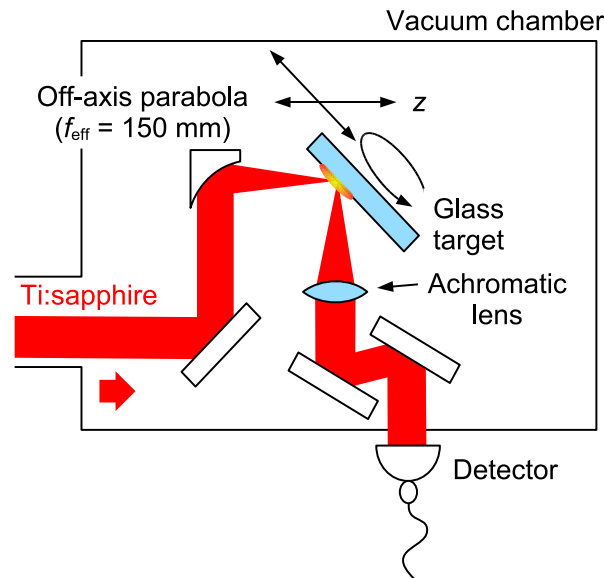


**Figure 3.4:** Experimental setup for reflectivity measurement of the plasma mirror. The 50 mm diameter beam was focused with a silver parabola ( $F = 3$ ) onto a round glass target, which was mounted on three motorized stages. The reflected beam was collected with an achromatic lens and sent onto a detector.

During the alignment, the focus was imaged with a microscope objective onto a charge-coupled device (CCD) beam profiler (WinCamD, DataRay). Figure 3.5 shows a typical image of the focal spot. The full width at half maximum (FWHM) size of the spot was obtained to be  $7 \mu\text{m}$  to  $8 \mu\text{m}$  by fitting Gaussian on vertical and horizontal lineouts. From this value and the values mentioned above, the maximum peak intensity on target during the measurement is estimated to be  $\sim 5 \times 10^{16} \text{ W cm}^{-2}$ .

### 3.3 Reflectivity of the plasma mirror

The efficiency of the plasma mirror was characterized by measuring the energy throughput and the peak reflectivity. The energy throughput is obtained as the ratio of the reflected energy to the incident energy, while the peak reflectivity is the ratio of the reflected peak intensity to the incident peak intensity assuming that the pulse duration did not change during the reflection. This assumption is validated in Section 3.5. The peak reflectivity was calculated from the incident energy and the measured beam profile on the target. The energy throughput is important for applications because this is the direct output from the system. On the other hand, the peak

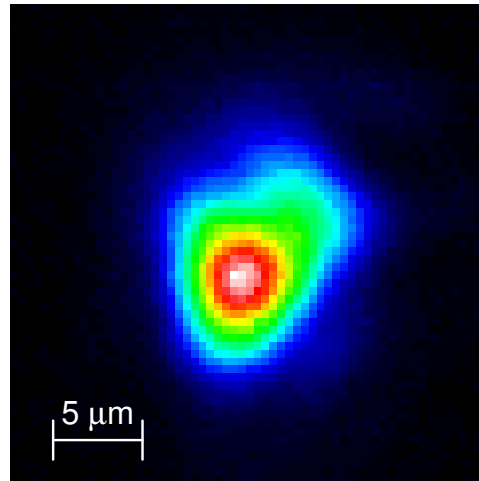


**Figure 3.5:** Image of a typical focal spot. Gaussian fit on a vertical and horizontal lineout returns the full width at half maximum (FWHM) of the spot to be  $7\ \mu\text{m}$ .

reflectivity is also important because this value is independent from the system parameter such as beam profile. This can be considered as the reflectivity at a certain point, i.e., the integration of this value over space and time will yield the energy throughput.

For these experiments, a power meter was used as the detector shown in Fig. 3.4. The throughput of the plasma mirror was measured by comparing the energies in front of the compressor chamber and at the detector outside the vacuum chamber. The throughput of the optics—from the compressor chamber to the target and from the target to the detector—was characterized thoroughly to determine the reflectivity precisely.

The energy throughput was measured as a function of the incident fluence. The incident fluence was changed by either changing the incident energy by using neutral-density (ND) filters (energy scan), or scanning the position of the plasma mirror in focal direction, i.e., changing the spot size on target ( $z$ -scan). Figure 3.6 shows one of the measurement results from the  $z$ -scan. The red circles show the energy measured at the power meter outside the vacuum chamber. The values are the average of several thousand laser shots and the error bars show the characteristic deviation of the measured energy over several seconds. The incident energy on the target was  $\sim 380\ \mu\text{J}$  during this measurement. Since the throughput of the optics between the plasma mirror and the detector (an achromatic lens, two silver mirrors, and an exit window) was  $\sim 73\%$  for our ultrabroadband pulses, the maximum reflectivity for this measurement is calculated to be  $(100/0.73)/380 \approx 0.36$ . The corresponding images of the spots along the  $z$ -axis was observed by making a separate scan right after the energy measurement. This scan was made with low energy to make sure that there is no effect from the plasma mirror. The blue squares in Fig. 3.6

shows the diameters of the spots. The incident fluence for each position was estimated by using this diameter and the incident energy of  $\sim 380 \mu\text{J}$ . The larger error at the positions far from the focus is due to non-Gaussian beam profile.

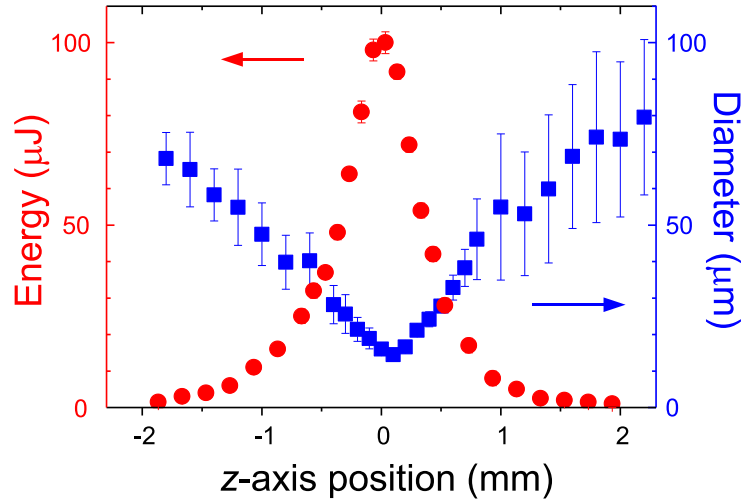


**Figure 3.6:** The reflected energy measured by  $z$ -scan, indicated by red circles. Blue squares show the diameter of the incident beam on the target observed at the corresponding positions. The reflectivity and the incident fluence are calculated from these results.

Figure 3.7(a) shows the energy throughput measured for  $p$ -polarization as a function of the average incident fluence. The average incident fluence is obtained by dividing the half of the energy by the area containing that energy. Different sets of measurements are shown with different symbols in Fig. 3.7. The measurements were well reproducible and gave the same results for the energy scan and for the  $z$ -scan. The highest throughput reached up to  $\sim 40\%$ , while the lowest reflectivity was as low as  $\sim 0.5\%$  because the incidence angle ( $45^\circ$ ) was close to Brewster's angle ( $\sim 56^\circ$ ). From these values a contrast improvement of two orders of magnitude is expected. The throughput was measured also with longer pulse durations, which was achieved by either chirping the pulse or clipping the spectrum. Chirping was achieved by inserting several pieces of AR-coated glass (total thickness of 3.5 mm) into the beam right before the compressor, which stretched the pulse duration to  $\sim 50$  fs. Clipping was achieved by placing a beam block in the prism compressor in front of the hollow-core fiber [103] and observing the spectra after the fiber. The bandwidth after clipping is shown in the legend of Fig. 3.7 in parentheses. With this method, the Fourier limited pulse duration was made longer to either  $\sim 30$  fs or  $\sim 60$  fs. Although the pulse duration was increased up to  $\sim 60$  fs, i.e., a factor of 8, no significant change was observed in the behavior of the reflectivity. This result is consistent with the observation of Doumy *et al.* [97]. Therefore, I plotted the reflectivity as a function of the incident fluence in Fig. 3.7.

The energy throughput measured for  $s$ -polarization is plotted in Fig. 3.7(b). The highest reflectivity reached up to  $\sim 65\%$ , which is higher than the reflectivity obtained for  $p$ -polarization. This is due to the absence of resonance absorption [83] and Brunel absorption [63] for  $s$ -polarization,

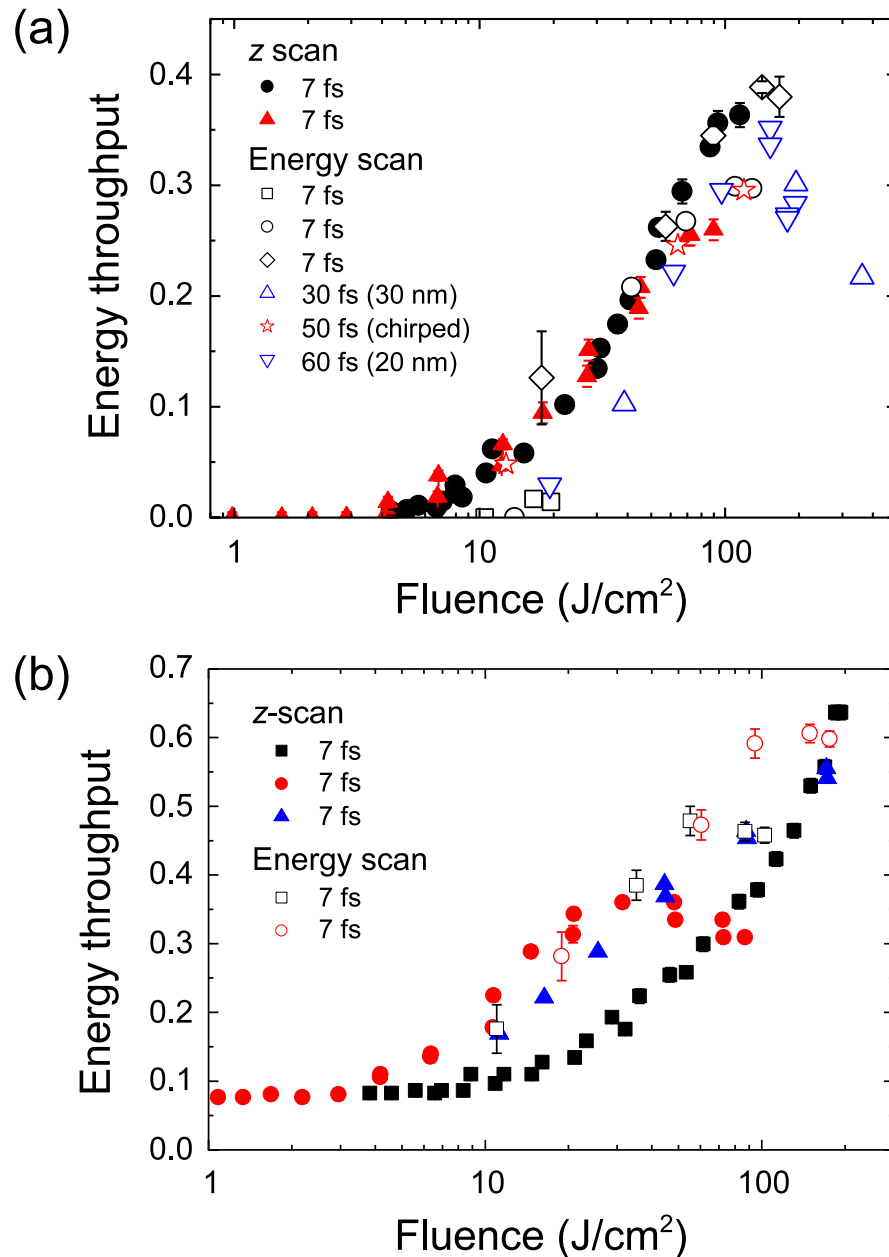


**Figure 3.7:** Energy throughput of the plasma mirror measured as a function of the average incident fluence. Different symbols represent different sets of measurements. (a) For  $p$ -polarization, the highest and lowest reflectivity are measured to be  $\sim 40\%$  and  $\sim 0.5\%$ , respectively. From these values, contrast improvement of two orders of magnitude is expected. The pulse duration was changed either by chirping or by clipping the spectrum. In the case of clipping, the bandwidth after the clipping is indicated in the legend. (b) For  $s$ -polarization, the reflectivity is higher than that of  $p$ -polarization. On the other hand, the expected contrast improvement is lower because of the higher reflectivity for low incident fluence.

in contrast to  $p$ -polarized light, where these processes absorb the energy and thus reduce the reflectable energy. On the other hand, the expected contrast improvement is only one order of magnitude because of the relatively high Fresnel reflectivity for  $s$ -polarization, which is  $\sim 8\%$  at  $45^\circ$  angle of incidence for our target material. The results plotted in Fig. 3.7(b) had larger fluctuations than those in Fig. 3.7(a) owing to the different laser conditions from different days.

Reducing the Fresnel reflectivity with anti-reflection (AR) coated targets [97] will boost the contrast improvement up to factor of 200. Therefore, using  $s$ -polarized beam with AR-coated targets is ideal for obtaining the maximal throughput (65%). On the other hand, AR-coated targets are expensive, especially when they have to be replaced frequently. Using  $p$ -polarized light solves this problem at the cost of decreased throughput (40%). The contrast improvement factors are in the same order for  $s$ -polarized light with AR-coated targets and for  $p$ -polarized light with ordinary targets, at  $45^\circ$  incidence angle. Using the plasma mirror at Brewster's angle ( $\sim 56^\circ$  for BK7 glass) will increase the improvement factor for  $p$ -polarization even more, although the alignment will be more complicated because the reflected beam will not be perpendicular to the incident beam any more.

The spatial peak reflectivities for  $p$ - and  $s$ -polarization are depicted in Fig. 3.8 as a function of the peak fluence. The maximum value was above 60% for  $p$ -polarization. It is even higher for  $s$ -polarization, where the maximum value is above 80%, but the measurement had rather large errors. As I mentioned in the beginning of this section, the value of peak reflectivity is important because it is independent from the parameter of the experimental setup. While the average reflectivity shows the overall performance of the specific system, the peak reflectivity shows the performance that depends solely on physics. Since this value is system-independent and similar values are obtained with other experiments [96, 97], it can be used to estimate the throughput when one needs to implement a plasma mirror on a different system.

### 3.4 Refocusability of the reflected beam

Since the plasma mirror is based on a nonlinear plasma effect, it is not self-evident that the focusability of the reflected beam is comparable to that of the incident beam. Therefore, the spatial profile of the reflected beam was characterized by refocusing it.

The setup was slightly modified from the previous measurement, as shown in Fig. 3.9. The reflected beam was collimated with an achromatic lens ( $f = 150$  mm) and refocused with a  $90^\circ$ ,  $f_{\text{eff}} = 75$  mm off-axis parabola. The image of the refocused spot was magnified with a microscope objective and captured by a CCD beam profiler (WinCamD, DataRay).

Figure 3.10 shows some of the images of the refocused spot. As a reference, the refocused image was observed without activating the plasma mirror [Fig. 3.10(a)]. This image was taken when the focus of the incident beam was exactly on target, while the incident fluence was sufficiently low so that no plasma was generated, in other words, the plasma mirror was “off.” Figure 3.10(b) shows an image observed at the same position and with the full incident energy, i.e., with the plasma mirror “on.” The spot is smaller and the corresponding near-field beam profile is cleaner than the one measured without activating the plasma mirror. The horizontal and vertical lineouts of the refocused spot images clearly shows that the spot is smaller when the

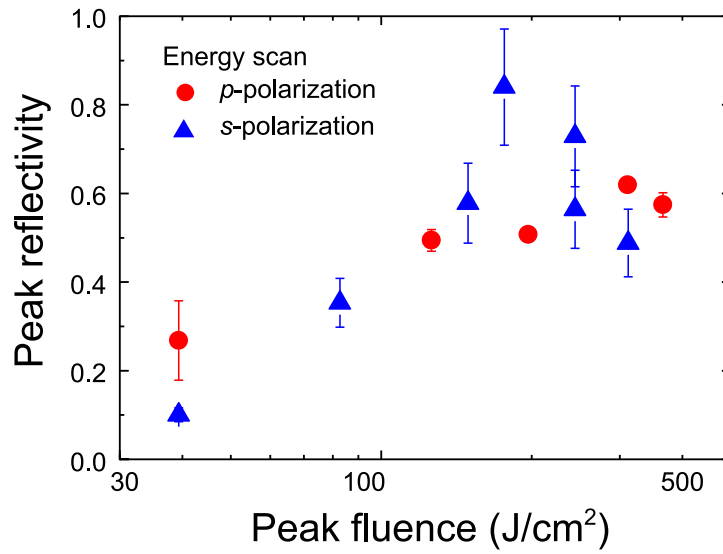


**Figure 3.8:** Peak reflectivity of the plasma mirror plotted against the spatial peak fluence of the incident beam. The maximum reflectivity reached  $\sim 60\%$  for  $p$ -polarization and  $\sim 80\%$  for  $s$ -polarization.

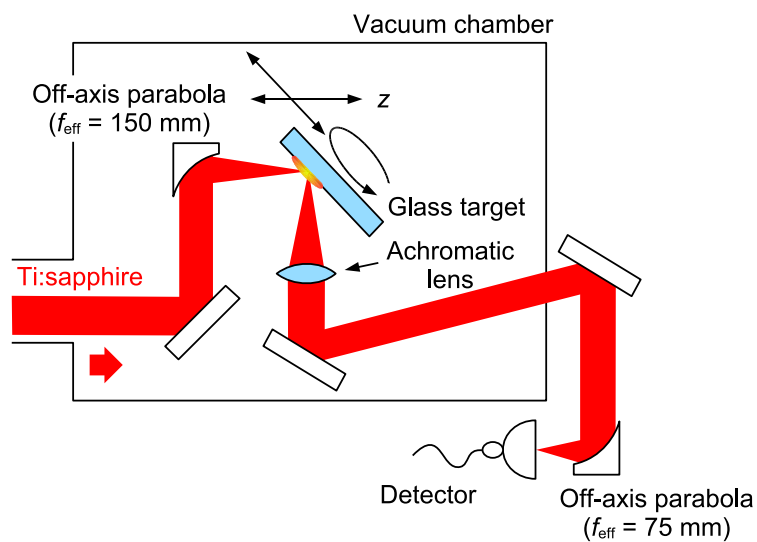


**Figure 3.9:** Setup for refocusability measurement. The reflected beam was collimated with an achromatic lens and refocused with an off-axis parabola ( $f_{\text{eff}} = 75$  mm). The refocused image was observed with a CCD camera with a microscope objective.



plasma mirror is “on,” as shown in Fig. 3.11.

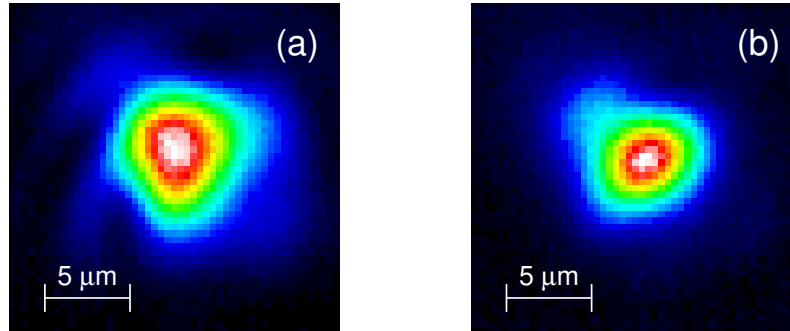


**Figure 3.10:** Images of the refocused spot. (a) Image taken while the plasma mirror was off, i.e., when the incident fluence was low. (b) Image taken while the plasma mirror was operating.

To study the behavior of the plasma mirror further, the refocused image was observed by scanning the plasma mirror in  $z$ -direction and adjusting the imaging system for each position to find the best refocused spot. The measured spot diameters are plotted as a function of the plasma mirror position in Fig. 3.12. The horizontal lines indicate the spot diameter when the plasma mirror was “off.” The different focus diameters for  $s$ - and  $p$ -polarizations are due to different alignments of the beam line. It is clearly seen that the diameter of the reflected beam becomes smaller when the plasma mirror is “turned on” and it is placed close to the focus of the incident beam.

Two effects are observed on the refocused beam profile: smaller spot size and cleaner beam profile. Both effects are explained by the fluence-dependent reflectivity of the plasma mirror. The plasma mirror reflects more efficiently at the central part of the beam, while the reflection at the surrounding area is relatively suppressed. In other words, the plasma mirror acts as a spatial filter that makes the beam profile cleaner [104]. At the same time, this fluence-dependent reflectivity makes the peak narrower, which results in a smaller spot size right after the reflection off from the plasma mirror and consequently a smaller refocused spot size.

### 3.5 Time-resolved reflectivity measurement with third-order correlation

The temporal characteristics of the reflected beam was also investigated by measuring a high-dynamic-range third-order correlation. The setup was almost the same as the one shown in Fig. 3.4 except for the detector, where a home-made third-order correlator [105] was used. The polarization of the beam incident to the target was set to  $p$  because a better contrast improvement

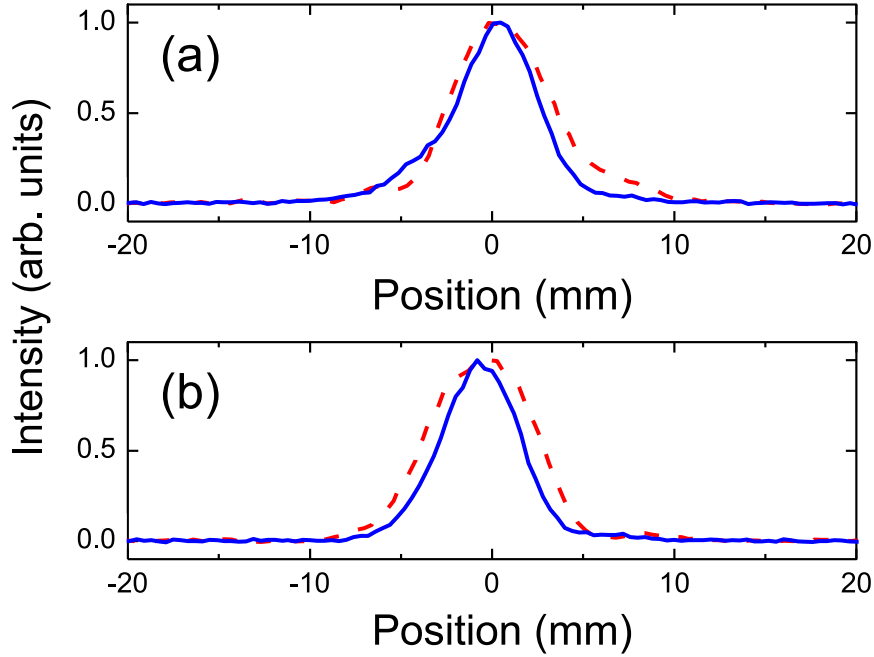
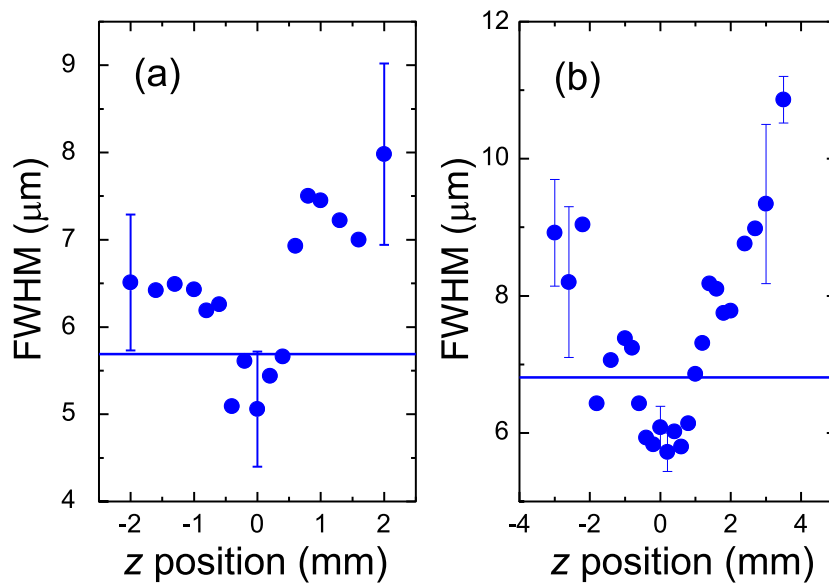


**Figure 3.11:** (a) Horizontal and (b) vertical lineouts of the refocused images with (blue solid line) and without (red dashed line) the plasma mirror. Refocused spot size is clearly smaller when the plasma mirror is “on.”

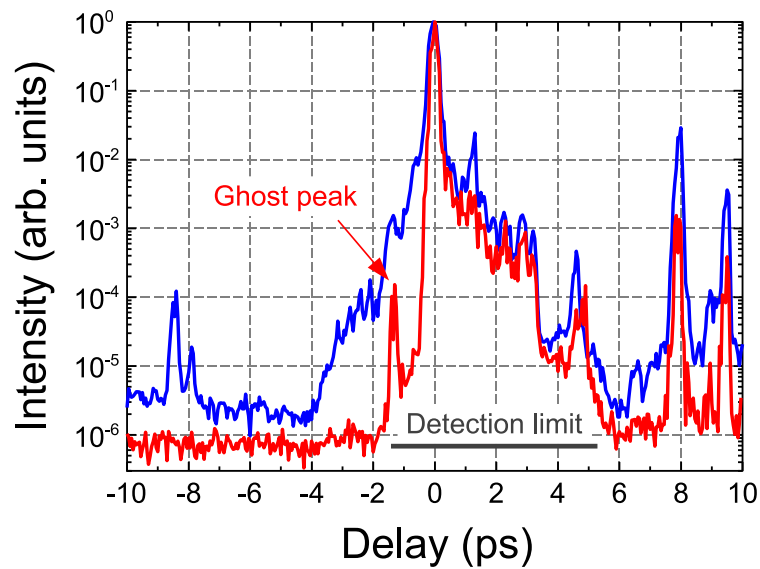
was expected. The fluence on the plasma mirror during this measurement was estimated to be  $\sim 60 \text{ J/cm}^2$ . The reflected beam was re-collimated and sent into the third-order correlator.

Figure 3.13 shows the measured third-order correlation of the reflected pulse together with that of the incident pulse. The negative delay represents the leading edge of the pulse. Although the measured contrast was limited to  $10^6$  because of the low energy ( $\sim 50 \mu\text{J}$ ) sent into the correlator, the expected contrast improvement of two orders of magnitude is clear at the pulse front, for example, around  $-2 \text{ ps}$  or at  $-8.5 \text{ ps}$ . The peak appearing at  $-1.5 \text{ ps}$  is an artifact from a post pulse, which appears due to the nature of correlation measurements. A pulse-steepening effect is also evident on the rising edge [106]. On the other hand, no effect is observed on the falling edge of the pulse, which implies that the reflectivity was constant during the pulse. Since  $100\text{-}\mu\text{m}$ -thick crystals were used in the correlator to gain strong signals, the third-order correlation trace does not reflect the short pulse duration shown in Fig. 3.3.

Figure 3.14 depicts the time-resolved reflectivity of the plasma mirror for  $p$ -polarization obtained by dividing the correlation trace of the reflected pulse by that of the incident pulse. The curve was normalized by setting the average value between  $0 \text{ ps}$  and  $4 \text{ ps}$  to the expected peak reflectivity of  $50\%$ . A steep rise of the reflectivity is clearly seen starting from  $-500 \text{ fs}$ . This steep rise indicates that the plasma is generated  $\sim 500 \text{ fs}$  before the main pulse. This suggests that the plasma mirror was activated with the pedestal of the sub-10-fs pulses, similarly to the previous experiments with longer pulses. It is apparent that the reflectivity is constant during the



**Figure 3.12:** Refocused spot size (FWHM) as a function of the plasma mirror position in the focal ( $z$ ) direction. The measurement was made with (a)  $p$ - and (b)  $s$ -polarization on the plasma mirror. Horizontal lines indicate the reference spot size without activating the plasma mirror.



**Figure 3.13:** Third-order correlation measured with (red) and without (blue) the plasma mirror. Negative delay represents the leading edge of the pulse. Although the measured contrast was limited by the low input energy ( $\sim 50 \mu\text{J}$ ), contrast improvement of two orders of magnitude is seen in the leading edge, for example, around  $-2$  ps.

pulse, and it starts to decrease again  $\sim 6$  ps after the main pulse.

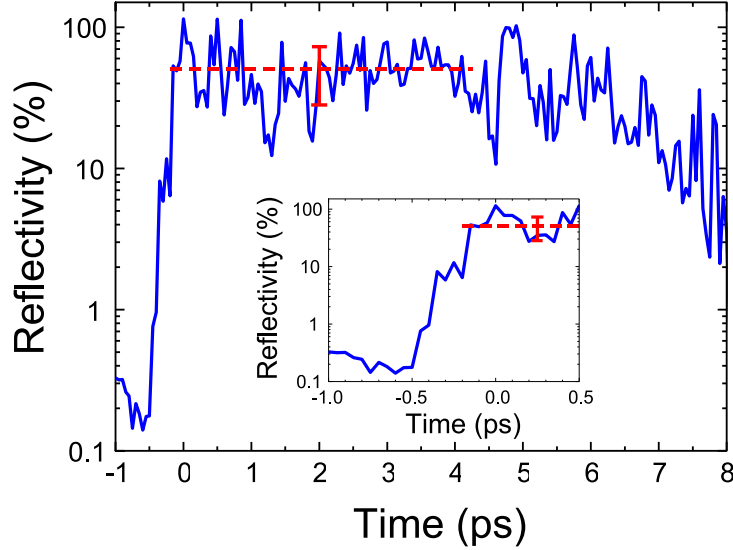


**Figure 3.14:** Time-resolved peak reflectivity of the plasma mirror calculated from the correlation traces in Fig. 3.13. The horizontal red lines show the average value of the reflectivity between 0 ps and 4 ps and the error bar correspond to the standard deviation. The inset shows the magnified view of the reflectivity. Fast increase of the reflectivity is observed at the leading edge.

To further understand the physical process, the hydrodynamic expansion of the plasma was simulated with a simulation code MEDUSA [107]. The input pulse used for the simulation was a 7 fs Gaussian pulse sitting on a 1.7 ps Gaussian pedestal with  $2 \times 10^{-4}$  contrast and 7 fs Gaussian prepulse a 8.5 ps before the main peak with  $10^{-4}$  contrast. The parameter was determined by a fit on the third-order correlation trace measured without the plasma mirror. The result of the simulation is shown on Fig. 3.15, together with the temporal structure of the input pulse. The simulation shows that the scale length  $L \equiv n_e/|dn_e/dz|$  of the plasma, where  $n_e$  is the electron density, is  $\sim 0.03\lambda$  at the critical density when the main peak of the pulse arrives. If the scale length is too large, a plasma mirror acts similarly to a chirped mirror because different wavelengths are reflected at different depths in the plasma surface, owing to the different critical densities. With this scale length, however, this chirping effect is negligible and the pulse duration stays the same after the plasma mirror. The simulation also shows that the scale length exceeds  $0.1\lambda$  around +2 ps after the main peak. Above this scale length, the process of resonant absorption starts [108], and reaches its maximum efficiency around  $L \sim 0.3\lambda$  [83]. The simulation shows that this scale length is reached around  $\sim +4$  ps, which explains the decrease of the reflectivity around 6 ps. The slight quantitative discrepancy is probably due to the imperfect fitting of the Gaussian profiles.

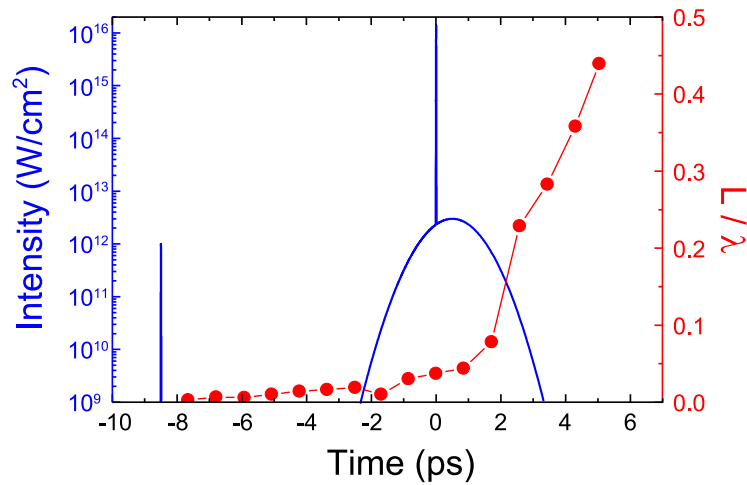


**Figure 3.15:** Evolution of plasma scale length calculated with MEDUSA (courtesy of L. Veisz). The blue curve shows the temporal profile of the input pulse, which has a prepulse 8.5 ps in front of the main pulse and a 1.7 ps Gaussian pedestal. Red circles show the evolution of the plasma scale length. It stays almost unchanged when the main pulse arrives and starts to increase after most of the pedestal has passed.

## 3.6 Summary

In conclusion, the contrast improvement of sub-10-fs pulses by using a plasma mirror is demonstrated. The reflected pulses were cleaned both spatially and temporally. The spatial peak reflectivity reached  $\geq 80\%$  ( $\geq 60\%$ ) and the energy throughput had a value of  $\sim 65\%$  ( $\sim 40\%$ ) for  $s$ - ( $p$ -) polarization at  $45^\circ$  angle of incidence. The first measurement of the complete high-dynamic-range correlation revealed the temporal structure of the pulses reflected from the plasma mirror. The time-resolved reflectivity of the plasma mirror was determined with the help of these results, showing the contrast improvement of two orders of magnitude and the pulse steepening at the leading edge.

Improving the contrast with the plasma mirror will lead to better performances in experiments such as high-order harmonic generation on plasma surfaces. On the other hand, this will impose a limit on the number of laser shots in one experimental run. The use of the plasma mirror should be determined by weighing the benefits gained by the contrast improvements against the drawback of the limited number of shots.



# Chapter 4

## Experimental investigations of HHG from plasma–vacuum interface

In this chapter, the experimental results to characterize the harmonics generated from the ATLAS laser system is presented. Characterizing the properties of the harmonics is important especially if the harmonics are meant to be used as a radiation source. The measured properties of the harmonics are presented and discussed in conjunction with further applications.

### 4.1 Experimental configuration

#### 4.1.1 Laser system

The experiment was conducted using a laser system developed at MPQ, which is an upgraded version of ATLAS [109]. The system is based on Ti:sapphire CPA scheme and consists of a broadband oscillator, a multi-pass pre-amplifier, a regenerative amplifier (regen), and two multi-pass amplifier stages. After the compression, the system typically produced the pulses with the energy of 850 mJ and the duration of 45 fs at the center wavelength of 800 nm with the maximum repetition rate of 10 Hz. Since this laser system is intended for ultrahigh-intensity experiment, extra care was taken to achieve high contrast. One is the pre-amplifier stage before the regen, so that the amplification in the regen could be lowered and thus the generation of the ASE pedestal could be lowered. Another is an extra Pockels cell with a fast rise time ( $\sim 200$  ps) after an ordinary Pockels cell of the regenerative amplifier, which suppresses any of the remaining ASE pedestal at 200 ps before the main pulse.

The contrast of the pulse was measured with a homemade third-order correlator [105]. Figure 4.1 shows the measured autocorrelation trace. The full third-order correlation trace is shown on Fig. 4.1(a). It shows a contrast of  $10^8$  around 100 ps in front of the main pulse. The rapid drops of the signal at the beginning and at the end of the trace shows the noise level ( $10^{-11}$  relative to the peak intensity), which indicates that the measured contrast is not limited by the detection level of the device. The magnified view around the main pulse is shown on Fig. 4.1(b). It shows a slow rise starting around 40 ps before the main pulse, and the contrast at the rising

edge of the main pulse reduces to  $10^6$ . Note that the peak in front of the main pulse is a ghost of a post pulse and does not affect the real contrast of the pulse. For the estimated focal intensity of  $\sim 10^{18} \text{ W cm}^{-2}$  to  $10^{19} \text{ W cm}^{-2}$ , the contrast of  $10^8$  at 40 ps is good enough because this means that the intensity in the pedestal should be lower than the damage threshold of dielectric materials [86]. The experiments described here were performed without a plasma mirror because its use significantly limits the number of laser shots, which will be critical for further applications.

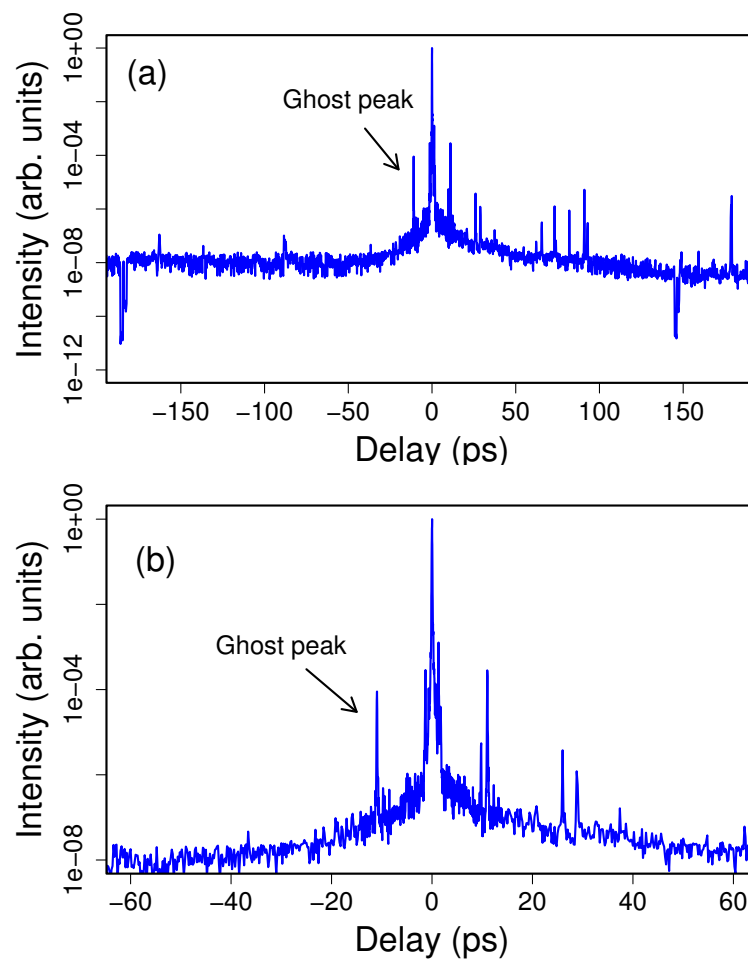


**Figure 4.1:** Third-order correlation trace of the output pulse from ATLAS (courtesy of K. Schmid). (a) Full correlation trace showing the contrast of  $10^8$  at 100 ps before the main pulse. Negative value represents the front side of the pulse. The noise level was measured at the beginning and at the end of the scan (drops of the signal to  $10^{-11}$ ) to make sure that the measured contrast is not limited by the dynamic range of the device. (b) Magnified view of the trace. The pulse shows a slow rise starting around 40 ps before the main pulse. The contrast reduces to  $10^6$  at the rising edge of the main pulse. The peak in front of the main pulse is a ghost of a post pulse and has nothing to do with the contrast.



### 4.1.2 Experimental chamber

The output beam from the system was sent through a vacuum beamline to the experimental chamber. Figure 4.2 shows a photograph and a perspective drawing of the experimental chamber used for the first measurement. The 60-mm-diameter infrared (IR) beam coming from the beamline was focused with a dielectric 4-inch 30° off-axis parabolic mirror with the focal length  $f = 150$  mm (effective focal length  $f_{\text{eff}} = 160.8$  mm) onto a glass target. An AR-coated, 500- $\mu\text{m}$ -thick glass wafer was placed right in front of the parabola to protect it from possible debris from the target. Typical energy on the target was 700 mJ.

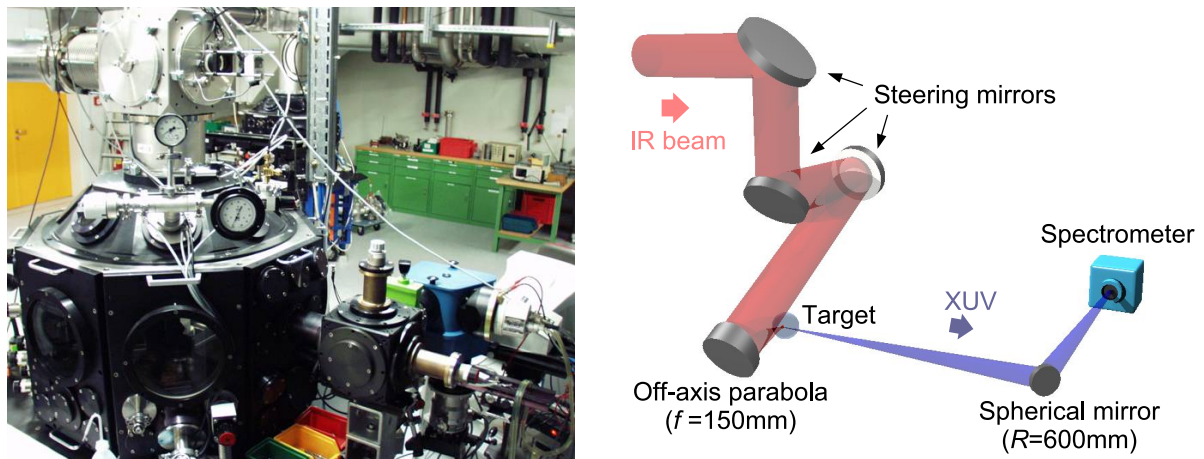


**Figure 4.2:** Photograph and drawing of the experimental chamber and the beamline. The beam coming from the beamline was focused onto a target with a off-axis parabola ( $f = 150$  mm) onto a solid target. The reflected beam was collected with a spherical mirror ( $R = 600$  mm) and sent into an XUV spectrometer.

The target was driven by four motorized stages (DRT65/LIMES60, OWIS). Since each laser shot destroys a part of the target surface, a rotation stage and a translation stage was used to provide a fresh part of the surface for each shot. It allowed approximately 5000 shots on one round target with the diameter of 120 mm, when the spacing between each shot was set to a typical value of 1.5 mm. The spacing was reduced to save the target when the incident energy was lowered, i.e., when the damage spot was smaller. Another translation stage is used for a focal scan along the incident beam axis. The other translation stage is used to move the whole target drive mechanism away from the beam to observe the beam profile at the focus.

During the alignment, the focus of the beam was imaged with a  $f = 100$  mm objective onto a beam profiler (WinCamD, DataRay), which was placed  $\sim 6$  m away from the focus. The alignment of the off-axis parabola was optimized by observing this image. Figure 4.3 shows a typical image of the focus after the optimization. The spot has an Airy pattern [110] because the profile of the incoming beam is flat-top. Energy distribution of the spot was analyzed from this image by calculating the energy within a circle with a certain radius. The blue circles in Fig. 4.3(b) shows the relative energy contents as a function of the radius of the enclosing circle.

To obtain an approximate focal intensity distribution, the plot is fitted to a double Gaussian profile. The power within a circle with radius  $r$  is calculated as

$$P(r) = P_0 \left[ \alpha \left( 1 - e^{-2r^2/w_1^2} \right) + (1 - \alpha) \left( 1 - e^{-2r^2/w_2^2} \right) \right], \quad (4.1)$$

where  $P_0$  is the peak power,  $w_1$  and  $w_2$  the  $1/e^2$  radii of the two Gaussian profiles, and  $\alpha$  the fraction into one of the Gaussian. Since  $P(r)$  is a “cumulative” power, the intensity profile of this beam is obtained as

$$I(r) = \frac{1}{2\pi r} \frac{dP}{dr} = P_0 \left( \frac{2\alpha}{\pi w_1^2} e^{-2r^2/w_1^2} + \frac{2(1-\alpha)}{\pi w_2^2} e^{-2r^2/w_2^2} \right). \quad (4.2)$$

If the temporal profile of the pulse is Gaussian, the peak power  $P_0$  is obtained as

$$P_0 = \sqrt{\frac{4 \ln 2}{\pi}} \frac{E}{\tau}, \quad (4.3)$$

where  $E$  is the total energy and  $\tau$  is the pulse duration. From the experimental values  $E = 700$  mJ and  $\tau = 45$  fs, together with the fitted parameters, the beam profile is obtained as shown in Fig. 4.3(b). The obtained peak intensity is  $\sim 4 \times 10^{19}$  W cm $^{-2}$ . On the other hand, the radius corresponding to  $1/e^2$  radius of Gaussian beam—where  $\sim 86\%$  of the energy is contained—is obtained as  $\sim 10$   $\mu$ m and from this value, the average intensity of the spot is calculated to be  $\sim 4 \times 10^{18}$  W cm $^{-2}$ . From this analysis, it is seen that the energy in the focal spot area with intensity  $< 4 \times 10^{18}$  W cm $^{-2}$  is  $\sim 55\%$ , while with intensity  $> 10^{19}$  W cm $^{-2}$  only  $\sim 30\%$ .

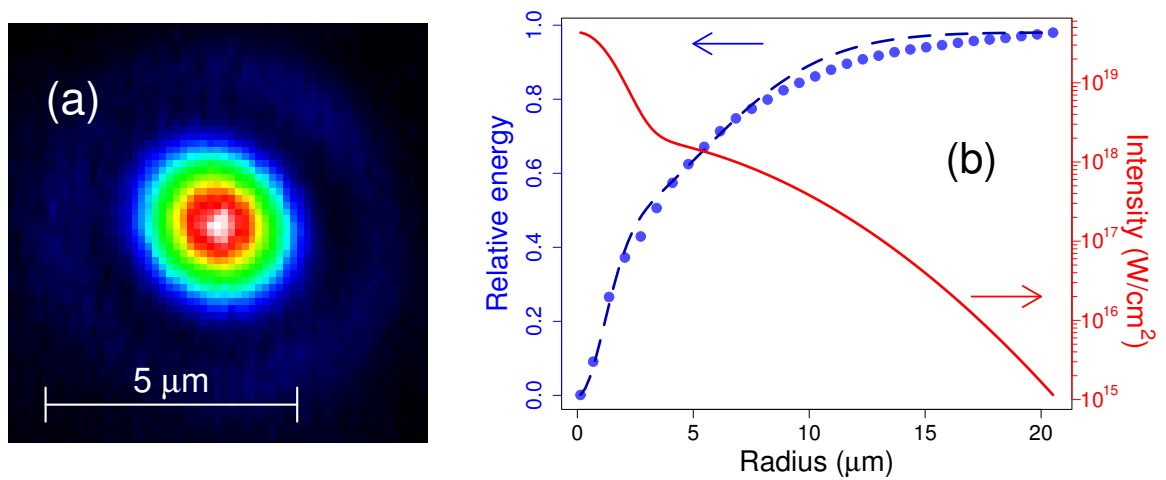
The reflected beam was collected with a gold-coated spherical mirror with a radius of curvature  $R = 600$  mm and sent into a 0.2 m vacuum monochromator (VM-502, Acton Research). The signal was detected with a multi-channel plate (MCP) with a phosphor screen and a CCD camera (CH350, Photometrics) and read out by a personal computer (PC).

Figure 4.4 shows a typical spectral image obtained with the setup. The image was taken with a single shot. Harmonics up to the 15th order are clearly observed. The observed spectral range was limited by the reflectivity of the gold focusing mirror and the efficiency of the grating.

### 4.1.3 Grazing-incidence spectrometer

Although it was possible to measure the spectra with the Acton spectrometer to a certain extent, it was not clear whether there is any signal above the observed spectral range. In fact, it is important to know the real XUV radiation because any unexpected radiation could be detrimental to some applications. Therefore, we made some modifications to the setup shown in Fig. 4.2. The first was to introduce a 1-m focal length scanning grazing incidence spectrometer (Model 248/310, McPherson). The advantage of the grazing incidence spectrometer is its high efficiency for the short wavelength. An MCP and a phosphor screen connected to a CCD camera (DH420, Andor) with a tapered fiber was chosen as the detector.

The spectrometer uses a Rowland-circle configuration [111], where the horizontal focusing of the vertical slit image is assured if the entrance slit and the detector are both located on the



**Figure 4.3:** Typical focal spot of ATLAS. (a) Image observed with a beam profiler. The spot shows an Airy pattern owing to the flat-top profile of the incoming beam. (b) Energy contents plotted as a function of a radius of the enclosing circle (blue dots). The blue dashed line shows a fit, where a double-Gaussian profile is assumed. From the fit, the intensity profile of the beam was calculated (red line).

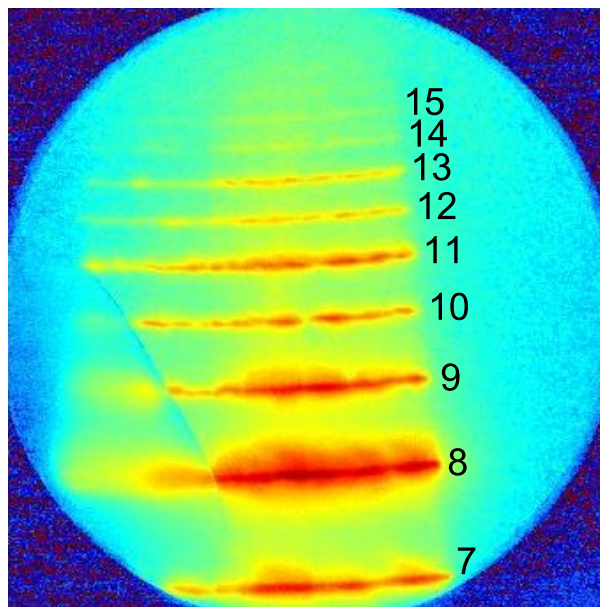


**Figure 4.4:** Typical image obtained with the setup. Harmonics up to 15th order is observed. The observed spectral range was limited by the reflectivity of the gold mirror and the efficiency of the grating.

Rowland circle. Figure 4.5 shows the configuration of the spectrometer. The reflection angle  $\theta$  is related to the incidence angle  $\alpha$  as  $d \sin \alpha - d \sin \theta = N\lambda$ , where  $d$  is the distance between the grooves of the grating,  $N$  is the diffraction order, and  $\lambda$  is the wavelength of the incident light. Figure 4.5 also shows that  $\cos \theta = x/r$ , where  $x$  is the chord length (distance between the grating and the center of the detector), and  $r$  is the grating radius, which is equal to the diameter of the Rowland circle. The detector is placed parallel to the tangent of the Rowland circle but intersects with the Rowland circle at two points so that the most of the rays are close to the focus. The position of the detector can be scanned along the Rowland circle to observe different wavelength ranges. The spectrometer is equipped with a counter that shows the chord length  $x$  in inches, and the conversion from  $x$  to the center wavelength  $\lambda$  on the detector is given as

$$\lambda = d \left[ \sin \alpha - \sin \left( \cos^{-1} \frac{x}{r} \right) \right]. \quad (4.4)$$

For our spectrometer, the parameters were  $\alpha = 87^\circ$ ,  $r = 998.8$  mm, and  $d = 1/133.6$  mm.

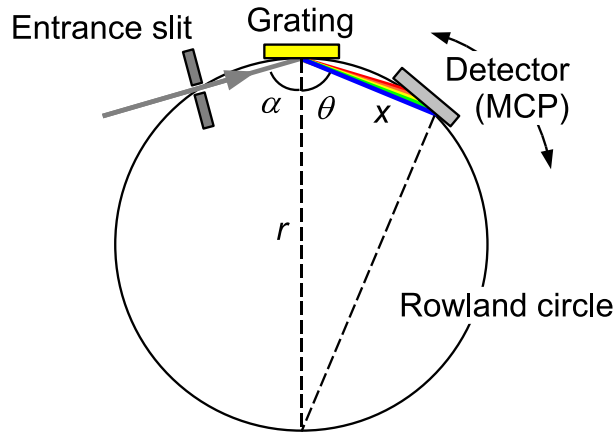


**Figure 4.5:** Configuration of the grazing-incidence spectrometer. The grating is placed tangential to the Rowland circle and has a radius of curvature equal to the diameter of the Rowland circle. The entrance slit and the detector are positioned on the Rowland circle. While the position of the slit is fixed, the detector can be scanned along the Rowland circle.

Another modification made was to attach the spectrometer directly to the chamber, so that the spectrometer is placed at the position of the spherical mirror in Fig. 4.2 and no reflection is involved before the spectrometer.

After those modifications, less signal was expected overall because there was no collecting optics any more. On the other hand, there is no component that truncates the short wavelength region of the spectra, thus we expect to obtain a clearer picture of what is generated at short wavelength region. Spectra measured with this modified setup will be presented and discussed in the next section.

## 4.2 Spectral properties and selection

As an XUV radiation source, one of the most important property is its spectral contents because many applications require specific wavelengths. For example, two-photon ionization of helium requires wavelength of the radiation to be longer than 50.4 nm. It is also important to take care of the fundamental wavelength reflected by the target and travels along with the generated harmonics, because the energy of the fundamental pulse is usually several orders of magnitude higher than that of the harmonics and hence easily disturbs further applications. In this section, methods to select a certain spectral region and to remove the unwanted wavelength component are described.

### 4.2.1 Spectral selection using various filters

The simplest way to select a spectral region is to use an appropriate filter. Metallic filters block IR beam, while transmitting a certain XUV spectral region depending on the material.

Figure 4.6 shows spectra measured with a 150-mm-thick aluminum filter. An aluminum filter was chosen because it transmits wavelength as short as 17 nm with high efficiency ( $\sim 80\%$ ) and it can be easily obtained from any manufacturer. The transmission curve of the filter is shown on the top [Fig. 4.6(a)]. Figure 4.6(b) shows a spectrum obtained at the center wavelength of 50 nm. The cutoff at 10th harmonic ( $\sim 80$  nm) is due to the low transmission of the aluminum filter. Figure 4.6(c) shows a spectrum at 50 nm. Harmonics up to 18th order is clearly seen. Besides the harmonic signals, the signal coming from the line emission from oxygen is also observed. Figure 4.6(d) shows a spectrum at 30 nm. Strong line emission from oxygen is observed around 20 nm. The sharp drop of the line emission signal is due to the X-ray absorption edge of aluminum (L-edge), which is located at 17 nm [112]. Spacing of the harmonics appears to change from Fig. 4.6(b) to Fig. 4.6(c) because the detector moves along the Rowland circle.

Figure 4.7 shows a vertically integrated profile of the image shown in Fig. 4.6(c). The harmonics up to 19th order were clearly observed, which was impossible with the Acton spectrometer. The signal around 30 nm is due to the scattered light that hits the edge of the MCP and the tapered fiber and thus has no physical significance. The harmonic signal lies on top of the slope of the second-order oxygen line emission signal. An important thing to note is that the oxygen line emission produced a signal comparable to harmonics, even for second-order diffraction. Its high photon energy will be adverse for further applications such as two-photon ionization of helium, if this radiation is not properly suppressed. Since aluminum has high transmission down to 17 nm, where the oxygen line lies, it does not make an appropriate filter for that purpose.

Fortunately, there exist other materials that suppress the spectral region around 20 nm efficiently. Indium, for example, is one of them. Figure 4.8 shows the transmission curve of indium and spectra measured with an indium filter. The indium filter transmits harmonics from 8th to 10th efficiently, while suppressing the radiation around 20 nm by 5 orders of magnitude. The spectra observed with a 150-nm-thick indium filter shows strong signals for 8th to 10th harmonics, a weak signal for 11th harmonic, and no signal for oxygen line emission. A tin filter is another possibility. Figure 4.9 shows the transmission curve of tin and spectra measured with a 150-nm-thick tin filter. The tin filter transmits 10th to 15th harmonics, which is consistent with

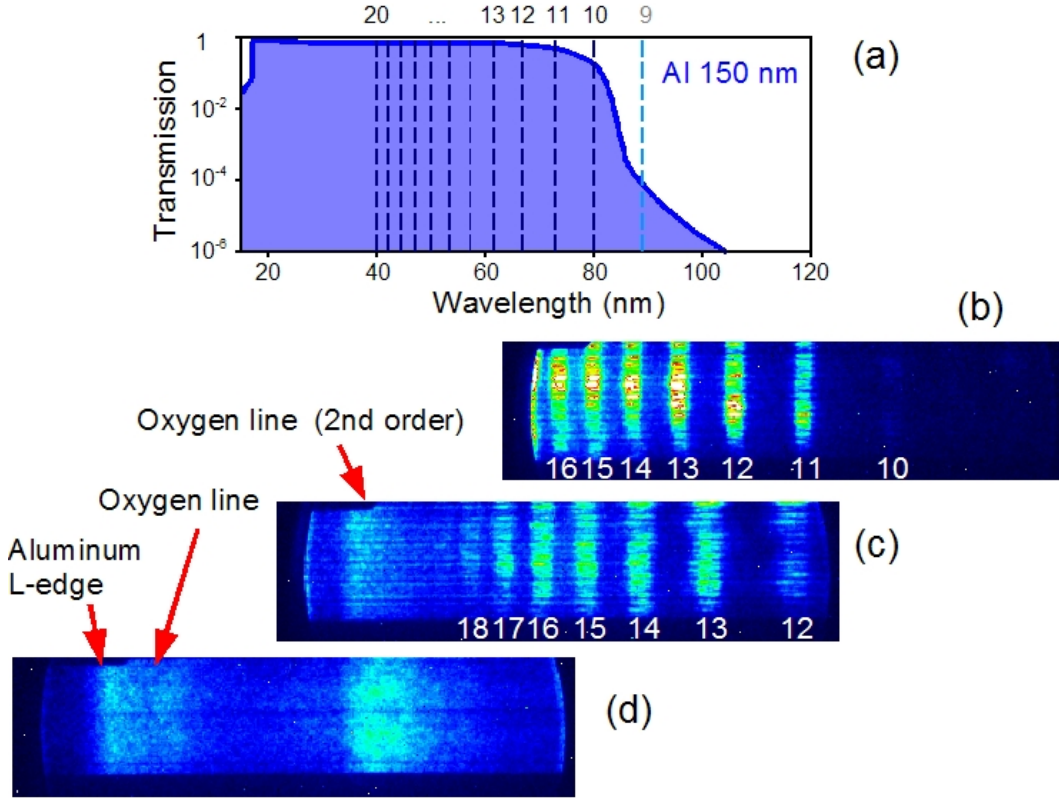


**Figure 4.6:** Spectral images measured with an aluminum filter. The transmission curve of a 150-nm-thick aluminum is shown on the top (a). The spectral images are taken at the center wavelengths of (b) 70 nm, (c) 50 nm, and (d) 30 nm. A strong signal from line emission of oxygen is also observed.

the observed spectra. No signal from oxygen line is observed.

### 4.2.2 Comparison of various targets

Another possibility to confine the spectral region of harmonic emission is to use a different target. This method works only for the CWE, where maximum harmonic order is limited by the plasma density, as explained in Section 2.2.2.

#### Fused silica

So far, all the spectra are taken by using fused silica as the target. Since the density of fused silica is  $2.21 \text{ g cm}^{-3}$  [113], the maximum electron number density expected from the fused silica ( $\text{SiO}_2$ ) is

$$n_e = 2.21 \cdot \frac{14 + 8 \times 2}{28 + 16 \times 2} \cdot 6.02 \times 10^{23} = 6.65 \times 10^{23} \text{ cm}^{-3},$$

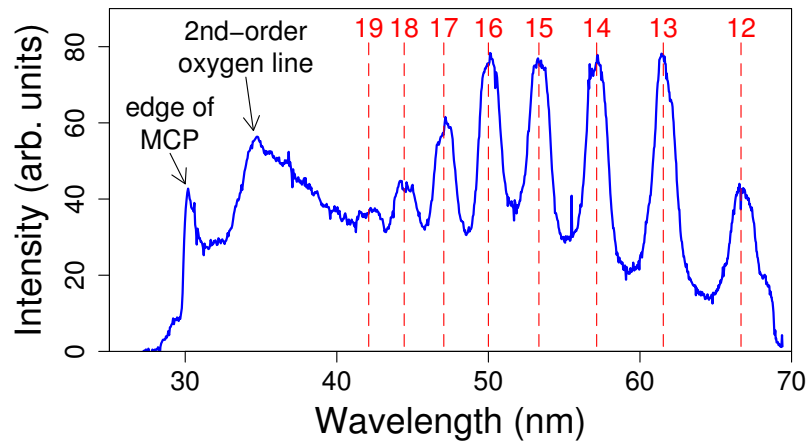


**Figure 4.7:** Spectrum obtained with an aluminum filter. The harmonics up to 19th order is observed. A strong signal from the second-order diffraction of oxygen line is also observed. The signal at the left end is scattered light hitting the edge of the MCP and tapered fiber.

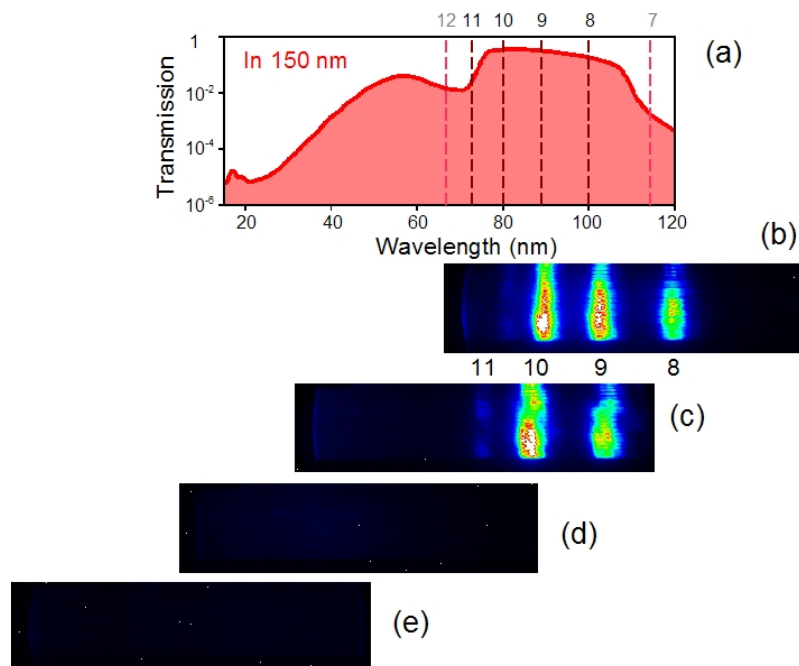


**Figure 4.8:** Spectra measured with an indium filter. Transmission curve of a 150-nm-thick indium filter is shown on the top (a). Spectra are measured at (b) 90 nm, (c) 70 nm, (d) 50 nm, and (e) 30 nm.

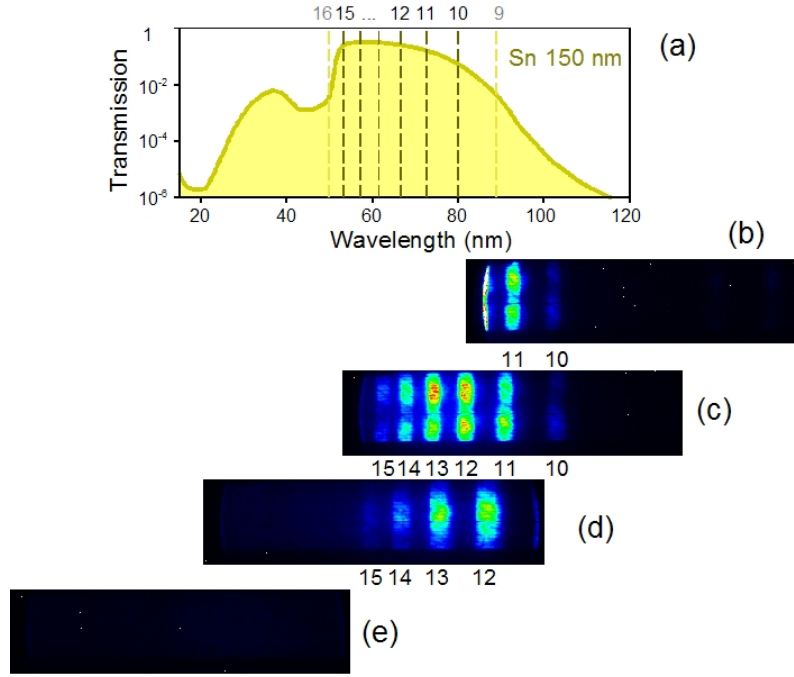


**Figure 4.9:** Spectra measured with a tin filter. Transmission curve of a 150-nm-thick tin filter is shown on the top (a). Spectra are measured at (b) 90 nm, (c) 70 nm, (d) 50 nm, and (e) 30 nm.

when the fused silica is fully ionized. This number density corresponds to the plasma frequency of

$$\omega_p = \sqrt{\frac{n_e e^2}{\epsilon_0 m_e}} = \sqrt{\frac{6.65 \times 10^{23} \times (1.602 \times 10^{-19})^2}{8.85 \times 10^{-12} \times 9.11 \times 10^{-31}}} = 4.60 \times 10^{16} \text{ Hz.}$$

Since the frequency of the fundamental field at 800 nm is  $\omega_0 = 2\pi c/\lambda = 2.35 \times 10^{15}$  Hz, this plasma frequency satisfies  $\omega_p \approx 19.5\omega_0$ . Therefore, the maximum harmonic order expected from CWE using a fused silica target is 19th order.

This is exactly the maximum order observed experimentally, and this suggests that the harmonics generated from the experiment might come from CWE and not ROM. Note that this coincidence does not necessarily exclude the possibility that the harmonics are generated from ROM. To find whether they are generated from CWE or ROM, the easiest way is to change the target with a material with lower density and see whether the cutoff position changes.

### Plexiglas

When the target is changed to Plexiglas (polymethylmethacrylate), whose molecular formula is  $(C_5O_2H_8)_n$  and density is  $1.19 \text{ g cm}^{-3}$  [113], the maximum electron number density is reduced to  $3.58 \times 10^{23} \text{ cm}^{-3}$  and the maximum plasma frequency becomes  $\omega_p \approx 14.3\omega_0$  accordingly.



Therefore, if no harmonic is observed above the 14th order with the same experimental condition, it indicates that the harmonics are generated from CWE.

Figure 4.10 shows the spectra obtained with glass and Plexiglas. For those spectra, the signals were accumulated for 100 laser shots each. For the glass target [Fig. 4.10(a)], the harmonics up to 16th order was observed, which is consistent with the results shown before. On the other hand, no harmonic above 14th order is observed when the target was changed to Plexiglas [Fig. 4.10(b)]. Since the laser condition is practically the same for those two measurements, the difference in the spectra is attributed to the difference in the material density. This means that those harmonics are generated from the CWE process.

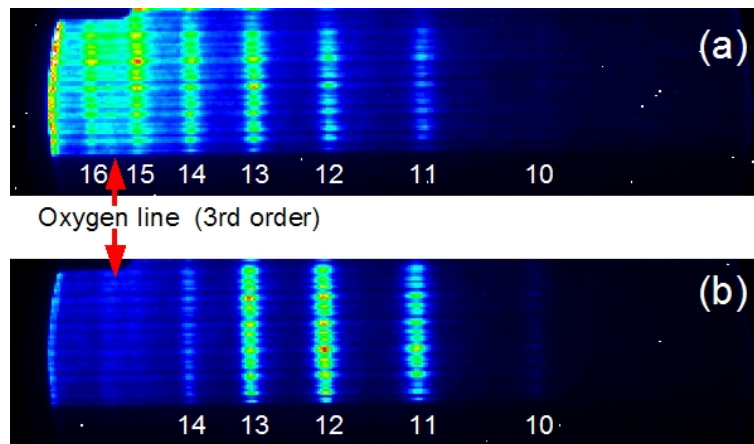


**Figure 4.10:** Comparison between the spectra taken with (a) glass and (b) Plexiglas at the center wavelength of 70 nm using an Al filter. Harmonics as high as 16th order is observed for a glass target, while no harmonic above 14th order is observed for a Plexiglas target.

This result suggest that it is possible to suppress harmonic generation above 14th order by using Plexiglas target, which is helpful for future applications such as two-photon ionization of helium, discussed in Section 5.1.2.

The result also suggests that no ROM harmonic is generated, although the estimated average intensity of  $4 \times 10^{18} \text{ W cm}^{-2}$  is already in relativistic regime. One of the possible explanation is that the contrast of the laser pulse was not high enough for ROM process. For relativistic interaction to take place, not only the intensity but also the plasma scale length plays a role [60]. In fact, ROM harmonics have been observed with laser pulses with higher contrast [59, 114], while no ROM harmonic has been observed with lower-contrast laser pulses at relativistic intensity [28, 31]. Compared to the CWE process, which occurs within the plasma density profile, the ROM process is bounded to the surface and requires a clean, well-defined vacuum-plasma interface [33].

Thus I conclude that most of the harmonics generated with ATLAS is generated from CWE process. The main harmonic generation process is considered to be CWE for the rest of the experiments presented in this thesis.

### Silicon

One thing to note is that harmonic generation efficiency was very low when silicon was used as a target. Since silicon has a density of  $2.33 \text{ g cm}^{-3}$  [113], which is comparable to that of the fused silica, at least the same number of harmonics are expected theoretically. Figure 4.11 shows the spectra observed from a silicon target with and without a 150-nm-thick aluminum filter. Although some harmonics were still generated, they were so weak that they were not observable when the aluminum filter was used, i.e., when the condition was the same as the previous measurement with a glass target shown in Fig. 4.6. The oxygen lines are most probably coming from the contamination layer on the surface of the target.

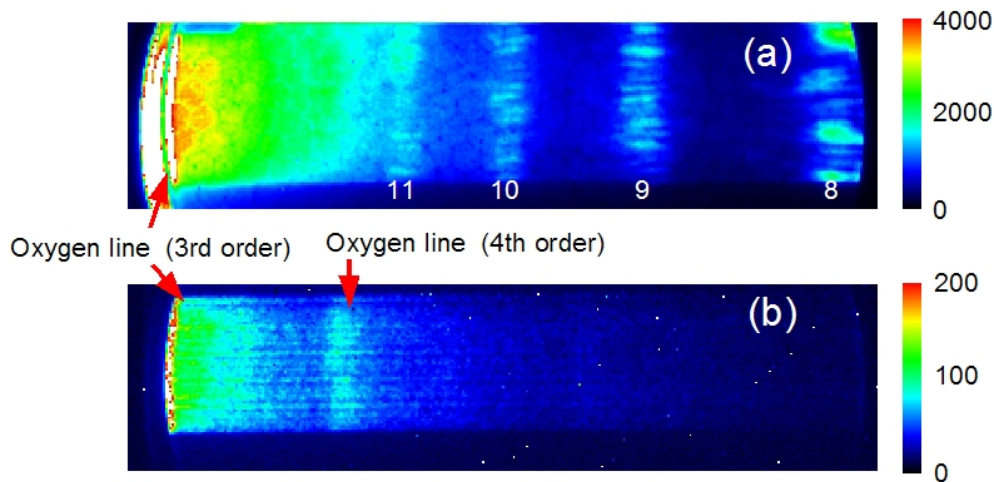


**Figure 4.11:** Spectra measured from a silicon target at the center wavelength of 80 nm (a) without and (b) with an Al filter. Note that the color scales are different for the two images.

The reason why the harmonic emission was weak is explained in terms of the contrast of the pulse and the plasma mirror effect. The main difference between fused silica and silicon is the absorptivity of the material. The fused silica is practically transparent to IR, while the silicon is not, i.e., it absorbs IR. This means that more energy from the pedestal of the pulse is absorbed by silicon and that leads to earlier formation of the preplasma on the target. The fused silica, on the other hand, does not absorb the energy on the pedestal efficiently, which is exactly the same process as the plasma mirror and thus the effective contrast for the interaction is increased. Since the contrast improvement by a plasma mirror increases the harmonic generation efficiency significantly [33, 48], the main reason for the low harmonic generation efficiency with the silicon target is attributed to the low effective contrast.

### 4.2.3 Suppression of infrared

Since the process of the surface HHG requires very high intensity, extra care should be taken with the remaining IR after the interaction because its extremely high intensity can easily ruin further applications.

The simplest method to attenuate the IR is to use a metallic filter. Any of the filters mentioned in Section 4.2.1 suppresses the fundamental wavelength by several orders of magnitude. Although the metallic filters are sufficient for moderate intensities like  $\sim 10^{14} \text{ W cm}^{-2}$ , it is not ideal for the energy used for surface HHG experiment. One of the problems is that the IR is so intense that it easily damages the filters. In fact, several pinholes have been found in some of the filters after several laser shots.

One possibility is to use the reflection from a silicon plate at the Brewster angle for the fundamental wavelength [115]. Figure 4.12 shows the reflectivity curve of silicon for  $p$ -polarization at  $74.83^\circ$  incidence angle. While the reflectivity of the fundamental wavelength of 800 nm is approximately  $10^{-6}$ , the reflectivity at the region of interest—between 8th to 15th harmonics—is close to unity. In other words, this “reflective filter” allows to suppress IR with a very high efficiency and with high throughput. It is possible to use multiple silicon plates to achieve higher IR suppression.

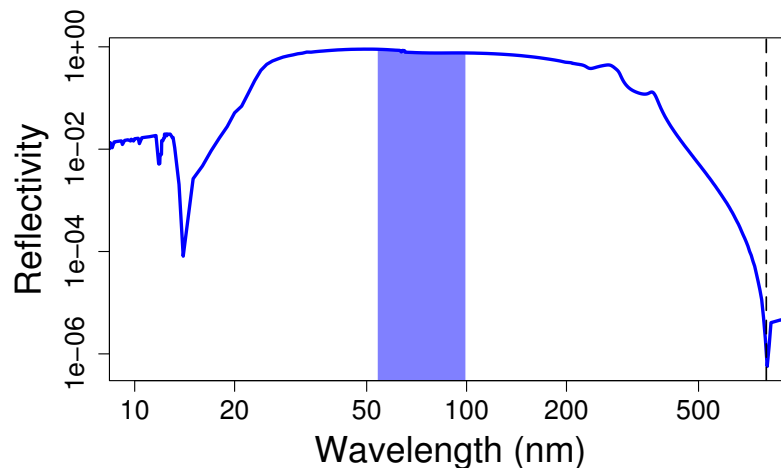


**Figure 4.12:** Reflectivity of silicon for  $p$ -polarization at  $74.83^\circ$  incidence angle. The vertical dashed line indicates the fundamental wavelength of 800 nm and the filled region indicates the region between 8th to 15th harmonics.

In practice, the suppression ratio depends strongly on the alignment of the plate. In fact, a small portion of  $s$ -polarized component increases the reflectivity significantly because the Brewster angle works only for  $p$ -polarization, and the reflectivity for  $s$ -polarization at the same incidence angle is as high as  $\sim 75\%$ . If the pulse contains  $s$ -polarized component with 1% of the pulse energy, for example, the reflectivity increases to  $\sim 7.5 \times 10^{-3}$ , which is almost 4 orders worse than the best case. It is also important to note that the plate needs to be replaced once in a while because the energy of IR is not transmitted but absorbed by the plate, which leads to a burn spot on the surface if the IR energy is high, and deteriorates the XUV reflection.

Other materials can be also used. For example, higher IR suppression is expected with silicon carbide at the price of lower XUV throughput [115]. Use of AR-coated dielectric plates has been

also reported [59].

### 4.3 Spatial profile

Spatial property of the radiation is important when one aims for high XUV fluence/intensity. There is a huge difference in efficiency whether the radiation is emitted in one direction as a beam or in any  $4\pi$  direction. It is also important to know the divergence of the radiation for collecting the radiation for further applications.

To find the divergence of the radiation, the XUV signal was measured by placing an absolutely calibrated XUV diode (AXUV100In/MgF<sub>2</sub>, IRD) in the specular direction and scanning it vertically and horizontally with two motorized translation stages (LM60, OWIS). The diode was mounted in a box with a 5-mm-diameter circular aperture. Figure 4.13 shows the experimental setup used for the measurement. Everything was placed inside the vacuum chamber. Although the diode was already equipped with an indium filter, an extra 300-nm-thick indium filter was placed in front of the diode to suppress as much IR as possible. To measure the remaining background signal from IR, a 5-mm-thick glass piece that can be moved in and out of the beam was placed in front of the filter to make it possible to block the XUV completely and let only the IR through.

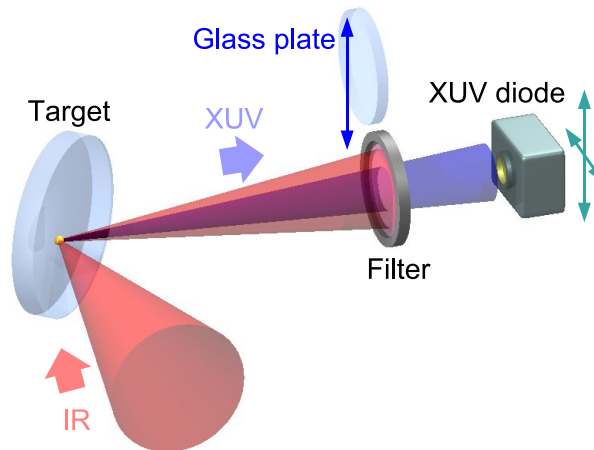


**Figure 4.13:** Setup for the measurement with XUV diode. The XUV diode is mounted on two translation stages to allow scanning in vertical and horizontal direction.

The signal was measured with and without the glass piece. The signal measured with the glass piece corresponds to the background signal from IR, while the signal measured without the glass piece corresponds to the XUV signal, possibly with IR background. To obtain the net XUV signal, the signal measured with the glass piece was subtracted from the signal measured without the glass piece. The results are shown on Fig. 4.14. The blue circles represent the net XUV signal after background subtraction. The background IR signal is also shown on the graphs for comparison. The range of the measurement was limited by the travel of the translation stages.

The Gaussian fits onto the IR signals show a rough estimate of the profiles of the reflected IR beam.

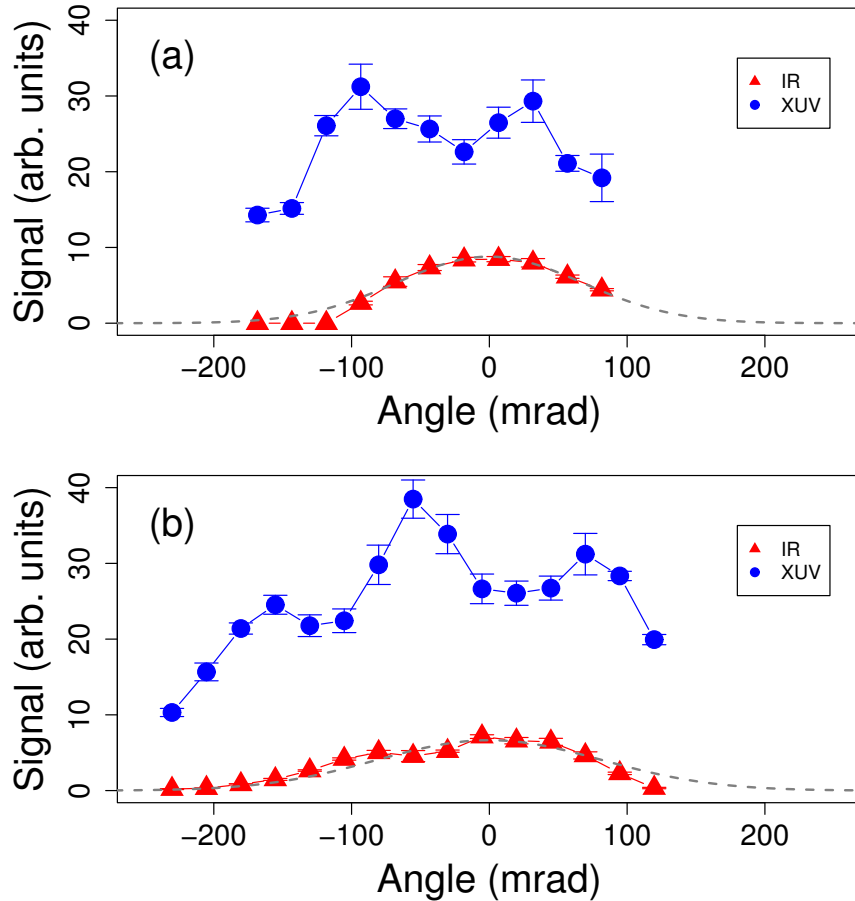


**Figure 4.14:** Divergence measurement with an XUV diode. The diode was scanned (a) vertically and (b) horizontally. Blue circles and red triangles represent the signal from XUV and IR, respectively. The gray dashed lines is the Gaussian fit to the IR background, showing the divergence of the reflected IR.

The results shown on the graphs suggest that the harmonic emission has approximately the same order of divergence angle as the reflected IR. However, the measured divergence is not very accurate because the observed range was limited. There is also a possibility that an extra background was added by electrons generated in the plasma and emitted in the specular direction.

Therefore, the spatial profile of the XUV beam was measured with another setup shown in Fig. 4.15. To make sure that the whole beam is collected, a gold-coated, 1-inch  $30^\circ$  off-axis parabola ( $f = 50$  mm,  $F = 2$ ) was placed after the target. The collection angle of this recollimating parabola is larger than that of the focusing parabola, i.e., all the reflected light should be collected with this parabola. The collected beam was sent through three reflections

from silicon wafers (two reflections at the Brewster angle, one reflection at  $60^\circ$ ) to suppress IR. A 150-nm-thick indium filter was placed in the beam to select 8th to 10th harmonics. A 5-mm-thick piece of glass was also placed in the vacuum chamber so that the background signal from IR can be measured. Both the indium filter and the glass piece were mounted on flipper mounts so that they can be moved in and out of the beam. The signal was detected with an MCP with a phosphor screen and the image was observed with a CCD camera (CH350, Photometrics).

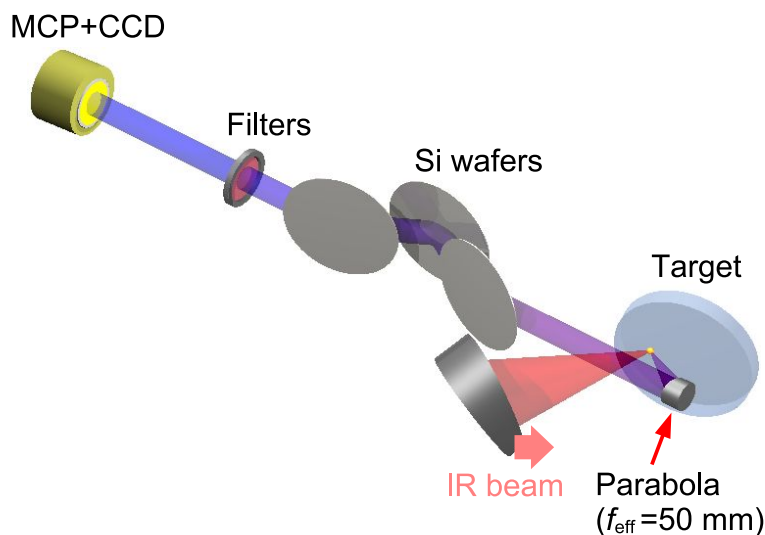


**Figure 4.15:** Setup for spatial profile measurement. The IR beam was focused onto the target with the off-axis parabola ( $F = 2.5$ ). The reflected beam was collected with a gold-coated parabola ( $f = 50$  mm,  $F = 2$ ). The beam was sent through three silicon wafers and filters to suppress IR. The beam was detected with an MCP with a phosphor screen and observed with a CCD camera.

The measured beam profiles are shown on Fig. 4.16. Figures 4.16(a–c) are the profiles of reflected IR beam, measured with the glass piece in the beam. The white dotted circles indicate the edge of the MCP. Red dashed circles are placed to show the diameter of the IR beam. It can be seen that the MCP is slightly larger than the re-collimated IR beam. Figures 4.16(d–f) are the profiles of XUV beam measured with the indium filter. The position of the beam was shifted upwards for images (c) and (f) to make sure that there was no clipping at the bottom. No signal was observed when both the glass piece and the indium filter was placed in the beam. In other words, there is no background signal coming from IR for images (d–f). The top-left corner of each image has a line and is blurred because the tapered fiber between the MCP and the CCD was chipped.

The profile of the XUV beam is clearly smaller than the red circle—the diameter of the collected IR. To analyze the data quantitatively, the diameter of the XUV beam profile is calculated by taking the root-mean-square (RMS) distance from the centroid. If the beam profile is Gaussian, the RMS distance corresponds to  $1/e$  radius (see Appendix A.1.3). From this value, the FWHM of the XUV beam is estimated to be 12 mm, as compared to 24 mm of IR diameter.

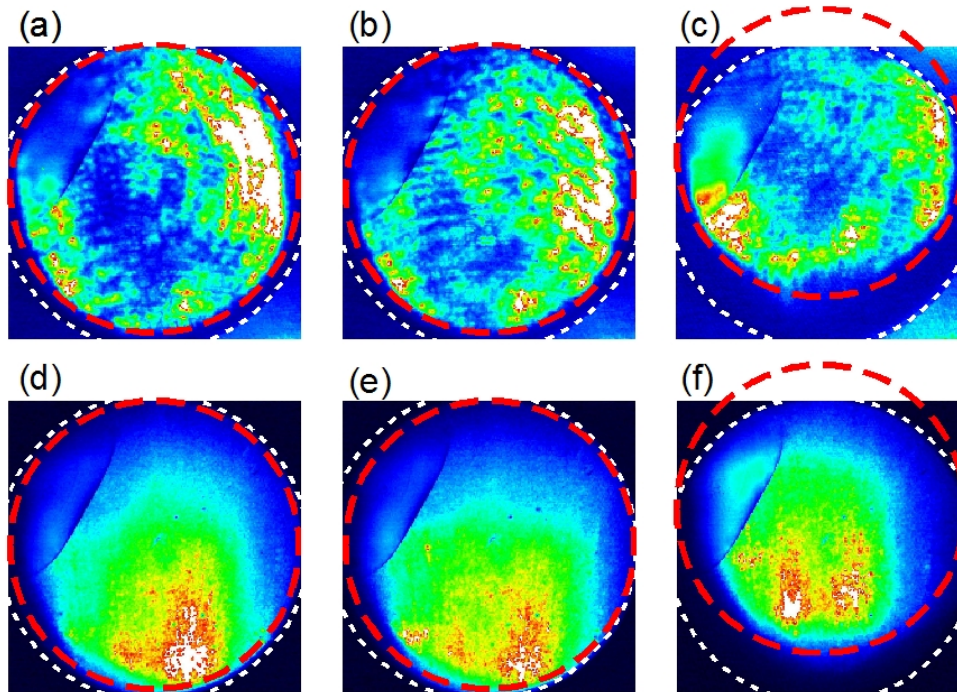


**Figure 4.16:** Measured beam profile of (a–c) IR and (d–f) XUV. White dotted circles indicate the edge of the MCP. Red dashed circles show the diameter of the IR beams. Position of the beam was shifted upwards for images (c) and (f) to make sure that there is no clipping at the bottom. The line and the blur at the top-left corner of each image is coming from the chipped fiber taper between the MCP and the CCD.

Therefore, the diameter of the XUV beam (8th to 10th harmonics) is approximately half of the diameter of IR, which is comparable to the result of another work [59]. This result shows that the generated harmonics have acceptable spatial coherence.

However, the profile of the XUV beam is not as smooth as the one reported in Ref. [59]. The most probable reason for that is the difference in the contrast of the incident laser pulse, where they had a double plasma mirror setup and had a contrast two orders of magnitude better than that of ATLAS. The difference of the contrast by two-orders of magnitude resulted in more distorted plasma–vacuum interface, which deteriorated the profile of the generated XUV beam.

## 4.4 Efficiency

To find the possibility of the surface HHG as an XUV radiation source, it is important to determine the conversion efficiency. Here the harmonic generation efficiency is estimated in the context of the next experiment, volume autocorrelation using two-photon ionization of helium (presented in Chapter 5).

Figure 4.17 shows the experimental setup. Most of the setup is same as the setup for the

experiment shown in Fig. 5.2. The IR beam is focused onto a Plexiglas target and the reflected beam is collected by a gold-coated, 90° off-axis parabola ( $f = 75$  mm, effective focal length  $f_{\text{eff}} = 150$  mm). Since the  $F$ -number of this parabola is  $F = 6$  and the  $F$ -number of the incident IR beam is  $F = 2.5$ , not all part of the reflected IR beam is collected. On the other hand, the diameter of the XUV beam is approximately half of that of the IR beam and a large amount of XUV beams should be collected. The collected beam is reflected by a glass plate at 60° incidence angle, which is close to the Brewster angle of 800 nm. The harmonics of 8th order and higher are selected with a 150-nm-thick indium filter. A 5-mm-thick glass piece is placed in the chamber to be able to block the XUV signal, which enables to measure the background signal from IR. The XUV signal is detected with an absolutely calibrated XUV diode (AXUV576C, IRD), which has a 1-inch square detector chip, and amplified with a signal amplifier (PA100, IRD). The output signal from the amplifier is measured with an oscilloscope (TDS3054B, Tektronix).

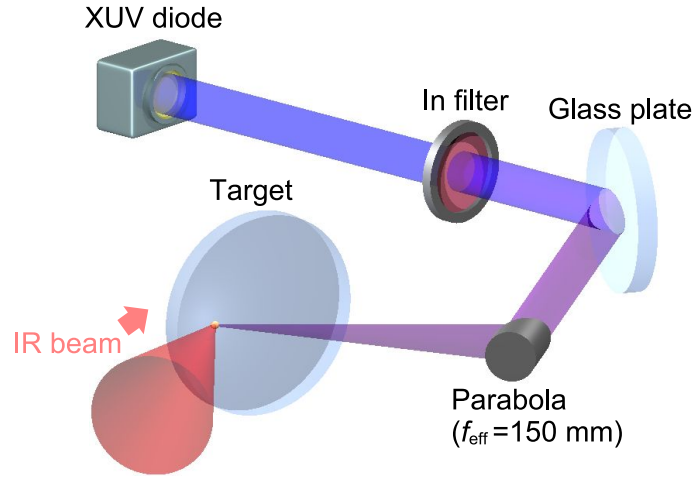


**Figure 4.17:** Experimental setup for efficiency measurement. The IR beam is focused onto the target. The reflected beam is collimated with a  $f_{\text{eff}} = 150$  mm parabola, reflected by a glass plate, and sent through a 150-nm-thick indium filter onto an XUV diode.

The typical signals obtained from the diode are shown in Fig. 4.18. The area under the curve corresponds to the electrons generated by the diode. The red curve was measured with both the indium filter and the glass piece in the beam, i.e., the background signal generated purely from IR. The blue curve was measured only with the indium filter in the beam. The difference between the blue curve and the red curve corresponds to the signal generated from XUV.

The absolute XUV energy is calculated as follows. The charge  $Q$  generated at the diode is obtained by

$$Q = \int I dt = \frac{1}{R} \int V dt, \quad (4.5)$$

where the integral of the last term is equal to the area under the curve. The signal amplifier was used in a setting corresponding to the value of  $R = 5000$ . Therefore, the absolute charge



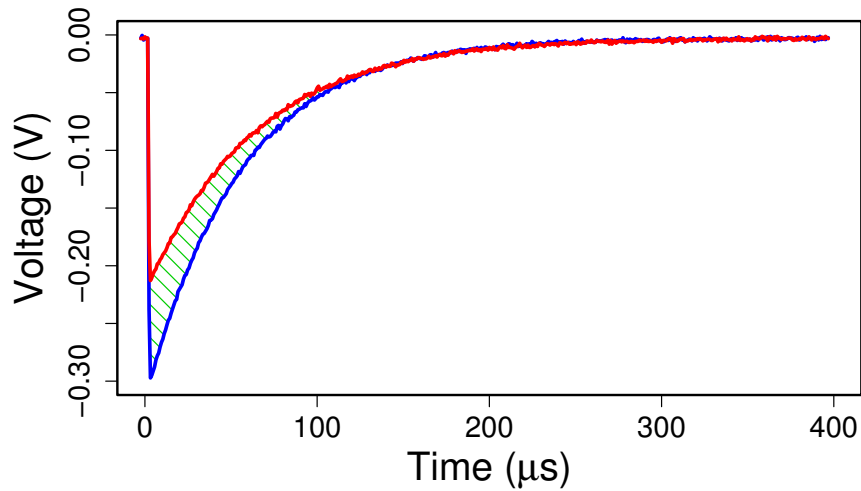


**Figure 4.18:** Typical signal measured from an XUV diode. The signals are average over 10 laser shots and measured with (red curve) and without (blue curve) the glass piece in the beam. The hatched area corresponds to the electrons generated by XUV.

generated in the diode is the hatched area in Fig. 4.18 divided by 5000, which is obtained to be  $(1.9 \pm 0.3)$  nC. To determine the photon energy from this value, the contributions from each harmonic must be considered separately. Although the spectrum consists of harmonics between 8th to 14th, here I neglect harmonics from 11th to 14th because the energies of those harmonics after the In filter is more than an order of magnitude lower than 8th to 10th harmonics. The procedure to obtain the contribution from each harmonic is summarized in Table 4.1.

**Table 4.1:** Summary of the procedure to obtain the contribution from each harmonics.

harmonic order	8th	9th	10th
quantum efficiency	1.6	1.9	2.3
relative energy in spectrum	1.0	1.5	1.7
contribution to the generated charge	1.60	2.85	3.91
charge generated at the diode / nC	0.364	0.648	0.888
number of electrons at the diode	$2.27 \times 10^9$	$4.04 \times 10^9$	$5.54 \times 10^9$
photon number at the diode	$1.42 \times 10^9$	$2.13 \times 10^9$	$2.41 \times 10^9$
single photon energy / nJ	$1.99 \times 10^{-9}$	$2.23 \times 10^{-9}$	$2.48 \times 10^{-9}$
total energy / nJ	2.82	4.74	5.98
total energy on the diode	13.5 nJ		

The quantum efficiency of the diode is provided by the manufacturer. The ratio of the en-

ergy of each harmonic signal was obtained from a typical spectrum shown in Fig. 4.8. The contribution to the charge generated in the diode is calculated by the product of energy of each harmonic and quantum efficiency. This ratio is used to divide the previously calculated value of charge 1.9 nC at the diode. Number of electrons is readily obtained by dividing these values by the charge of single electron  $e = 1.60 \times 10^{-19}$  C. The number of photon generated in the diode is calculated by dividing the electron number by the quantum efficiency. From these numbers, energy of the each harmonic on the diode is calculated. The total XUV energy on the diode is calculated to be 13.5 nJ.

To find the harmonic conversion efficiency, the reduction of the energy from the target to the diode must be considered. There is a number of components in the path from the target to the diode that reduce the energy of the harmonics, namely, reflection on the gold off-axis parabola at  $45^\circ$  incidence angle, reflection on the glass plate, and transmission of the indium filter. The transmission of those components are summarized in Table 4.2. Since the diameter of the parabola is 5/12 of the IR beam, it is approximately 5/6 of the FWHM of the XUV beam. If the XUV beam profile is assumed to be Gaussian, the energy contained within this radius is estimated to be 38% (see Appendix A.1.1). From these values, the energy of 8th, 9th and 10th harmonic generated on the target is estimated to be 14.5  $\mu$ J, 11.6  $\mu$ J, and 14.9  $\mu$ J, respectively. Since the typical energy on target was 700 mJ, the generation efficiency for 8th to 10th harmonic is estimated to be  $6 \times 10^{-5}$ .

**Table 4.2:** Transmission of the components between the target and the diode.

harmonic order	8th	9th	10th
gold parabola ( $45^\circ$ )	0.064	0.063	0.059
glass plate ( $60^\circ$ )	0.043	0.055	0.053
150-nm-thick In filter	0.182	0.310	0.339
overall transmission	$0.50 \times 10^{-3}$	$1.07 \times 10^{-3}$	$1.06 \times 10^{-3}$

From the XUV energy of 13.5 nJ on the diode, the intensity in the further application is also estimated. With a  $R = 300$  gold-coated mirror at near normal incidence,  $\sim 13\%$  of the energy is reflected. If you assume the pulse duration to be the same as the IR and the spot size to be  $10 \mu\text{m}$ —derived from a simulation (see Appendix B for detail)—the peak intensity of the focused XUV beam is estimated to be  $\sim 3.2 \times 10^{10}$  W  $\text{cm}^{-2}$ . This intensity should be sufficient for detecting helium ions from two photon ionization process [116, 117].

## 4.5 Summary

In this chapter, I have presented the characterization of the harmonics generated from solid targets and discussed the results in the context of using the generated harmonics in further applications

With the ATLAS laser system, harmonics up to 19th order was observed from glass targets. It is also found that there was a strong contribution from the line emission of oxygen, which should be taken care of before using the generated XUV radiation. This line emission was properly

suppressed by using appropriate filters and/or changing the target material to Plexiglas. This result also indicates that the harmonics generated in this setup is mainly from CWE process.

The spatial profile and divergence of the beam is studied because they are crucial for further applications where the beam must be sent far from the target, where they are generated. The collected XUV beam had a nice beam profile. The divergence of the generated harmonic beam is found to be approximately half of the reflected IR beam, which is helpful when the collection optics needs to be placed far from the source.

Efficiency of the harmonic-generation process is estimated by using an absolutely calibrated XUV diode. The efficiency of the harmonic generation for 8th to 10th order is estimated to be  $6 \times 10^{-5}$ . The intensity of the focused XUV beam in a realistic setup is estimated to be  $\sim 3.2 \times 10^{10} \text{ W cm}^{-2}$ , which should be sufficient for the next experiment, the volume autocorrelation using two-photon ionization of helium.



# Chapter 5

## Volume autocorrelation of harmonics by two-photon ionization of helium

In this chapter, I present the experiment of volume autocorrelation using two-photon ionization of helium to characterize the temporal structure of the generated harmonic radiation. The background for temporal characterization of harmonic radiation and the technique of volume autocorrelation is described in detail first. Then the experimental demonstration of two-photon ionization of helium is presented. This nonlinear process was used for measuring autocorrelation to characterize the temporal features of the generated harmonics, which is the main results of this work and discussed thoroughly.

### 5.1 Temporal characterization of XUV radiation

#### 5.1.1 Attosecond pulse characterization techniques

One of the most challenging tasks in the study of harmonic generation process is the characterization of the temporal structure of the generated harmonics. The most of the problems come from the lack of optics in XUV region and low intensity of generated XUV radiation, which make it difficult to apply the common techniques used in the visible region. Nevertheless, many studies have proposed and demonstrated the methods to characterize the duration of XUV pulses generated with gas harmonics.

Some methods can be classified as cross-correlation type. A technique called RABITT [16] uses the fundamental electric field to produce sidebands in the photoelectron spectra generated with XUV photons. The average duration of the pulses within a train of attosecond pulses was characterized by observing the interference between the sidebands. Another technique known as streak camera [1, 118] uses the fundamental electric field to “dress” the energy distribution of photoelectron generated by XUV photons. This modulation in the photoelectron spectrum was used to determine the duration of the isolated attosecond pulses [1, 18].

Another class of methods is based on autocorrelation. Those methods typically use XUV photons to trigger nonlinear processes such as two-photon ionization (TPI). Several different

materials and different ionization processes are demonstrated such as TPI of helium [17, 119], two-photon above-threshold ionization (ATI) of helium [120, 121, 122], two-photon double ionization of helium [123], and two-photon ATI of argon [122]. The ion species were determined by ion mass spectroscopy for the most of the cases [17, 119, 123]. For ATI methods, photoelectron spectroscopy was used instead [120, 121, 122].

There were also some proposals and demonstrations to extend full pulse characterization methods used in visible wavelength region such as frequency-resolved optical gating (FROG) [124] and spectral phase interferometry for direct electric-field reconstruction (SPIDER) [125]. This class of methods include FROG using two-photon ATI as the nonlinear process [126], FROG for complete reconstruction of attosecond burst (FROG CRAB) [19, 127], and XUV SPIDER [128, 129].

All the methods mentioned above are demonstrated with gas HHG process. Here I discuss the feasibility of those methods to our experiment. For our 45 fs pulse produced by ATLAS, it is more likely that the generated XUV pulse is a train instead of a single pulse. Therefore, it is better to use the method that works with a train. RABITT, for example, is meant to characterize a train of attosecond pulses. Unfortunately it is not straightforward to apply RABITT to surface HHG process because not only odd harmonics but also even harmonics are generated from surface HHG process. These even harmonics will appear at the same position as the sidebands generated in RABITT process, which makes it difficult to unfold the necessary information. Autocorrelation using two-photon ionization process is directly applicable to the surface HHG process. The drawback of this technique is that usable photon energy is strictly limited by the target medium and the process. In other words, different medium or different process is needed to observe different wavelength region. Full characterization would be an ideal solution, but generally they require rather complicated setups and accumulation of a large number of shots. It should be noted that preparing two replicas of XUV pulses necessary for many of the methods is not trivial for surface HHG because it is not clear if the method used for gas HHG works. A typical method in gas HHG is to produce harmonics from a double pulse, but it does not necessarily produce identical XUV pulses for surface HHG because of the complicated interaction between the laser pulse and the plasma.

From the above considerations, the volume autocorrelation using two-photon ionization was chosen for our experiment. This technique certainly has a limitation to the applicable XUV energy. On the other hand, the required setup is rather simple, consisting of a split mirror and a time-of-flight (TOF) setup. It also has an advantage that splitting and delaying of the XUV pulse by the split mirror is not affected by the harmonic generation process. These simplicity and direct applicability to surface HHG make it suitable for the first attempt to characterize the temporal structure of harmonics generated from solid targets.

### 5.1.2 Volume autocorrelation

The method of volume autocorrelation was demonstrated by Tzallas *et al.* [17] to characterize a train of attosecond pulses generated by gas HHG. Figure 5.1 illustrates the scheme of volume autocorrelation. After the harmonics are generated, a metallic filter is used to suppress the IR and extract a certain region of harmonics that can be used for the nonlinear process. A split

mirror—a spherical mirror cut into two pieces—was used to introduce a delay in two spatially divided components of the XUV beam and to focus them into a gas jet. Typically helium gas is used as the nonlinear medium. The generated ions are accelerated with a static electric field and collected with a TOF setup. The ion signals are detected with an MCP to form a mass spectrum, which is used to extract the nonlinear signal.

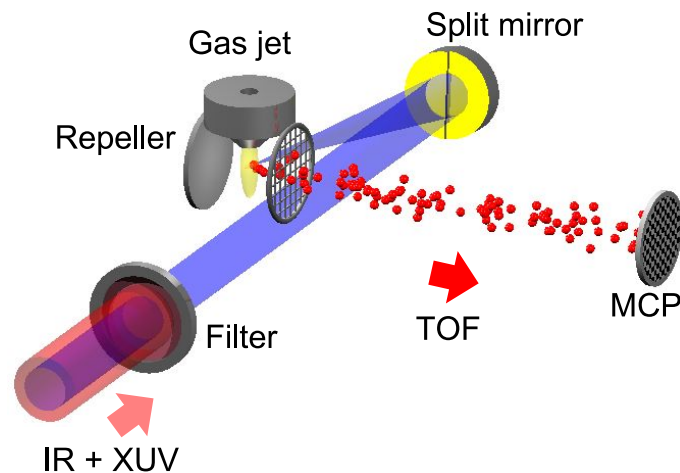


**Figure 5.1:** Scheme of volume autocorrelation. After the harmonic generation, a filter is used to block the IR and select harmonics. The harmonic beam is divided into two spatial components with a split mirror and focused into a gas jet. The generated ions are collected with a TOF setup and detected with an MCP.

First thing to consider when implementing the volume autocorrelation is the nonlinear process used for the autocorrelation and range of harmonics allowed by the process. Two-photon ionization of rare gas such as helium [119] is one of the simplest and the most straightforward processes. Helium has the highest ionization potential of all the atoms, whose value is 24.6 eV [113], and is suitable for this purpose because it allows the use of a wide range of harmonics. For an IR pulse with the central wavelength of 800 nm, any combination of harmonics between 8th order (12.4 eV) to 15th order (23.2 eV) can be used to ionize helium through two-photon ionization process. On the other hand, any harmonics from 16th order (24.8 eV) and above is capable of ionizing helium by a single photon. This single-photon ionization is a linear process and cannot be used for autocorrelation measurement.

The problem of single-photon ionization is its high cross section and resulting high ion yield, which can easily mask the ion signal from the two-photon ionization process. The cross section for single-photon ionization at the 16th order (50 nm) is  $\sim 7 \times 10^{-18} \text{ cm}^2$  [130], while the cross section for two-photon ionization around the 10th order ( $\sim 80 \text{ nm}$ ) is  $\sim 10^{-51} \text{ cm}^4 \text{ s}$  [131]. The total ion yield can be estimated from the cross section and the XUV photon flux. The XUV photon flux for each harmonic is estimated to be  $\sim 10^{28} \text{ cm}^{-2} \text{ s}^{-1}$  from the parameters used in Section 4.4. From this value, the transition probability per second [131] is obtained to be  $\sim 7 \times 10^{10} \text{ s}^{-1}$  for single-photon ionization and  $\sim 10^5 \text{ s}^{-1}$  for two-photon ionization. Therefore, the

ion yield from single-photon ionization process is expected to be  $\sim 5$  to 6 orders of magnitude higher than that from two-photon ionization. In other words, if the harmonics of 16th order and higher are not sufficiently suppressed, single-photon ionization process will be dominant and it will obscure the signal from two-photon ionization process. Thus it is crucial to suppress the photons with the energy higher than the ionization potential of helium.

Another thing to be considered is the property of the autocorrelation trace. The volume autocorrelation technique is different from the conventional Michelson-interferometer-type autocorrelation in two respects [132]. One is that the beam is split spatially into two and changing the delay between them results in a spatial redistribution of the energy in the nonlinear medium. This is in contrast to the amplitude-splitting arrangement, where the delay variation results in the change in the energy reaching the nonlinear crystal and the detector. The other is related to the first effect. Since the delay variation is reflected in a spatial distribution of the energy, the calculation must take account of the volume where the interaction occurs, which makes it more complicated than the amplitude-splitting method, where the effect of volume does not play a crucial role.

In the volume autocorrelation technique, any signal generated from a linear process will be constant over the delay because the energy within the focal volume does not change by varying the delay. On the other hand, a second-order process will be sensitive to the delay because the signal scale as the square of the intensity, whose integral is not constant even when the total energy is constant. Mashiko and his coworkers [133] calculated the spatial distribution of the energy in the focal plane analytically, and used it to calculate a second-order interferometric autocorrelation trace. The peak-to-background ratio was obtained to be  $\sim 4.5 : 1$ . Tzallas and his coworkers [117] made a numerical simulation including the volume effect by calculating also in the focal direction, and obtained a second-order interferometric autocorrelation trace with the peak-to-background ratio of  $\sim 2.75 : 1$ . Although the peak-to-background ratio is lower than that of the conventional Michelson-type autocorrelation, where the ratio is  $8 : 1$ , these results suggest that this method can be certainly used for autocorrelation measurement.

## 5.2 Experimental setup

### 5.2.1 General setup

The experimental setup used for the autocorrelation measurement is shown in Fig. 5.2. The laser parameters are the same as those described in Section 4.1.1. The 60-mm-diameter IR beam was focused with a dielectric 4-inch  $30^\circ$  off-axis parabola with the focal length  $f = 150$  mm onto a target ( $F = 2.5$ ). A 120-mm-diameter round plate made with Plexiglas was used as the target because the highest harmonic generated from Plexiglas is 14th order (21.7 eV), as shown in Fig. 4.10. In other words, no harmonic is generated with the photon energy above the ionization threshold of helium.

The reflected beam was re-collimated with a gold-coated,  $90^\circ$  off-axis parabola with the focal length  $f = 75$  mm (effective focal length  $f_{\text{eff}} = 150$  mm), which is the same as the one shown in Fig. 4.17. The  $F$ -number of the parabola was  $F = 6$ , which is approximately half of the  $F$ -



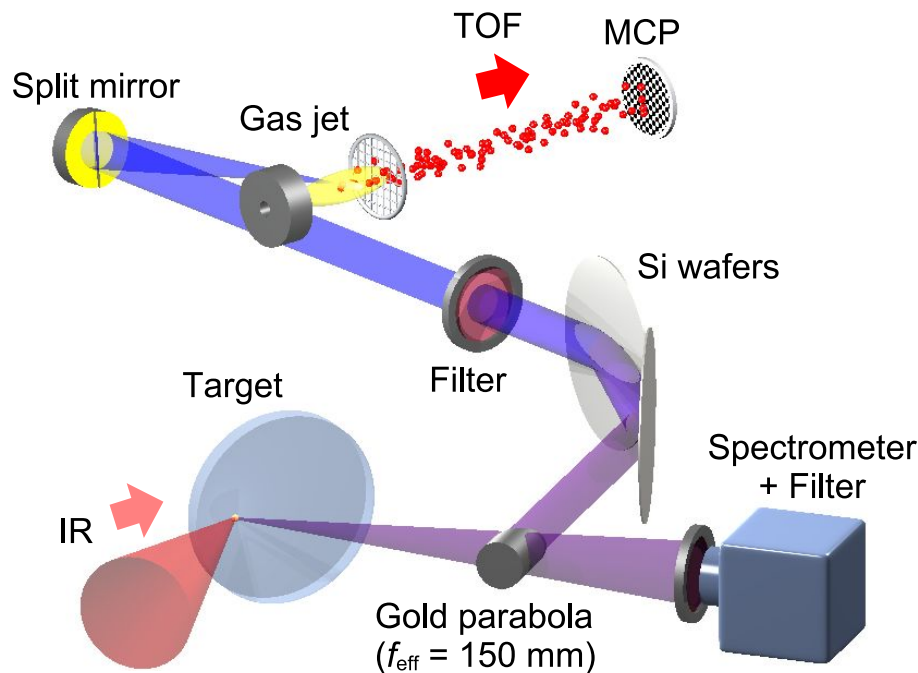


**Figure 5.2:** Experimental setup for volume autocorrelation. The incoming IR beam is focused with a parabola ( $F = 2.5$ ) onto a Plexiglas target. The reflected beam is re-collimated with a gold parabola ( $F = 6$ ) and reflected by two silicon wafers to suppress the remaining IR. The spectral region is selected by a filter afterward. The beam is focused with a split mirror ( $R = 300$  mm) into a helium gas jet. The generated ions are collected with a TOF setup and detected by an MCP. The re-collimating parabola could be flipped out of the beam to observe the spectrum of the reflected light with a spectrometer.

number of the incident IR beam. This configuration was chosen to avoid a technical problem. To collect the whole beam and still keep the beam size small so that the beam can be easily handled, the best way is to place the parabola as close to the target as possible. However, the energy of the IR beam is so high that the reflected IR beam damages the coating of the parabola, if it is placed too close to the target. Therefore it was placed rather far from the target. On the other hand, the usable size of the XUV beam is limited by the sizes of the split mirror and the filters, which are approximately 1 inch. Thus the diameter of the parabola was also chosen to be 1 inch. The collected XUV energy is estimated to be  $\sim 38\%$  of the generated XUV, as discussed in Section 4.4.

The parabola was mounted on a flipper mount so that the spectra of the reflected beam could be observed with a 1-m grazing incidence spectrometer (Model 248/310, McPherson) by moving the parabola out from the beam. The beam collected with the parabola was reflected by two silicon wafers at  $75^\circ$  incidence angle to suppress the reflected IR beam. These silicon wafers were replaced with a single glass plate at  $60^\circ$  incidence angle in some of the experiments. After the silicon wafers, a metallic filter was inserted in the beam to select a certain region of the harmonic spectra and suppress the remaining IR. Typically, a 150-nm-thick indium filter with

1-inch open aperture was used. A 150-nm-thick tin filter was also tried, but it was not used in the autocorrelation measurements because the quality of the filter was not as good as indium filters with the same size. With the indium filter, harmonics from 8th order to 10th order are transmitted efficiently ( $\sim 30\%$ ), and the other harmonics from 11th to 14th are transmitted with the efficiency of  $\sim 2\%$  or lower. The transmitted harmonics are focused with a gold-coated spherical split mirror ( $R = 300$  mm) into a gas jet generated from a pulsed valve (Model LPV, Lasertechnics). The generated ions are accelerated with a static electric field into a TOF setup and time-resolved mass spectra are measured with an MCP and accumulated with an oscilloscope (TDS7104, Tektronix).

### 5.2.2 Focus property in the interaction volume

Since the focus property in the interaction region is important for the method of volume autocorrelation, the focus of the IR beam in the gas jet was imaged and observed with a beam profiler (WinCamD, DataRay). This imaging system also served the purpose of the alignment. To have enough reflectivity off from the silicon wafers for the weak alignment IR beam, a half-wave plate was moved into the beam to change the polarization from  $p$  to  $s$ . The filter was mounted on a flipper so that it could be moved out of the beam. Typical images of the spot are shown on Fig. 5.3(a, b).

Since the diameter of the beam was as large as  $\sim 25$  mm, the gas jet had to be placed 20 mm above the incoming beam, which resulted in a rather large angle of  $\sim 8^\circ$  between the incoming beam and the reflected beam. This means that the aberration from the split mirror is not negligible and the autocorrelation traces obtained by former work [117, 133] are not applicable. Therefore, I made a numerical simulation similar to the one shown in Ref. [117] by taking the effect of aberration into account (see Appendix B for detail). Some of the images obtained for IR incident beam with the same parameters as the experiment are shown in Fig. 5.3(c, d), together with corresponding images observed experimentally. In Fig. 5.3, two different foci produced from two halves of the split mirror are shown separately. Although the simulation results do not reproduce all the features observed in the experimental spots, the overall profiles resemble the experimentally observed IR spots. The discrepancy is probably due to slight misalignments and non-perfect wavefront of the experimental beam. Fringe structures are coming from aberrations similar to a coma [134].

With this code including aberration, volume autocorrelation trace was calculated by using three harmonics from 8th to 10th order, which corresponds to the main harmonics transmitted through the indium filter. Other harmonics are ignored because they are at least one order of magnitude weaker than those three harmonics. The amplitude was assumed to be constant over time, i.e., the simulation included no information about the envelope of the pulse train. The focal volume to be considered was found by making many runs with low resolution and studying which part of the volume has the highest value for the square of the intensity, which should be proportional to the helium ion yield. The focal volume used for the full scan was  $15 \mu\text{m} \times 50 \mu\text{m} \times 150 \mu\text{m}$ . Figure 5.4 shows the autocorrelation trace obtained from the simulation. A peak with sub-cycle structure is observed for each cycle, in contrast to the gas HHG [117], where two peaks are observed for each cycle because the separation between the harmonics was  $2\omega_0$ .

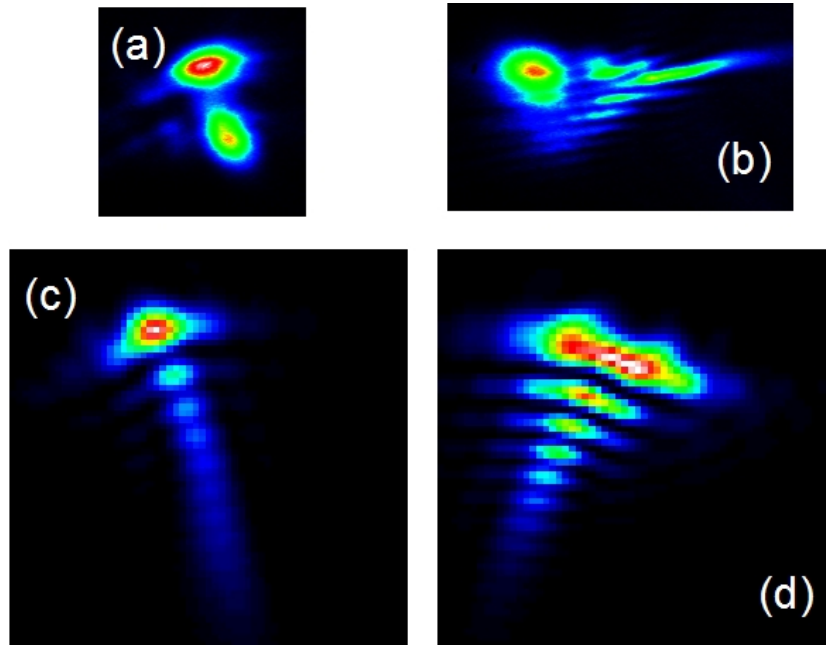


**Figure 5.3:** Images of the (a, b) measured and (c, d) simulated profiles at the focus. The images show the focus observed with half of the beam coming from (a, c) left half and (b, d) right half of the split mirror. The experimental and simulation results resemble each other. The fringe structures are from aberrations similar to a coma.

Since no envelope was included in the simulation, the background level was obtained separately by simulating only half of the beam so that no interference occurs, and then multiplying the obtained value by 2, which is equivalent to setting the delay  $\Delta\tau \rightarrow \infty$ . The peak-to-background ratio is found to be approximately 1.5 : 1. This value is lower compared to the values obtained by other work [117, 133] because of the aberration. Nevertheless, this simulation shows that the fringe should be still observable with the current setup.

### 5.2.3 Time-of-flight setup

The time-of-flight setup was characterized by using argon gas instead of helium gas because it can be easily ionized and detected with the TOF setup. Typically, 5 kV to 6 kV of high voltage was applied over the distance of  $\sim 10$  cm to accelerate the ions. The distance between the end of the acceleration region and the MCP was approximately  $\sim 50$  cm. Figure 5.5 shows a typical ion spectrum measured by focusing the XUV beam that passed through a 150-nm-thick indium filter into argon gas jet. A sharp, strong peak around  $4 \mu\text{s}$  is the signal coming from  $\text{Ar}^+$ . A small peak on the left around  $1 \mu\text{s}$  is a signal coming from the scattered light and corresponds to the arrival time of the XUV pulse. Those two peaks are used for calibrating the axis of the mass spectra and identifying other ion signals in other ion spectra. When measuring mass spectra, several parameters, especially the amount of the gas, were controlled carefully so that the ion

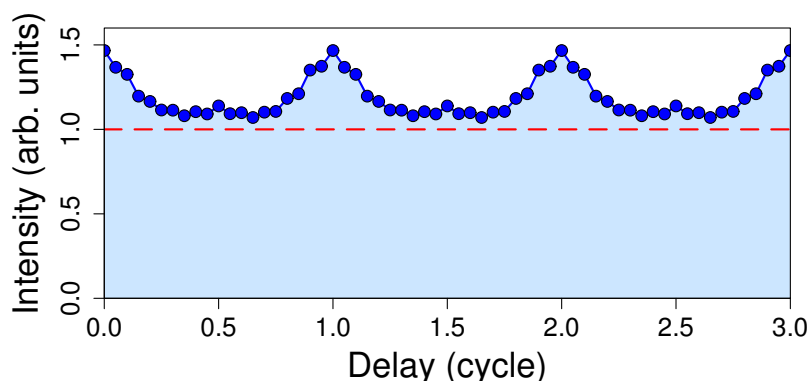


**Figure 5.4:** Autocorrelation trace obtained from simulation. A periodic structure of sub-cycle pulses constituting a train is clearly observable. The horizontal dashed line shows the background level. The peak-to-background ratio is approximately 1.5 : 1.

peaks were strong but also narrow at the same time. When the amount of the gas is too much, the peaks start to get broader because of the space-charge effect, i.e., the ions are expelled in all the directions and arrives at the MCP at different moments, which results in the broadening of the peaks. When the space-charge effect is observed, it means that there is too much gas, which can be detrimental to the measurement because dense electrons and ions can cause collisional ionization, which also obscures the two-photon ionization process.

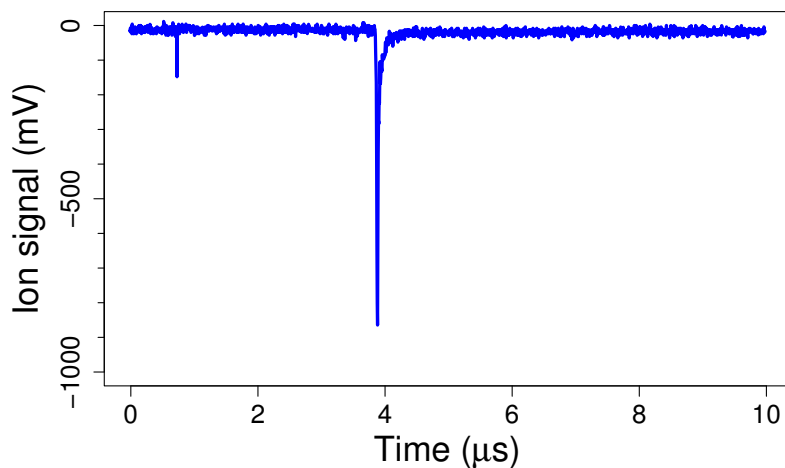


**Figure 5.5:** Raw ion mass spectrum measured with argon gas. A sharp, strong peak in the middle is the signal from  $\text{Ar}^+$ . A small peak on the left is a signal coming from the scattered light, which is used to determine the arrival time of the XUV pulse.

## 5.3 Two-photon ionization of helium

The first thing to confirm before starting to measure the autocorrelation is that helium ions are generated from two-photon ionization process. In fact, it is possible that the ions are generated by other processes, for example, single-photon ionization from the remaining high-energy XUV photons that were not properly suppressed. If the single-photon ionization process is dominant, no modulation will be observed in the autocorrelation trace [117].

Ion mass spectra are measured with the setup shown in Fig. 5.2. A 150-nm-thick indium filter was used to select mainly from 8th to 10th harmonics with the throughput of  $\sim 20$  to 30%, while transmitting higher-order harmonics with low efficiency ( $\sim 2\%$ ). Since Plexiglas is used as the target, no harmonic above 14th order should be generated. Those harmonics are focused into a helium gas jet. Measured ion mass spectrum is shown on Fig. 5.6.

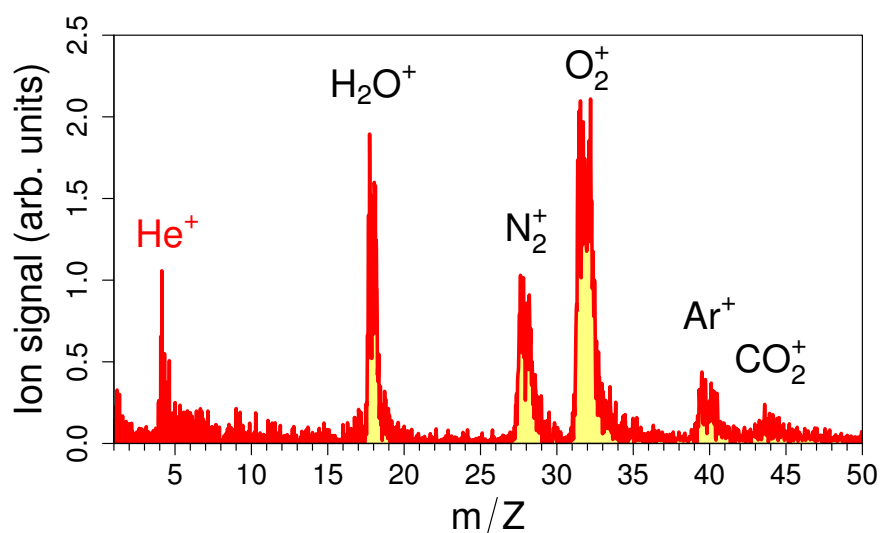


**Figure 5.6:** Calibrated ion mass spectrum measured with helium gas. The horizontal axis is the mass  $m$  divided by the charge state number  $Z$ . Besides a helium peak, signals from remaining argon gas and other gases contained in the air are observed. All the gases other than helium should be ionized from a single photon.

The horizontal axis is calibrated from the positions of the photon peak and the argon peak in separately measured spectra as in Fig. 5.5. Besides the signals from helium and remaining argon, signals from the gas contained in air such as water, nitrogen, oxygen, and sometimes carbon dioxide are observed. All the gases other than helium has ionization potential lower than 16 eV, as shown in Table 5.1. Since harmonics from 8th to 10th order should be the main constituents of the XUV beam, the water, oxygen, and carbon dioxide can be easily ionized with a single photon of 9th (13.9 eV) or 10th (15.5 eV) harmonic. On the other hand the nitrogen and argon should be ionized with relatively weak (but still strong enough) harmonics between 11th to 14th order through single-photon ionization process. A double-peak structure observed on the

$O_2^+$  peak was coming from non-perfect overlapping of the two foci from the two halves of the split mirror. This is not critical for measurements that does not require changing the delay, but better overlapping is certainly necessary for autocorrelation measurements.

**Table 5.1:** Ionization potential of the observed gases [113].

Gas	Ionization potential (eV)
He	24.6
H <sub>2</sub> O	12.6
N <sub>2</sub>	15.6
O <sub>2</sub>	12.1
Ar	15.8
CO <sub>2</sub>	13.8

Although the helium signal is clearly observed in Fig. 5.6, it is not a proof that the helium ions are generated from two-photon ionization process. To find the nonlinearity of the ionization process, it is necessary to observe how the ion signal scales as the XUV intensity changes. If the ion signal scales linearly to the XUV intensity, it means that the process is linear and indicates that the single-photon ionization process is dominant. On the other hand, if the signal scales quadratically to the XUV intensity, it means that a 2nd-order process—two-photon ionization—is dominant. Therefore, it is necessary to make an XUV energy scan to find the nonlinearity of the ionization process.

One issue has to be mentioned before the scan, which is a technical problem of the target degradation. After a few hundred laser shots on one target, a rapid degradation of the ion signal was observed. Figure 5.7 shows the ion signal measured over  $\sim 100$  spectra without changing any experimental parameters. For each spectra, 20 laser shots were accumulated. The signal stayed at the same level only for the first 10 spectra, and then started to degrade rapidly. The degradation of the signal slows down after  $\sim 40$  spectra, and the signal eventually converge into certain values.

This degradation of the signal is most probably due to the degradation of the target surface. Actually there seemed to be two types of surface degradation. One is a relatively long-term degradation caused by debris. In fact, a large amount of debris was observed while shooting onto the Plexiglas target, even more than that observed from glass targets. The debris floats in the vacuum chamber and eventually come back onto the target surface and impairs the surface quality. This type of surface degradation takes place when the target stays too long in the chamber. For example, when a half-used target stayed in the chamber over night, the XUV signal observed on the next day was much lower than that from the day before, even when nothing has changed in the laser condition. This type of degradation was avoided by placing a thin protective plate right in front of ( $\sim 1$  mm away from) the target. The other type of degradation was rather short term, which caused the signal degradation observed in Fig. 5.7. It was cracking of the surface from each laser shot. Although the observed damage spot size was  $\sim 1$  mm and 1.5 mm spacing in each direction seemed to be enough, actually it was not the case. The signal started to de-

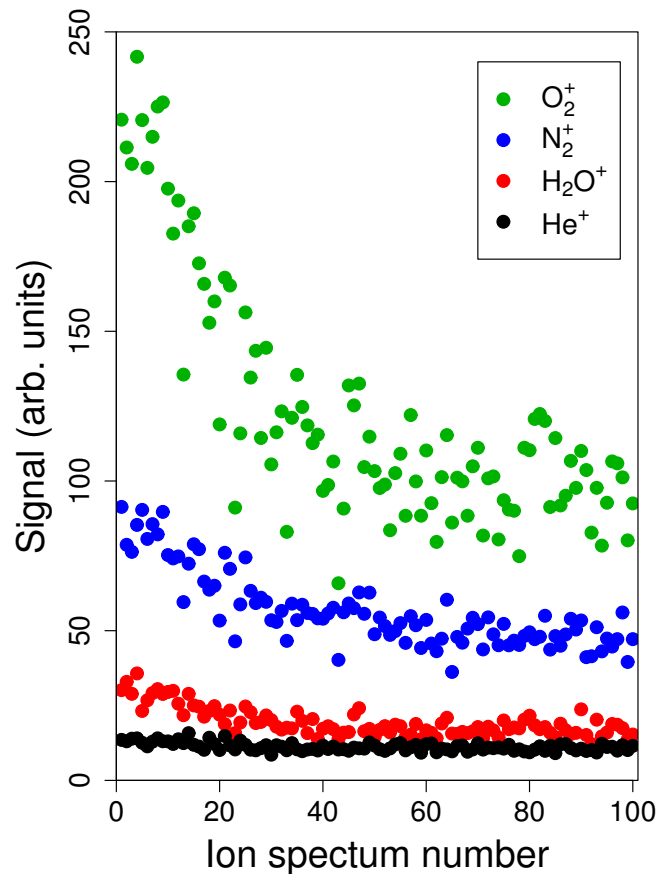


**Figure 5.7:** Degradation of the ion signals. Each point is extracted from an ion spectrum measured with an accumulation of 20 laser shots. The signals degrade rapidly within  $\sim 40$  spectra and eventually converge into certain values.

grade after the target has made one revolution and the focal spot moved to the next circle on the target. This suggests that the actual damage was larger in radial direction (although it was not visible) and the spot in the new circle was actually hitting the damaged surface. This degradation was avoided by increasing the interval between the damage circles to 4 mm. On the other hand, this reduced the number of shots allowed on each target to  $\sim 2000$ . After those changes, no significant degradation of the signal was observed over one target.

Having solved the technical problem of target degradation, I return to the determination of the nonlinearity. To find the nonlinearity of the generation process of the ions observed in Fig. 5.6, the ion signals were measured by changing the energy of the incident IR pulse with ND filters. Each mass spectrum was obtained by accumulating 50 laser shots. For this measurement, the split mirror was fixed at the zero-delay position, i.e., the split mirror was used as an ordinary spherical mirror. The nonlinearity of the ionization process can be found by plotting the ion signal as a function of the XUV intensity in a log-log scale, where the slope of the plot should

equal the nonlinearity of the process. Since it was not possible to measure the XUV intensity directly with the setup, I plotted the ion signals as a function of  $O_2^+$  signal instead. Rationale behind this is as follows. Theoretically, oxygen should be ionized with any harmonic photons of 8th order (12.4 eV) or higher through the single-photon ionization process, i.e.,  $O_2^+$  signal should scale linearly to the XUV intensity. In other words,  $O_2^+$  signal should be proportional to the XUV intensity and plotting against  $O_2^+$  signal should be equivalent to plotting against the XUV intensity. The resulting plot is shown in Fig. 5.8(a).

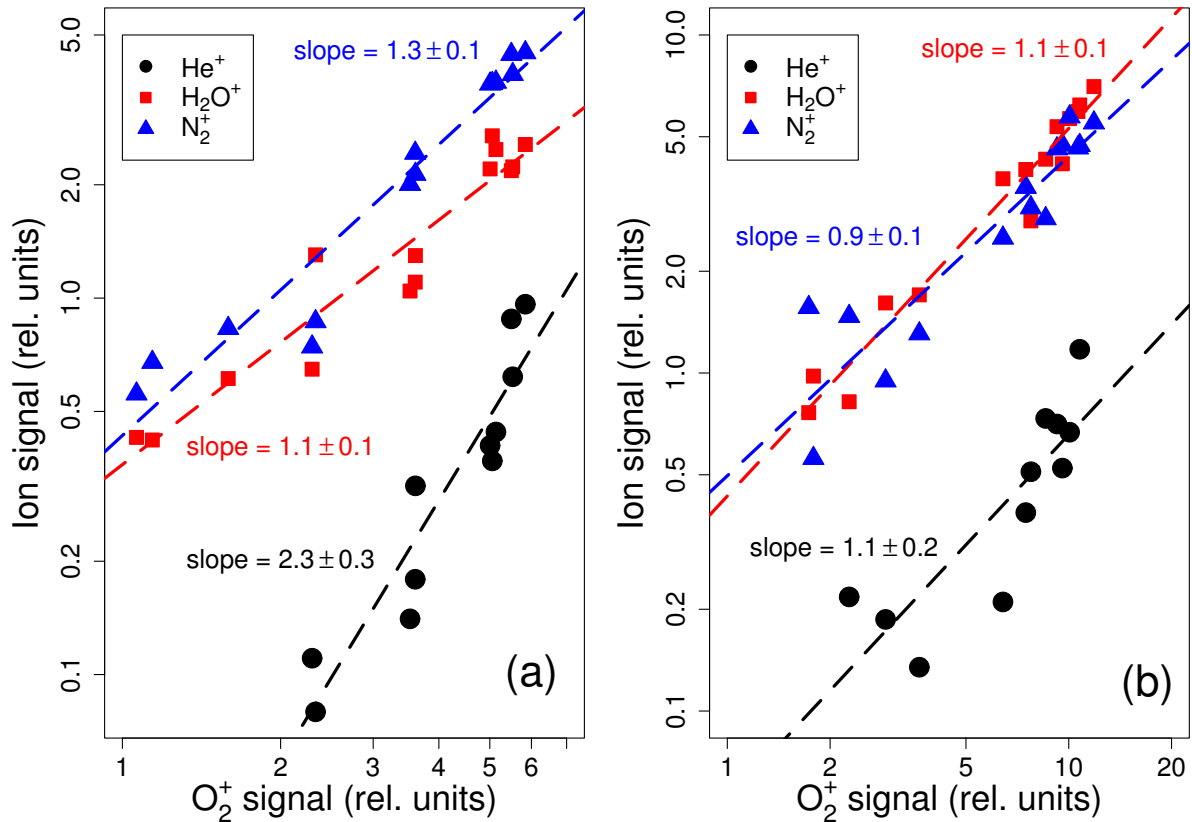


**Figure 5.8:** Intensity dependences of ion signals. The ion signals are plotted against  $O_2^+$  signal, which is equivalent to plotting against the XUV intensity. (a) Results obtained with a Plexiglas target. The signals from water and nitrogen show the slope of one, while the helium ion signal shows the slope of two. This means that water and nitrogen are ionized with a single photon, while helium is ionized through two-photon ionization process. (b) Results obtained from a glass target. All the ion signals exhibit the slope of one, which indicates that all the ions including  $He^+$  are generated from single-photon ionization process. The difference from the Plexiglas target is the presence of harmonics higher than 15th order, which are capable of ionizing helium with a single photon.

The slopes of the ion signals are determined by linear fitting. For the ion signals from water and nitrogen, the observed slopes are one. This indicates that water and nitrogen are ionized



through the single-photon ionization process. On the other hand, the ion signal from helium shows the slope of two. This means that the helium ion yield scales quadratically to the XUV intensity and the helium ions are generated through two-photon ionization process. These scalings are exactly the expected behavior, and it is confirmed that the ionization process of helium is second order.

For comparison, same kind of measurements and analysis were made by changing the target to fused silica. The result is shown in Fig. 5.8(b). In this case, the observed slopes are one for all the ions including helium, which means that all the ions are generated from the single-photon ionization process. This is explained by the presence of harmonics higher than 15th order for the glass target, as shown in Fig. 4.10. Although a 150-nm-thick indium filter was used, the suppression of those higher-order harmonics was only 2 to 3 orders of magnitude and was clearly not enough, and thus the single-photon ionization process became dominant.

## 5.4 Coarse autocorrelation measurement

Provided that the generation process of the helium ions is second order, autocorrelation traces can be measured by observing the evolution of the helium ion signal as a function of the delay between two parts of the beam [119]. The measurement of Ref. [119] characterized the duration of only one harmonic and is fundamentally different from our experiment, where more than one harmonic are involved and interference among them results in a pulse train structure [17]. On the other hand, if the delay scan is made with a coarse step so that the interference is not resolved, this under-sampling will cause aliasing and only the overall tendency of the autocorrelation trace will be observed. In other words, the measured coarse autocorrelation will reflect the shape of the envelope of the XUV pulse train [117], which corresponds to intensity autocorrelation in conventional terminology.

Before starting the measurement, the silicon wafers to suppress IR was replaced with a thick glass plate because we found that the reflection from thin silicon wafers distort the wave front. After two reflections from the silicon wafers, the observed image of the IR focal spot in the gas jet was far from the spot expected from the ray tracing, which implies that there was a severe distortion of the wave front. For the previous measurement of the two-photon ionization of helium, this focus was good enough because the focal pattern did not change during the energy scan, i.e., the shape of the focal spot did not affect the measurement. On the other hand, the autocorrelation measurement relies on the energy and intensity redistribution within the focal volume [117] and thus distorted focal spot might lead to unexpected results. Therefore, it was crucial to improve the focus. A thick glass plate was chosen as the replacement because its reflectivity of 800 nm radiation at  $60^\circ$  is  $\sim 2.5 \times 10^{-3}$ , which should be enough amount of suppression, and less wave front distortion was expected from the thick slab. After replacing the silicon wafers to a thick glass plate, the focus became much smaller and similar to the results obtained from the ray-tracing calculation, as shown in Fig. 5.3. The reflectivity of 8th to 10th harmonics from the glass plate at  $60^\circ$  is  $\sim 5\%$ , which is a factor of  $\sim 10$  smaller than two reflections from silicon wafers at  $75^\circ$ . On the other hand, the focus spot became much smaller and the loss of energy was compensated by a smaller spot size, i.e., the expected XUV intensity at the focus was at least at

the same level, if not higher.

To measure a coarse autocorrelation trace, the evolution of the helium ion signal was observed by changing the delay between the two components from the split mirror. A half of the split mirror was scanned with a step size of  $0.5\ \mu\text{m}$ , which corresponds to  $1\ \mu\text{m}$  of light path difference and  $3.3\ \text{fs}$  of delay. This is larger than one cycle of the fundamental laser pulse and hence it is not possible to resolve the fine pulse structure within the XUV pulse train. For each delay, 20 laser shots were accumulated to measure one mass spectrum. The  $\text{He}^+$  signals are obtained from the measured ion spectra and plotted against the delay. The resulting autocorrelation trace is shown in Fig. 5.9(a).

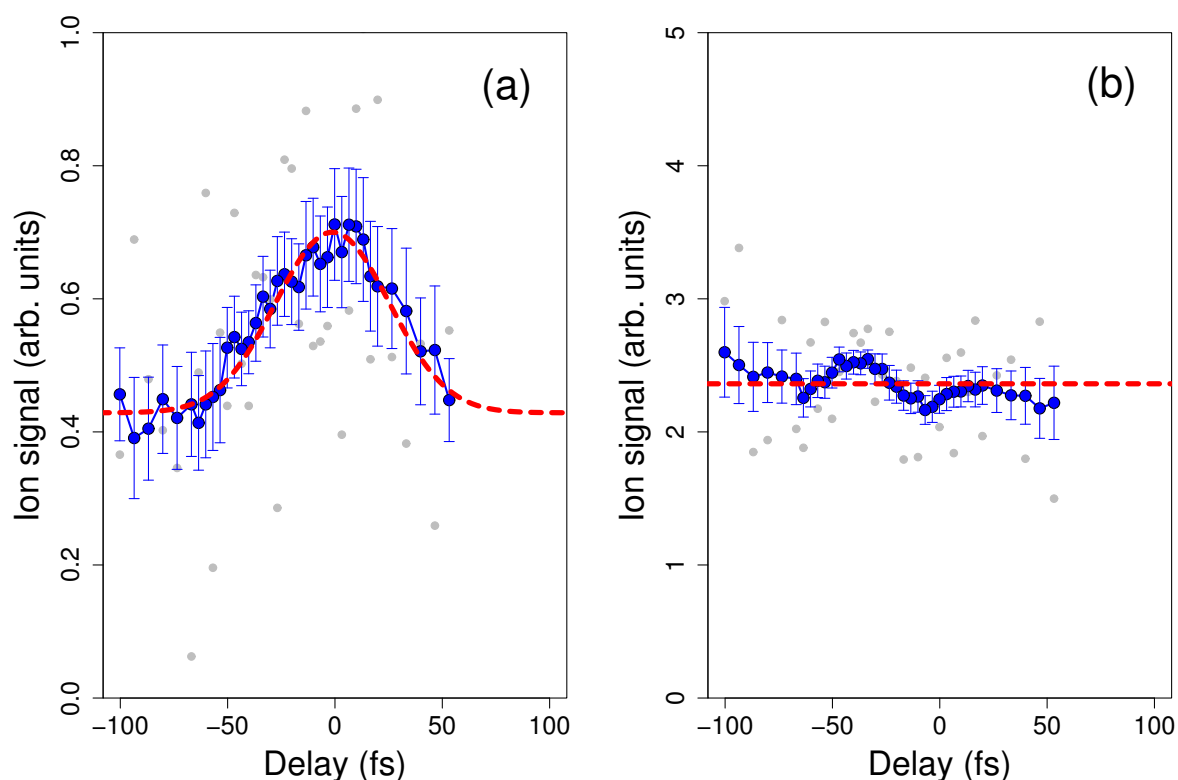


**Figure 5.9:** Measured coarse autocorrelation. (a) Autocorrelation trace measured using  $\text{He}^+$  signal with a step of  $3.3\ \text{fs}$ . The raw data points are shown as gray dots, which have a rather large fluctuations but still show a tendency of high signals in the middle and low signals at the edges. Blue dots are the running average of 4 points on each sides, which reduces noise and makes the structure clearer. The red dashed curve shows a Gaussian fit to the raw data. The duration of the envelope of the XUV pulse train obtained from the fit is  $\sim 44\ \text{fs}$ . (b) The same kind of trace measured with  $\text{H}_2\text{O}^+$  signal. The trace shows no significant peak compared to the background level, which is expected because the ionization process is linear.

The raw data is shown as gray dots in Fig. 5.9. Although the fluctuation is large, a tendency of higher signals around the zero delay and lower signals at the edges can be seen. This feature

becomes clearer when the running average (smoothing) of the data is taken. The blue dots show the running average of 4 points on both sides from each points, i.e., running average of 9 points overall. The error bars show the standard error of the running average. If the fluctuation is from pure noise, the averaging should result in a flat trace. Instead, a clear peak structure is seen. To deduce some quantitative information, I fitted a Gaussian onto the ‘raw’ data. I chose to fit on the raw data instead of the running average because the fitting onto running average tends to overestimate the width of the trace, which I will explain later. Despite the large fluctuation of the raw data, the fitted curve nicely lies on the points from the running average. From the fitted parameters, the peak-to-background ratio was obtained to be  $(1.7 \pm 0.3) : 1$ , which matches the ratio of  $1.5 : 1$  obtained from the calculation shown in Section 5.2.2. The width of the autocorrelation is obtained as  $(62 \pm 28)$  fs, which means that the duration of the envelope of the XUV pulse train is  $(44 \pm 20)$  fs, because the width of the autocorrelation trace is a factor of  $\sqrt{2}$  larger than that of the measured pulse, when a Gaussian profile is assumed. The error is rather large because of the large fluctuation of the raw data. A fit to the running average of 3 points gives the pulse duration of  $(44 \pm 9)$  fs instead, where the error is much smaller, but care must be taken here. The more points you take for running average, the longer the fitted pulse becomes, as summarized in Table 5.2. The fitted pulse duration for running average of 9 points is clearly longer than that for the raw data. On the other hand, this effect is smaller for the running average of less number of points. Thus I conclude that the duration of the XUV pulse train is  $\sim 44$  fs.

**Table 5.2:** Fitted pulse duration for different number of running average.

Averaged points	Duration (fs)
1	$44 \pm 20$
3	$44 \pm 9$
5	$46 \pm 6$
7	$49 \pm 4$
9	$53 \pm 4$

The duration of  $\sim 44$  fs is almost the same as the duration of the incident IR pulse produced from ATLAS, which was  $\sim 45$  fs. This is somewhat counter-intuitive because the harmonic generation process for gas HHG is nonlinear and the duration of the XUV pulse train expected in analogy is shorter than that of the incident IR pulse. On the other hand, it was observed that the generated XUV intensity of the CWE process is actually nearly linear to the incident IR intensity [135]. This observation is consistent with the observed duration of the XUV pulse train and supports our result.

For comparison, the evolution of the  $\text{H}_2\text{O}^+$  signal was extracted from the same set of measured mass spectra and plotted in Fig. 5.9(b). The signal is basically flat over all the delay range. This result is expected because  $\text{H}_2\text{O}^+$  signal is generated from a single-photon ionization process. Since a linear process depends only on the energy within the interaction volume, the different intensity distribution from the different delay does not affect the total ion yield [132]. Although a

small modulation can be seen on the trace, this modulation has no physical significance because it is small compared to the signal level, i.e., the peak-to-background ratio is low. This modulation simply shows that the average XUV intensity fluctuated a little, but was not so significant to affect the measurement.

## 5.5 Fine autocorrelation measurement

To observe the expected fine structure of the XUV pulses within the autocorrelation trace [17, 117], the relative delay introduced by the split mirror must be set small enough so that the fringe structure can be resolved.

The ion spectra were measured by moving a half of the split mirror in a step of 20 nm over a distance of  $\sim 1.5 \mu\text{m}$ . This distance corresponds to the light path over  $\sim 3 \mu\text{m}$  with 40 nm step and the relative delay over  $\sim 10$  fs with  $\sim 0.13$  fs step. This step size means that there are 20 points per cycle and should be small enough to resolve the fine structure. At each position, a mass spectrum is obtained by accumulating over 20 laser shots. Figure 5.10 shows all the spectra measured in one run. From these raw ion spectra, the  $\text{He}^+$  signals are extracted and plotted as a function of the relative delay. The resulting trace is shown in Fig. 5.11(a).

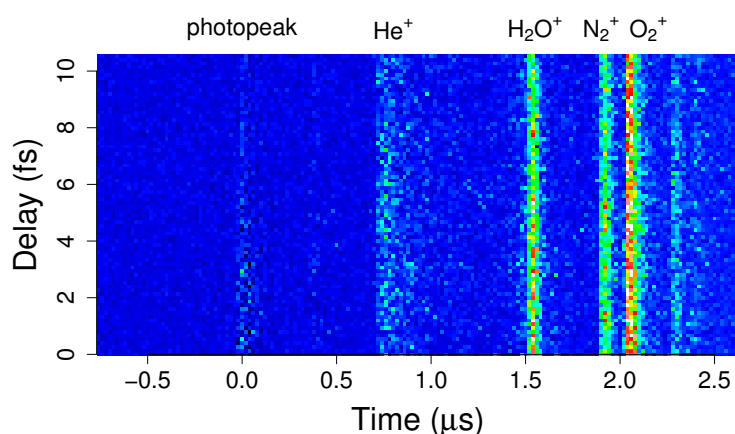


**Figure 5.10:** Series of raw ion spectra measured by changing the relative delay between the two beams coming from the split mirror.

The raw data points are shown as gray dots. The fluctuation is rather large and it is difficult to see the tendency. To make the tendency clear, I took the running average of 9 points (4 points from each side), i.e., same as the analysis made in Fig. 5.9. The resulting trace is shown as the blue circles. The error bars show the standard error of the running average. Now it is clear that there is a structure with a certain period. To analyze this structure quantitatively, I made a fit with five successive Gaussian profiles with a background. This five Gaussian structure was fitted directly to the autocorrelation data, i.e., obtained width will be the width of the fringe structure in the autocorrelation trace and not the width of the pulse within the pulse train. The assumptions were (i) the interval between the peaks are fixed with the laser period 2.67 fs, and (ii) all the

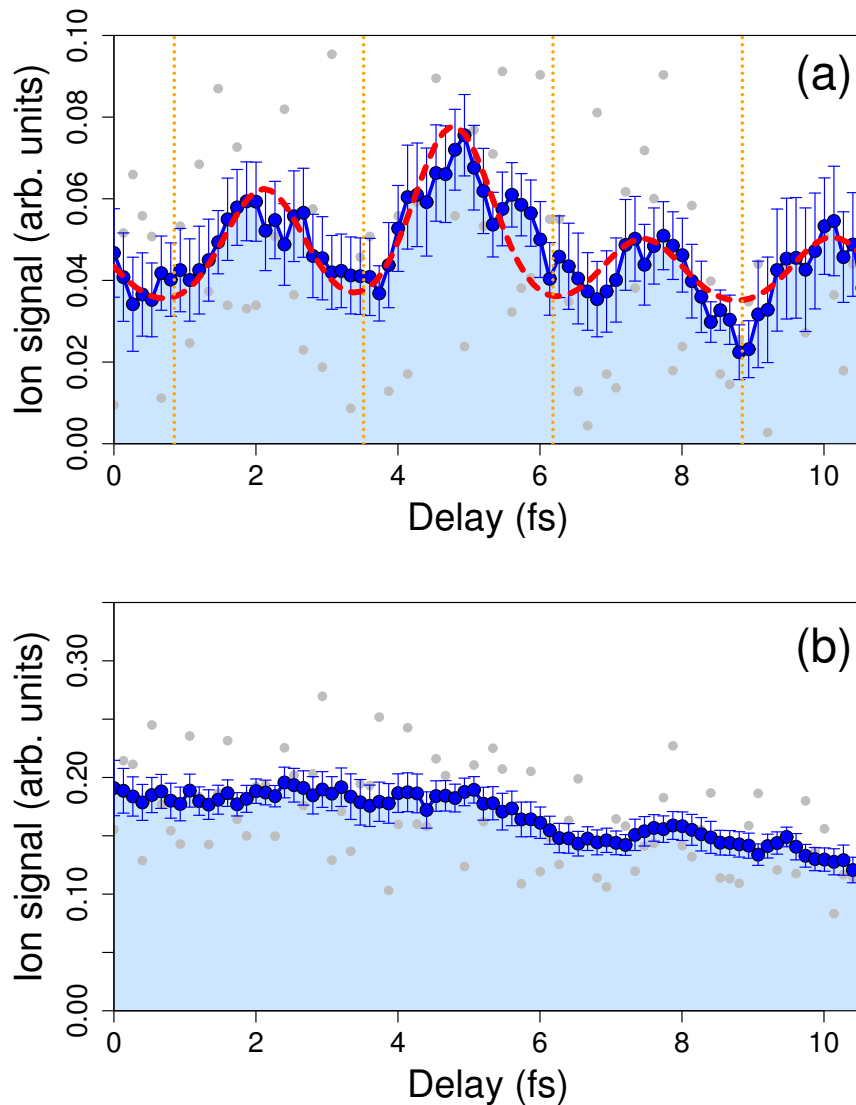


**Figure 5.11:** Measured fine autocorrelation. (a) Autocorrelation trace measured using  $\text{He}^+$  gas with a step of 0.13 fs. The raw data are shown as gray dots. Blue dots show the running average of the raw data, taking 4 points from each side. Several peaks are observed with some periodicity. The red dashed curve is a fit onto the raw data, assuming five Gaussian peaks spaced with a fixed interval of 2.67 fs (one laser period). The vertical orange dotted lines are placed with the same period to divide the trace into cycles and make the structure clear. (b) Same kind of trace measured using  $\text{H}_2\text{O}^+$ . No significant modulation is observed. The lower signal at the end is probably due to a slight degradation in the XUV signal.

Gaussian profiles have the same width. The other parameters such as the amplitude of each peak and the background level were free. The fit was made onto the raw data again. The resulting curve is shown as a red dashed line in Fig. 5.11(a). Although the fit was made onto the raw data, the curve lies nicely onto the blue circles of the running average. This also indicates that there is a clear periodic structure in the measured trace, which appears with the period of the fundamental laser field.

The width of the Gaussian was obtained from the fit as  $(1300 \pm 500)$  as. From this value, the duration of the pulses within the XUV train is obtained to be  $(900 \pm 400)$  as, because an autocorrelation of a Gaussian pulse train will be a train of Gaussian broader by a factor of  $\sqrt{2}$ . Note that this is the average duration of the pulses within the train, because the fit was made by assuming all the Gaussian to have the same width. In any case, the duration of the single pulse within a train is  $\sim 900$  as, i.e., the harmonics generated from solid surfaces have attosecond pulse structure.

A same kind of measurement was made with  $\text{H}_2\text{O}^+$  signal. The result is shown in Fig. 5.11(b). No significant modulation was observed compared to the background level, which is also expected from the same reason as in the case of coarse autocorrelation. The decrease of the signal is seen at the end of the scan, which probably means that the XUV signal has decreased during the scan owing to the degradation of the target surface. A decrease of the signal is also seen in  $\text{He}^+$  signal as a lower background level in Fig. 5.11(a). Nevertheless, this decrease did not impair the measurement significantly.

The validity of this measurement was estimated by calculating the transform limit of the harmonic spectrum. The spectrum was assumed to have harmonics from 8th to 14th order. Figure 5.12(a) shows the assumed harmonic spectrum in the gas jet. The relative intensity ratio between the harmonics was obtained from the measured spectra and the theoretical values of the transmission of the 150-nm-thick indium filter and the reflection of the gold-coated split mirror. Each harmonic was assumed to be a delta function to make the calculation simple. This assumption results in a train with a flat envelope, but this is not a problem because the necessary information is only the duration of the individual pulse and not the envelope of the train. The transform limit of this spectrum was obtained by Fourier transforming it by assuming a flat phase. The resulting pulse train is shown in Fig. 5.12(b). The obtained duration of one pulse within the train is  $\sim 500$  as.

The experimentally obtained pulse duration of  $\sim 900$  as is larger than the transform-limited value of  $\sim 500$  as. This is explained by the chirp introduced from the CWE process [34, 136]. Since the harmonic with higher frequency is generated deeper in the plasma density profile, where the local density is higher, it needs to travel longer in the plasma density than lower frequency component, i.e., the generated pulse is chirped (atto chirp). Here I will treat this problem by assuming a simple model with a linear density gradient  $n(x) = n_{\text{max}}x/L$ , as shown in Fig. 5.13. This assumption is valid when the interaction time is sub-picosecond, where the plasma does not have enough time to expand into an exponential profile.

In this case, the  $q$ -th harmonic  $\omega_q \equiv q\omega_0$  is generated at the position  $x_q = Ln_q/n_{\text{max}}$ , where the density is  $n_q = \varepsilon_0 m_e \omega_q^2 / e^2$ . If we assume that the electron bunch travels with the velocity close to the light speed, which should be a valid assumption for our relativistic laser intensity, the chirp can be directly obtained from the phase difference between the harmonics. To consider the phase

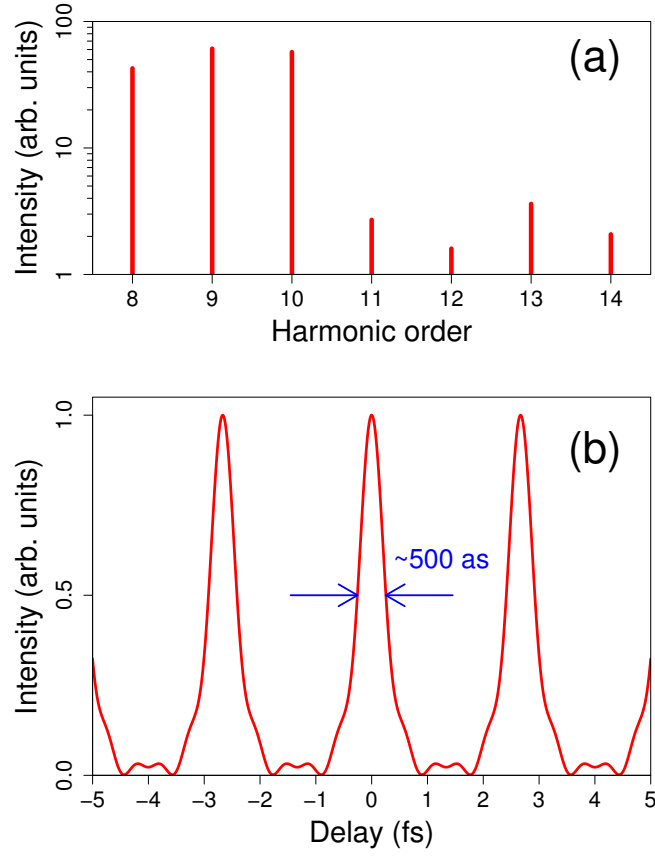


**Figure 5.12:** Transform limited attosecond pulse train. (a) Assumed spectrum in the gas jet. The ratio between harmonics are obtained from the measure spectra by taking account of the transmission of the indium filter and the reflection from the gold split mirror. (b) Train of attosecond pulses obtained by Fourier transforming the spectrum shown in (a), assuming a flat phase. The duration of one pulse in the train is  $\sim 500$  as.

accumulated by each frequency, not only the distance it travels, but also the refractive index of the plasma must be taken into account. The refractive index within the plasma is  $\sqrt{1 - \omega_p^2/\omega^2}$ , where  $\omega$  is the frequency of the traveling wave and  $\omega_p$  is the plasma frequency, which depends on the position as  $\omega_p^2 = n(x)e^2/\varepsilon_0 m_e$ . Thus, the phase  $\phi_q$  accumulated by  $q$ -th harmonic is obtained as

$$\phi_q = \omega_q \int_0^{x_q} \frac{dx}{v_{\text{eff}}} + \omega_q \int_0^{x_q} \frac{dx}{v_{\text{eff}}/\sqrt{1 - \omega_p^2(x)/\omega_q^2}}, \quad (5.1)$$

where  $v_{\text{eff}}$  is the effective velocity in the target-normal direction and is order of the light speed. The first term comes from the electron bunch traveling into the plasma density profile, while the second term comes from the generated harmonics traveling the same distance to come out. If we

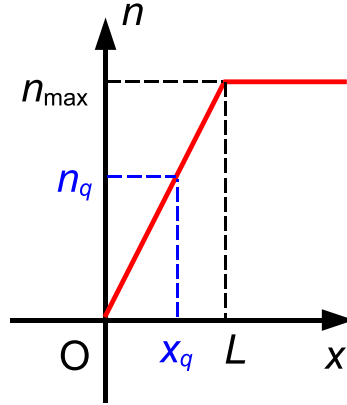


**Figure 5.13:** Assumed density ramp. The density ramp can be expressed as  $n(x) = n_{\max}x/L$ . The  $q$ -th harmonic  $\omega_q = q\omega_0$  will be reflected at  $x_q$ , where the density is  $n_q \propto \omega_q^2$ .

assume that  $v_{\text{eff}} = c/\sqrt{2}$  for  $45^\circ$  incidence angle, this phase can be readily calculated as

$$\begin{aligned}
 \phi_q &= \int_0^{x_q} \sqrt{2}k_q dx + \int_0^{x_q} \sqrt{2}k_q \sqrt{1 - \frac{\omega_p^2(x)}{\omega_q^2}} dx \quad \left(k_q = \frac{\omega_q}{c}\right) \\
 &= \sqrt{2}k_q \int_0^{x_q} \left(1 + \sqrt{1 - \frac{n(x)}{n_q}}\right) dx \\
 &= \sqrt{2}k_q \int_0^1 (1 + \sqrt{1 - x'}) \cdot \frac{n_q L}{n_{\max}} dx' \quad \left(x' = \frac{n_{\max}x}{n_q L}\right) \\
 &= \sqrt{2}k_q \cdot \left(1 + \frac{2}{3}\right) \cdot \frac{n_q L}{n_{\max}} \\
 &= \frac{5\sqrt{2}}{3} \frac{n_q}{n_{\max}} k_q L.
 \end{aligned} \tag{5.2}$$

Since  $n_q \propto q^2$  and  $k_q \propto q$ , the phase scales as  $\phi_q \propto q^3$ , which means that there is a chirp between harmonics and this chirp makes an individual pulse within a train longer. Effect of this chirp was studied by applying it to the spectrum shown in Fig. 5.12(a) by changing the value of the scale length  $L$ . The results are shown in Fig. 5.14.

Figure 5.14(a) shows some of the resulting pulse trains. This shows how the pulse train changes as the scale length is increased, i.e., as the chirp is increased. As the scale length grows, the pulse duration increases rapidly up to  $\sim 900$  as. When the scale length is below  $\sim 0.5\lambda$ , the pulse duration oscillates between  $\sim 500$  as and  $\sim 900$  as. Although the pulse duration appears to be short at the scale length of  $0.4\lambda$ , a large portion of the energy is contained in the wing of the main peak. The evolution of the pulse duration as a function of the scale length is shown in Fig. 5.14(b). I plotted only up to  $\sim 0.5\lambda$  because the shape of the pulse is severely distorted above this scale length and it is difficult to define the duration of the pulse. Since the harmonic



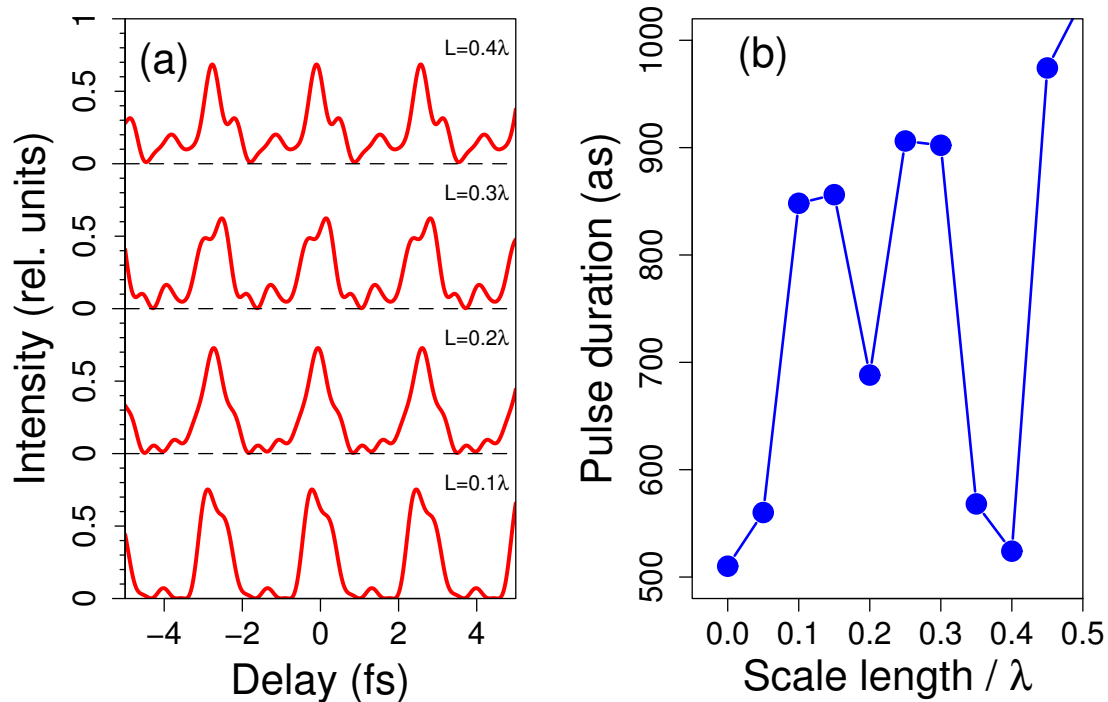


**Figure 5.14:** Attosecond pulse train with a chirp. (a) Attosecond pulse trains synthesized with different amount of chirps, coming from different scale lengths. The train without a chirp is already shown in Fig. 5.12(b). The distortion of the pulse shape becomes severe as the scale length becomes close to  $1\lambda$ , where a notable amount of the energy is contained in the wing. (b) Duration of the main pulse as a function of the scale length. The duration oscillates between 500 as to 900 as when the scale length is below  $0.8\lambda$ .

generation efficiency drops rapidly for longer scale lengths, it should be enough to study only the scale length below  $0.5\lambda$ . Nevertheless, the result of the model shows that the chirp of the CWE process can certainly broaden the duration of the pulse to the experimentally observed value of  $\sim 900$  as. Thus, the broadening of the individual pulse within the train is attributed to the chirp coming from the different reflection point in a plasma density profile for different harmonics.

## 5.6 Summary

In this chapter, I have presented the experimental results to characterize the temporal profile of the harmonics generated from the plasma surface.

First, the harmonics were focused into a gas jet to ionize helium through the two-photon ionization process. The use of Plexiglas targets was the key to suppress the XUV radiation above the ionization potential of helium and thus single-photon ionization of helium. This result provided a nonlinear process necessary for the autocorrelations measurements.

The coarse autocorrelation trace showed that the duration of the generated harmonics is approximately the same as that of the incident IR pulse. This result is consistent with the observation that the efficiency of the CWE process is linear to the incident IR intensity.

The fine autocorrelation trace revealed the sub-cycle structure in the generated harmonics. The average duration of the pulses within the train structure is obtained as  $\sim 900$  as. This is longer than the transform limit of the spectra in the gas jet, which is explained by a chirp introduced by the CWE process.

# Chapter 6

## Conclusions and outlook

In conclusion, volume autocorrelation measurements unveiled the temporal structure of the harmonics generated from the plasma–vacuum interface. The measurement was made possible by a thorough characterization of the properties of the harmonics, which enabled us to prepare the setup so that the necessary conditions are satisfied and any possible problems are excluded. The autocorrelation traces show that the harmonics are emitted in a form of an attosecond pulse train. Although the experiment was limited to the CWE harmonics, this result clearly indicates the great potential of surface HHG process as a source of attosecond pulses.

To fully exploit the benefits of surface HHG process, it is highly desirable to generate harmonics by the ROM process. Not only ROM harmonics extend to higher frequency region compared to CWE, but also have a smaller divergence and a better transverse coherence [114, 136]. The key to generate ROM harmonics is to improve the contrast of the laser pulses further. One possible method for improving the contrast is to use XPW [93], although this will require a major modification on the laser system itself. A plasma mirror is easier to implement, but it will severely limit the number of shots allowed for each experimental run.

Actually, the limitation on the number of laser shots is a big problem not only for the plasma mirror but also in the experiments of surface HHG itself. This is inherent to the surface HHG experiment, where the target must be ionized to generate a plasma. This problem can be alleviated by using a tape target, which will dramatically increase the number of shots allowed for each run. Liquid jet targets are even better because the number of shots will not be limited. On the other hand, it becomes more difficult to achieve a surface quality as good as that from rigid targets. Since the harmonics are generated during the reflection from the surface, a distorted surface will distort the wavefront of the reflected beam and lead to the deterioration of the XUV beam quality. Increasing the number of shots will require further technological improvements.

The measurement was also limited by a rather large divergence angle of the reflected beam. This was due to the tight focusing of the incident beam to achieve the high intensity necessary for the surface HHG process. This led to a correspondingly large divergence of the reflected beam, which made the handling of the beam difficult. More important thing to note is that the large divergence of the beam made it necessary to re-collimate the beam, i.e., an extra optic was required compared to gas HHG experiments. This extra reflection reduced the XUV intensity approximately by one order of magnitude. Although it is difficult to decrease the divergence an-

gle, it is possible to increase the reflectivity of the collection mirror by using a grazing incidence angle. One of the ideas is shown in Fig. 6.1. Re-collimation and focusing of the XUV beam are made with parabolas with large angles. Since the focusing is done with a parabola rather than a spherical mirror, a smaller focal spot is expected. The reflected IR beam is suppressed by two reflections on an appropriate material such as silicon plates or glass wedges. The split mirror can be placed between those two reflections, also at grazing incidence angle. Since the translation of the half of the split mirror does not change the direction of the beam, the beam will focus into the same position regardless of the delay. On the other hand, the energy distribution within the focal volume might change slightly and should be studied carefully. This setup will increase the XUV throughput and reduces the focal spot size at the same time, which will increase the usable XUV intensity significantly.

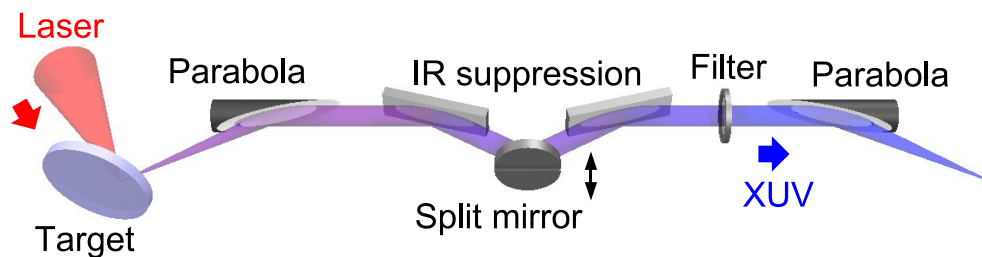


**Figure 6.1:** Setup only with grazing incidence. Re-collimating and focusing are done with grazing incidence parabolas. The reflected IR beam is suppressed by two reflections on an appropriate material such as silicon. The split mirror is placed between those two reflections, also at grazing incidence, and divides the beam vertically into two. Here it is designed so that the whole IR suppression unit does not change the path of the outgoing beam and can be moved out of the beam to make the alignment easier.

The autocorrelation measurements presented in the thesis took advantage of the property of CWE that no harmonic is generated above the plasma frequency. This property was used to restrict the generation of harmonics to only the ones necessary for two-photon ionization of helium. Although it was helpful for the first measurements, further experiments in different spectral regions require different nonlinear processes. In fact, many improvements to the experiment such as increasing the contrast to generate ROM harmonics or using the glass target to avoid target degradation will lead to higher-order harmonics and a nonlinear process that can be used for those spectral range is definitely necessary. One possibility is direct double ionization (DDI) of atoms by two XUV photons [123, 137, 138, 139]. The DDI process would allow use of higher photon energy without changing the experimental setup. For example, the usable photon energy is between 40 eV to 54 eV for helium. While the lower energy is determined by the energy necessary for ionizing helium into the second ionization stage with two photons, the upper energy is determined by the energy gap between the first and the second ionization. If the photon energy is higher than this level, the sequential double ionization process, which has no delay dependence [138], starts to dominate over the DDI process and masks the autocorrelation measurements. Another possibility is to observe the photoelectrons generated through above-threshold ionization

---

(ATI) processes [120, 121, 122]. Although detecting photoelectrons is generally a more demanding task compared to detecting ions, this method does not limit the usable photon energy and it is even possible to extend it to FROG-type measurement [126].

Finally, I would like to discuss the possibility to generate isolated attosecond pulses. With ATLAS laser system, the only possibility available is to apply the polarization-gating technique [79, 81]. On the other hand, it is not straightforward to implement it because of the high  $B$ -integral, as I mentioned in Section 2.3.2. A more promising route is to use our newly developed laser system LWS-10 [105, 140], which is based on optical parametric chirped-pulse amplification (OPCPA) and produces sub-10-fs pulses with 10 TW power. The biggest challenge was to obtain a high contrast necessary for the surface HHG process. In fact, an attempt made a year ago to generate harmonics from LWS-10 failed; observed radiation was only line emission from oxygen. Since then, LWS-10 has been under intensive development and the contrast of the output pulse has improved by 2 to 3 orders of magnitude. This improvement led to the observation of some harmonics in a recent experiment, which will be presented in the thesis of Rainer Hörlein. This is the first demonstration of harmonic generation from plasma surfaces using sub-10-fs pulse. Even though there are many challenges lying ahead, I believe this will lead to the generation of attosecond pulses with unprecedented intensities, which will open up a new regime of attosecond physics.



# Appendix A

## Useful formulas

### A.1 Values related to Gaussian beam

#### A.1.1 The Full Width Half Maximum

Assume a Gaussian beam

$$I(r, t) = I_0 \exp\left(-\frac{2r^2}{w_0^2}\right) \exp\left(-4 \ln 2 \frac{t^2}{\tau^2}\right), \quad (\text{A.1})$$

where  $I_0$  is the peak intensity,  $w_0$  the  $1/e^2$  radius, and  $\tau$  the pulse duration. The fluence  $\Phi(r)$  of the beam is obtained as

$$\Phi(r) = \int_{-\infty}^{\infty} I(r, t) dt = \Phi_0 \exp\left(-\frac{2r^2}{w_0^2}\right), \quad (\text{A.2})$$

where  $\Phi_0 = \sqrt{\pi/(4 \ln 2)} \cdot I_0 \tau$  is the peak fluence.

The FWHM of the beam is obtained as  $\text{FWHM} = 2r_{1/2}$ , where  $r_{1/2}$  satisfies  $\Phi(r_{1/2}) = \Phi_0/2$ . Therefore,  $r_{1/2} = w_0 \sqrt{\ln 2/2}$  and the relation between the FWHM and  $w_0$  is obtained as

$$\text{FWHM} = w_0 \sqrt{2 \ln 2}. \quad (\text{A.3})$$

The energy within a circle with diameter  $R$  is calculated as

$$\begin{aligned} \int_0^R \Phi(r) \cdot 2\pi r dr &= \int_0^R \Phi_0 e^{-ar^2} \cdot 2\pi r dr \quad (a = 2/w_0^2) \\ &= -\frac{\pi\Phi_0}{a} e^{-ar^2} \Big|_0^R = \frac{\pi\Phi_0}{a} (1 - e^{-aR^2}). \end{aligned} \quad (\text{A.4})$$

Since  $\exp[-a(r_{1/2})^2] = 1/2$ , the half of the energy is contained within the circle with the radius  $r_{1/2}$ , in other words, within the FWHM.

### A.1.2 Peak intensity and average intensity

The energy  $E$  within the Gaussian pulse of Eq. (A.1) is obtained as

$$\begin{aligned}
 E &= \int_{-\infty}^{\infty} dt \int_0^{\infty} 2\pi r dr I(r, t) \\
 &= I_0 \int_{-\infty}^{\infty} dt \exp\left(-4 \ln 2 \frac{t^2}{\tau^2}\right) \int_0^{\infty} 2\pi r \exp\left(-\frac{2r^2}{w_0^2}\right) \\
 &= I_0 \cdot \sqrt{\frac{\pi}{4 \ln 2}} \tau \cdot \frac{\pi w_0^2}{2} \\
 &= I_0 \cdot \sqrt{\frac{\pi}{4 \ln 2}} \tau \cdot \frac{\pi(\text{FWHM})^2}{4 \ln 2}
 \end{aligned} \tag{A.5}$$

where I used the following formulas and Eq. (A.3):

$$\int_0^{\infty} e^{-at^2} dt = \sqrt{\frac{\pi}{a}}, \tag{A.6}$$

$$\int_0^{\infty} e^{-ar^2} \cdot 2\pi r dr = -\frac{\pi}{a} \cdot e^{-ar^2} \Big|_0^{\infty} = \frac{\pi}{a}. \tag{A.7}$$

Thus the peak intensity of a Gaussian pulse is calculated from the pulse energy as

$$I_0 = \frac{E}{\tau(\text{FWHM})^2} \left(\frac{4 \ln 2}{\pi}\right)^{3/2} \sim \frac{0.83E}{\tau(\text{FWHM})^2}. \tag{A.8}$$

The average intensity  $I_{\text{avg}}$  can be defined as the average intensity within  $1/e^2$  radius. Since the energy within  $1/e^2$  radius can be calculated from Eq. (A.4) and gives  $(1 - e^{-2})E$ , the average intensity is obtained as

$$\begin{aligned}
 I_{\text{avg}} &= \frac{(1 - e^{-2})E}{\pi w_0^2 \tau} = \frac{2 \ln 2 (1 - e^{-2})E}{\pi \tau (\text{FWHM})^2} \\
 &\sim \frac{0.28E}{w_0^2 \tau} \sim \frac{0.38E}{\tau (\text{FWHM})^2}.
 \end{aligned} \tag{A.9}$$

### A.1.3 The RMS radius

The RMS distance of a Gaussian beam is obtained as

$$r_{\text{rms}}^2 = \frac{\int_0^{\infty} r^2 \Phi(r) \cdot 2\pi r dr}{\int_0^{\infty} \Phi(r) \cdot 2\pi r dr}. \tag{A.10}$$

The denominator is obtained from Eq. (A.7), while the numerator is obtained as

$$\begin{aligned}
 \int_0^{\infty} r^2 e^{-ar^2} \cdot 2\pi r dr &= -\frac{\pi r^2}{a} e^{-ar^2} \Big|_0^{\infty} + \frac{\pi}{a} \int_0^{\infty} 2r e^{-ar^2} \cdot 2\pi r dr \\
 &= -\frac{\pi}{a^2} e^{-ar^2} \Big|_0^{\infty} = \frac{\pi}{a^2}.
 \end{aligned} \tag{A.11}$$



Therefore, the RMS distance of the beam is

$$r_{\text{RMS}}^2 = \frac{\pi/a^2}{\pi/a} = \frac{1}{a} = \frac{w_0}{2}, \quad (\text{A.12})$$

$$r_{\text{RMS}} = \frac{w_0}{\sqrt{2}}. \quad (\text{A.13})$$

This value corresponds to the 1/e radius of the Gaussian beam.

## **A.2 Second-order interferometric autocorrelation**

For an electric field  $E(t) = A(t) \cos(\omega t + \phi)$ , the equation for the second-order interferometric autocorrelation is obtained as

$$\begin{aligned} \int_{-\infty}^{\infty} |E(t)E(t-\tau)|^2 dt &= \int_{-\infty}^{\infty} |E^2(t) + 2E^2(t)E^2(t-\tau) + E^2(t-\tau)|^2 dt \\ &= 2B_0 + 4 \int_{-\infty}^{\infty} A^2(t)A^2(t-\tau) dt \\ &\quad + 4 \int_{-\infty}^{\infty} A(t)A(t-\tau)[A^2(t) + A^2(t-\tau)] \cos(\omega\tau + \phi) dt \\ &\quad + 2 \int_{-\infty}^{\infty} A^2(t)A^2(t-\tau) \cos(2\omega\tau + 2\phi) dt, \end{aligned} \quad (\text{A.14})$$

where  $B_0 = \int_{-\infty}^{\infty} A^4(t) dt$  is a constant. If the envelope  $A(t)$  becomes 0 for  $t \rightarrow \infty$ , which is a reasonable assumption for a pulse, all the terms in Eq. (A.14) except for the first becomes 0 for  $\tau \rightarrow \infty$ . Therefore, the background level is  $2B_0$ . When  $\tau \rightarrow 0$ , on the other hand, the equation reduces to  $16B_0$ . Thus the peak-to-background ratio for a second-order interferometric autocorrelation is 8 : 1.



## Appendix B

### Simulation of the focus from the split mirror at oblique incidence

Here I will present the simulation I have made to estimate the focal spot and autocorrelation trace expected from the split mirror when angle of incidence is not normal. The simulation presented here is similar to the one made by Tzallas *et al.* [117]. Figure B.1 shows the scheme of the simulation.

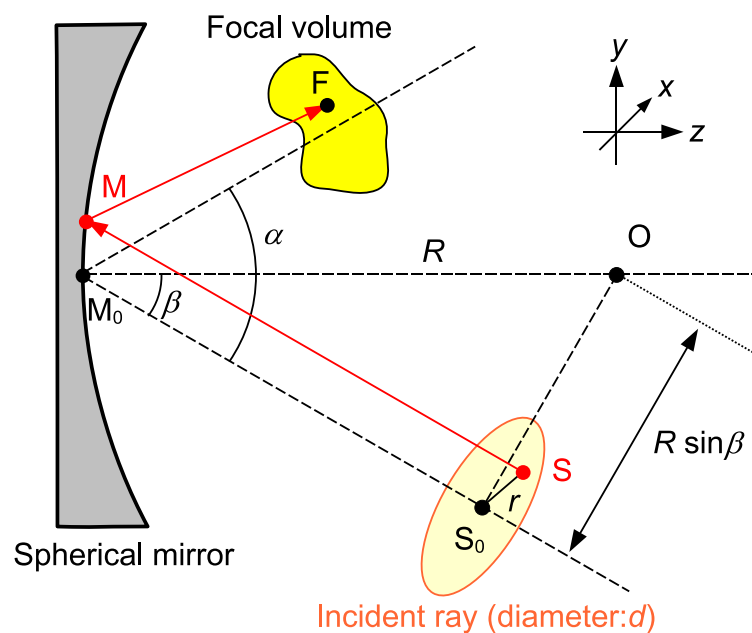


**Figure B.1:** Schematic diagram for the simulation. The meanings of the symbols are as follows.  $R$ : curvature of the spherical mirror;  $O$ : center of the sphere with radius  $R$ ;  $S_0$ : center of the incident ray;  $S$ : point on the incident ray;  $r$ : distance between  $S_0$  and  $S$ ;  $\alpha$ : reflection angle for the center of the ray;  $\beta$ : incidence angle,  $\beta = \alpha/2$ ;  $M_0, M$ : points on the mirror where the rays from points  $S_0$  and  $S$  arrive at.  $F$ : focal point, where contribution is calculated.

First I will treat the model analytically. The ray was assumed to have a round, flat-top profile with a diameter  $d$ . The angle of incidence is  $\beta$  onto a spherical mirror with the radius of curvature  $R$ . If I take the starting point of the ray  $S_0$  so that a line segment  $OS_0$  becomes perpendicular to the ray  $S_0M_0$ , the coordinate vector of  $S_0$  becomes

$$\vec{S}_0 = (0, -R \sin \beta \cos \beta, -R \sin^2 \beta). \quad (\text{B.1})$$

If I consider a point  $S$  on the initial plane perpendicular to the incident ray so that the distance from the center  $S_0$  is  $r$  and the angle from the  $x$ -axis is  $\theta$ , the coordinate vector can be written as

$$\begin{aligned} \vec{S} - \vec{S}_0 &= (r \cos \theta, r \sin \theta \cos \beta, r \sin \theta \sin \beta), & \left(0 \leq r \leq \frac{d}{2}, 0 \leq \theta < 2\pi\right) \\ \vec{S} &= (r \cos \theta, (-R \sin \beta + r \sin \theta) \cos \beta, (-R \sin \beta + r \sin \theta) \sin \beta). \end{aligned} \quad (\text{B.2})$$

Thus all the points on the incident ray is expressed by two parameters  $r$  and  $\theta$ .

Now I would like to calculate the contribution in the focal volume from each point. Since the beam is flat-top, amplitude is the same everywhere on the ray. The phase of the each ray can be obtained by calculating the distance the ray travels. Here I divide the distance into two: from the starting point to the mirror, and from the mirror to the focal volume.

The distance from the starting point  $S$  to the point  $M$  on the spherical mirror can be obtained analytically. The distance  $OM$  is always equal to  $R$  because  $M$  is a point on the sphere centered at  $O$ . Since the triangle  $OSM$  is a right triangle, the distance  $SM$  is obtained as

$$\begin{aligned} |\overline{SM}|^2 &= R^2 - |\vec{S}|^2 \\ &= R^2 - r^2 \cos^2 \theta - (-R \sin \beta + r \sin \theta)^2 (\cos^2 \beta + \sin^2 \beta) \\ &= R^2 \cos^2 \beta + 2Rr \sin \beta \sin \theta - r^2 \\ \overline{SM} &= \sqrt{R^2 \cos^2 \beta + 2Rr \sin \beta \sin \theta - r^2} \end{aligned} \quad (\text{B.3})$$

Since all the rays are parallel, the direction of  $\overrightarrow{SM}$  is parallel to  $\overrightarrow{S_0M_0} = S_0M_0(0, \sin \beta, \cos \beta)$ . Therefore, the coordinate of the intersection point  $M$  is obtained as

$$\vec{M} = \overrightarrow{OS} + \overrightarrow{SM}, \quad \text{where } \overrightarrow{SM} = \sqrt{R^2 \cos^2 \beta + 2Rr \sin \beta \sin \theta - r^2} \begin{pmatrix} 0 \\ \sin \beta \\ \cos \beta \end{pmatrix} \quad (\text{B.4})$$

The distance from the intersection point  $M$  to a point  $F$  in the focal volume will be calculated numerically. To make the calculation easier, the coordinate system was changed so that the  $z$ -axis becomes parallel to the center of the reflected ray and the center of the coordinate system is located at the point  $R/2$  away from the spherical mirror, as shown in Fig. B.2. The transformation is made by rotating around the  $x$ -axis by angle  $\beta$  in clockwise direction, and then translating by  $(0, -R \sin \beta, R \cos \beta - R/2)$ . Since this transformation includes only rotation and translation, the distances obtained above are not changed. The coordinate of the starting point  $S$  and the direction

of the ray  $\vec{SM}$  change to

$$\vec{S} = \begin{pmatrix} r \cos \theta \\ (-R \sin \beta + r \sin \theta) \cos 2\beta - R \sin \beta \\ (-R \sin \beta + r \sin \theta) \sin 2\beta + R \cos \beta - R/2 \end{pmatrix}, \quad (\text{B.5})$$

$$\vec{SM} = \sqrt{R^2 \cos^2 \beta + 2Rr \sin \beta \sin \theta - r^2} \begin{pmatrix} 0 \\ \sin 2\beta \\ \cos 2\beta \end{pmatrix} \quad (\text{B.6})$$

respectively. From these equations, the coordinate of M in the new coordinate system is also obtained. Once the coordinate of M is obtained, the distance each ray travels can be calculated for each point F in the focal volume.

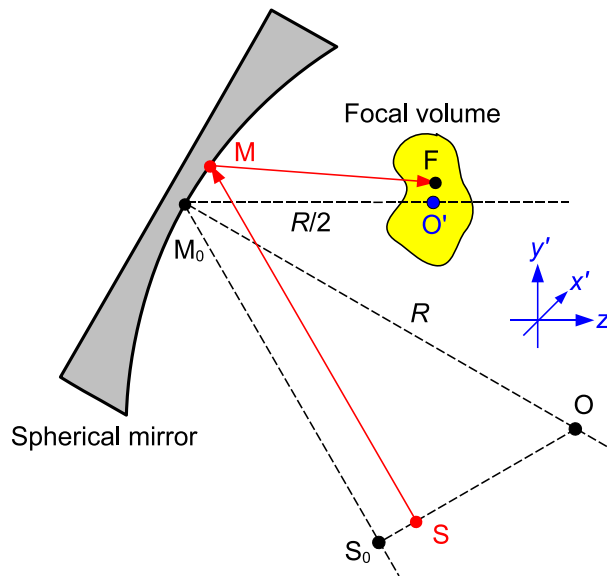


**Figure B.2:** New coordinate system after rotation and translation.

The rest of the calculation was done numerically. The focal volume was defined as a rectangular box. For each point F in the focal volume, the contribution from the each part of the ray was calculated by calculating the distance each ray travels from the initial plane. The distance was translated into the phase of each ray, and summing up everything gives the overall intensity at the point F.

Introducing the effect of the split mirror is rather simple. In the actual experiment, half of the split mirror is scanned parallelly to the incoming beam. This means that the intersection point shifts by  $\Delta d$  when the half of the split mirror is shifted by the same amount. Since moving the split mirror does not affect the incoming ray, the direction of the ray does not change and only the distance changes by  $\Delta d$ . Therefore, the coordinate of M shifts accordingly for half of the ray. Once the coordinate of M is obtained, the distance each ray travels can be obtained in the same way.

The simulation code was written in a computer language R [141]. Figure B.3 shows some of the images of the beam profile obtained by the simulation, assuming the IR incident ray at 800 nm with 50 mm diameter. No delay was included for the images in the upper row, while a half-cycle delay from the split mirror was introduced for the images in the lower row. For the actual simulation, three harmonics from 8th order to 10th order was used, which corresponds to the harmonics transmitted through an indium filter. The obtained autocorrelation is presented in Section 5.2.2.

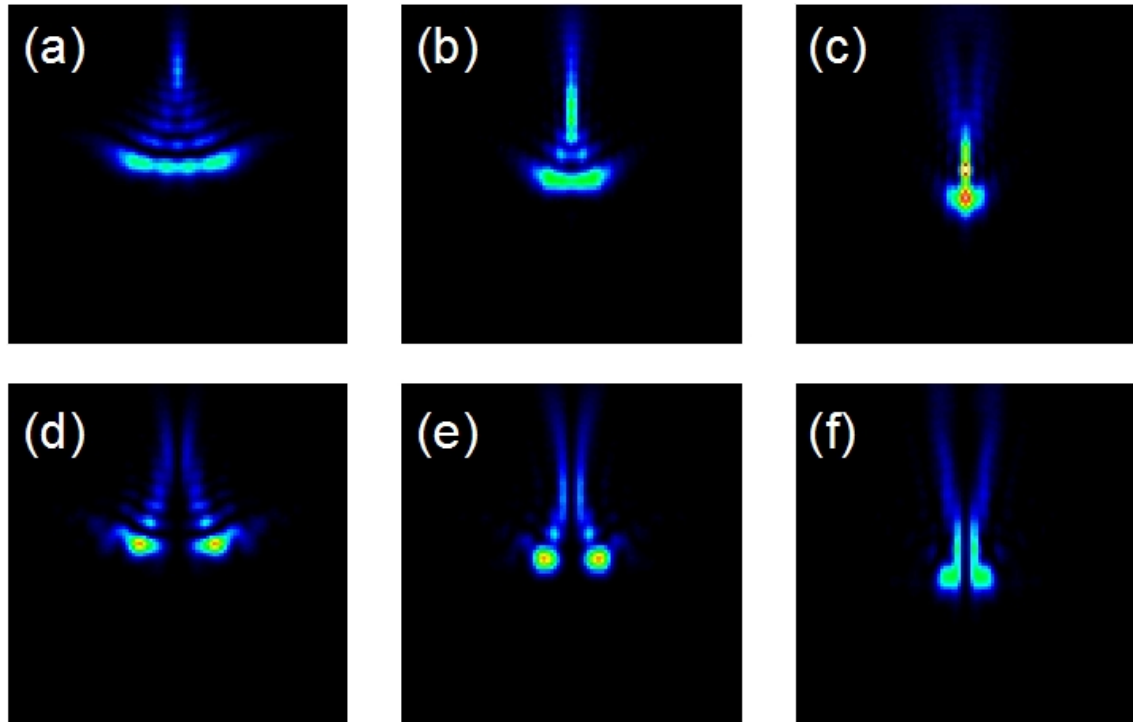


**Figure B.3:** Examples of images around the focus with IR beam obtained by the simulation. (a-c) Images with no delay. (d-f) Images with half-cycle delay from the split mirror.

# Bibliography

- [1] M. Hentschel, R. Kienberger, Ch. Spielmann, G. A. Reider, N. Milosevic, T. Brabec, P. Corkum, U. Heinzmann, M. Drescher, and F. Krausz, “Attosecond metrology,” *Nature* **414**, 509 (2001).
- [2] A. D. Bandrauk, F. Krausz, and A. F. Starace, “Focus on attosecond physics,” *New J. Phys.* **10**, 025004 (2008).
- [3] E. Goulielmakis, M. Uiberacker, R. Kienberger, A. Baltuska, V. Yakovlev, A. Scrinzi, Th. Westerwalbesloh, U. Kleineberg, U. Heinzmann, M. Drescher, and F. Krausz, “Direct measurement of light waves,” *Science* **305**, 1267 (2004).
- [4] M. Uiberacker, Th. Uphues, M. Schultze, A. J. Verhoef, V. Yakovlev, M. F. Kling, J. Rauschenberger, N. M. Kabachnik, H. Schröder, M. Lezius, K. L. Kompa, H.-G. Muller, M. J. J. Vrakking, S. Hendel, U. Kleineberg, U. Heinzmann, M. Drescher, and F. Krausz, “Attosecond real-time observation of electron tunnelling in atoms,” *Nature* **446**, 627 (2007).
- [5] A. L. Cavalieri, N. Müller, Th. Uphues, V. S. Yakovlev, A. Baltuška, B. Horvath, B. Schmidt, L. Blümel, R. Holzwarth, S. Hendel, M. Drescher, U. Kleineberg, P. M. Echenique, R. Kienberger, F. Krausz, and U. Heinzmann, “Attosecond spectroscopy in condensed matter,” *Nature* **449**, 1029 (2007).
- [6] P. B. Corkum, “Plasma perspective on strong field multiphoton ionization,” *Phys. Rev. Lett.* **71**, 1994 (1993).
- [7] M. Lewenstein, Ph. Balcou, M. Yu. Ivanov, A. L’Huillier, and P. B. Corkum, “Theory of high-harmonic generation by low-frequency laser fields,” *Phys. Rev. A* **49**, 2117 (1994).
- [8] T. W. Hänsch, “A proposed sub-femtosecond pulse synthesizer using separate phase-locked laser oscillators,” *Opt. Commun.* **80**, 71 (1990).
- [9] Gy. Farkas and Cs. Tóth, “Proposal for attosecond light pulse generation using laser induced multiple-harmonic conversion processes in rare gases,” *Phys. Lett. A* **168**, 447 (1992).
- [10] S. E. Harris, J. J. Macklin, and T. W. Hänsch, “Atomic scale temporal structure inherent to high-order harmonic generation,” *Opt. Commun.* **100**, 487 (1993).

- [11] Ph. Antoine, A. L’Huillier, and M. Lewenstein, “Attosecond pulse trains using high-order harmonics,” *Phys. Rev. Lett.* **77**, 1234 (1996).
- [12] P. B. Corkum, N. H. Burnett, and M. Y. Ivanov, “Subfemtosecond pulses,” *Opt. Lett.* **19**, 1870 (1994).
- [13] K. J. Schafer and K. C. Kulander, “High harmonic generation from ultrafast pump lasers,” *Phys. Rev. Lett.* **78**, 638 (1997).
- [14] I. P. Christov, M. M. Murnane, and H. C. Kapteyn, “High-harmonic generation of attosecond pulses in the “single-cycle” regime,” *Phys. Rev. Lett.* **78**, 1251 (1997).
- [15] N. A. Papadogiannis, B. Witzel, C. Kalpouzos, and D. Charalambidis, “Observation of attosecond light localization in higher order harmonic generation,” *Phys. Rev. Lett.* **83**, 4289 (1999).
- [16] P. M. Paul, E. S. Toma, P. Breger, G. Mullot, F. Augé, Ph. Balcou, H. G. Muller, and P. Agostini, “Observation of a train of attosecond pulses from high harmonic generation,” *Science* **292**, 1689 (2001).
- [17] P. Tzallas, D. Charalambidis, N. A. Papadogiannis, K. Witte, and G. D. Tsakiris, “Direct observation of attosecond light bunching,” *Nature* **426**, 267 (2003).
- [18] R. Kienberger, E. Goulielmakis, M. Uiberacker, A. Baltuska, V. Yakovlev, F. Bammer, A. Scrinzi, Th. Westerwalbesloh, U. Kleineberg, U. Heinzmann, M. Drescher, and F. Krausz, “Atomic transient recorder,” *Nature* **427**, 817 (2004).
- [19] G. Sansone, E. Benedetti, F. Calegari, C. Vozzi, L. Avaldi, R. Flammini, L. Poletto, P. Villoresi, C. Altucci, R. Velotta, S. Stagira, S. De Silvestri, and M. Nisoli, “Isolated single-cycle attosecond pulses,” *Science* **314**, 443 (2006).
- [20] A. Rundquist, C. G. Durfee III, Z. Chang, C. Herne, S. Backus, M. M. Murnane, and H. C. Kapteyn, “Phase-matched generation of coherent soft x-rays,” *Science* **280**, 1412 (1998).
- [21] Y. Tamaki, J. Itatani, Y. Nagata, M. Obara, and K. Midorikawa, “Highly efficient, phase-matched high-harmonic generation by a self-guided laser beam,” *Phys. Rev. Lett.* **82**, 1422 (1999).
- [22] E. Constant, D. Garzella, P. Breger, E. Mével, Ch. Dorrer, C. Le Blanc, F. Salin, and P. Agostini, “Optimizing high harmonic generation in absorbing gases: Model and experiment,” *Phys. Rev. Lett.* **82**, 1668 (1999).
- [23] L. Roos, E. Constant, E. Mével, Ph. Balcou, D. Descamps, M. B. Gaarde, A. Valette, R. Haroutunian, and A. L’Huillier, “Controlling phase matching of high-order harmonic generation by manipulating the fundamental field,” *Phys. Rev. A* **60**, 5010 (1999).



- [24] E. Takahashi, Y. Nabekawa, T. Otsuka, M. Obara, and K. Midorikawa, "Generation of highly coherent submicrojoule soft x rays by high-order harmonics," *Phys. Rev. A* **66**, 021802(R) (2002).
- [25] J.-F. Hergott, M. Kovacev, H. Merdji, C. Hubert, Y. Mairesse, E. Jean, P. Breger, P. Agostini, B. Carré, and P. Salières, "Extreme-ultraviolet high-order harmonic pulses in the microjoule range," *Phys. Rev. A* **66**, 021801(R) (2002).
- [26] S. Kazamias, D. Douillet, F. Weihe, C. Valentin, A. Rousse, S. Sebban, G. Grillon, F. Augé, D. Hulin, and Ph. Balcou, "Global optimization of high harmonic generation," *Phys. Rev. Lett.* **90**, 193901 (2003).
- [27] G. D. Tsakiris, K. Eidmann, J. Meyer-ter-Vehn, and F. Krausz, "Route to intense single attosecond pulses," *New J. Phys.* **8**, 19 (2006).
- [28] S. Kohlweyer, G. D. Tsakiris, C.-G. Wahlström, C. Tillman, and I. Mercer, "Harmonic generation from solid-vacuum interface irradiated at high laser intensities," *Opt. Commun.* **117**, 431 (1995).
- [29] P. A. Norreys, M. Zepf, S. Mousaizis, A. P. Fews, J. Zhang, P. Lee, M. Bakarezos, C. N. Danson, A. Dyson, P. Gibbon, P. Loukakos, D. Neely, F. N. Walsh, J. S. Wark, and D. A. E., "Efficient extreme UV harmonics generated from picosecond laser pulse interactions with solid targets," *Phys. Rev. Lett.* **76**, 1832 (1996).
- [30] R. Lichters, J. Meyer-ter-Vehn, and A. Pukhov, "Short-pulse laser harmonics from oscillating plasma surfaces driven at relativistic intensity," *Phys. Plasmas* **3**, 3425 (1996).
- [31] M. Zepf, G. D. Tsakiris, G. Pretzler, I. Watts, D. M. Chambers, P. A. Norreys, U. Andiel, A. E. Dangor, K. Eidmann, C. Gahn, A. Machacek, J. S. Wark, and K. Witte, "Role of the plasma scale length in the harmonic generation from solid targets," *Phys. Rev. E* **58**, R5253 (1998).
- [32] T. Baeva, S. Gordienko, and A. Pukhov, "Theory of high-order harmonic generation in relativistic laser interaction with overdense plasma," *Phys. Rev. E* **74**, 046404 (2006).
- [33] B. Dromey, M. Zepf, A. Gopal, K. Lancaster, M. S. Wei, K. Krushelnick, M. Tatarakis, N. Vakakis, S. Mousaizis, R. Kodama, M. Tambo, C. Stoeckl, R. Clarke, H. Habara, D. Neely, S. Karsch, and P. Norreys, "High harmonic generation in the relativistic limit," *Nature Phys.* **2**, 456 (2006).
- [34] F. Quéré, C. Thaury, P. Monot, S. Dobosz, Ph. Martin, J.-P. Geindre, and P. Audebert, "Coherent wake emission of high-order harmonics from overdense plasmas," *Phys. Rev. Lett.* **96**, 125004 (2006).
- [35] N. H. Burnett, H. A. Baldis, M. C. Richardson, and G. D. Enright, "Harmonic generation in CO<sub>2</sub> laser target interaction," *Appl. Phys. Lett.* **31**, 172 (1977).

- [36] R. L. Carman, D. W. Forslund, and J. M. Kindel, "Visible harmonic emission as a way of measuring profile steepening," *Phys. Rev. Lett.* **46**, 29 (1981).
- [37] R. L. Carman, C. K. Rhodes, and R. F. Benjamin, "Observation of harmonics in the visible and ultraviolet created in CO<sub>2</sub>-laser-produced plasmas," *Phys. Rev. A* **24**, 2649 (1981).
- [38] B. Bezzerides, R. D. Jones, and D. W. Forslund, "Plasma mechanism for ultraviolet harmonic radiation due to intense CO<sub>2</sub> light," *Phys. Rev. Lett.* **49**, 202 (1982).
- [39] C. Grebogi, V. K. Tripathi, and H.-H. Chen, "Harmonic generation of radiation in a steep density profile," *Phys. Fluids* **26**, 1904 (1983).
- [40] D. von der Linde, T. Engers, G. Jenke, P. Agostini, G. Grillon, E. Nibbering, A. Mysyrowicz, and A. Antonetti, "Generation of high-order harmonics from solid surfaces by intense femtosecond laser pulses," *Phys. Rev. A* **52**, R25 (1995).
- [41] P. Gibbon, "Harmonic generation by femtosecond laser-solid interaction: A coherent "water-window" light source?," *Phys. Rev. Lett.* **76**, 50 (1996).
- [42] S. V. Bulanov, N. M. Naumova, and F. Pegoraro, "Interaction of an ultrashort, relativistically strong laser pulse with an overdense plasma," *Phys. Plasmas* **1**, 745 (1994).
- [43] D. von der Linde and K. Rzàzewski, "High-order optical harmonic generation from solid surfaces," *Appl. Phys. B* **63**, 499 (1996).
- [44] P. Gibbon, "High-order harmonic generation in plasmas," *IEEE J. Quantum Electron.* **33**, 1915 (1997).
- [45] A. Tarasevitch, A. Orisch, D. von der Linde, Ph. Balcou, G. Rey, J.-P. Chambaret, U. Teubner, D. Klöpfel, and W. Theobald, "Generation of high-order spatially coherent harmonics from solid targets by femtosecond laser pulses," *Phys. Rev. A* **62**, 023816 (2000).
- [46] I. B. Földes, J. S. Bakos, Z. Bakonyi, T. Nagy, and S. Szatmári, "Harmonic generation in plasmas of different density gradients," *Phys. Lett. A* **258**, 312 (1999).
- [47] A. Ishizawa, T. Kanai, T. Ozaki, and H. Kuroda, "Enhancement of high-order harmonic generation efficiency from solid-surface plasma by controlling the electron density gradient of picosecond laser-produced plasmas," *IEEE J. Quantum Electron.* **37**, 384 (2001).
- [48] P. Monot, G. Doumy, S. Dobosz, M. Perdrix, P. D'Oliveira, F. Quéré, F. Réau, Ph. Martin, P. Audebert, J.-C. Gauthier, and J.-P. Geindre, "High-order harmonic generation by nonlinear reflection of an intense high-contrast laser pulse on a plasma," *Opt. Lett.* **29**, 893 (2004).
- [49] J. Zhang, M. Zepf, P. A. Norreys, A. E. Dangor, M. Bakarezos, C. N. Danson, A. Dyson, A. P. Fews, P. Gibbon, M. H. Key, P. Lee, P. Loukakos, S. Moustazis, D. Neely, F. N. Walsh, and J. S. Wark, "Coherence and bandwidth measurements of harmonics generated

- from solid surfaces irradiated by intense picosecond laser pulses,” *Phys. Rev. A* **54**, 1597 (1996).
- [50] G. Veres, J. S. Bakos, I. B. Földes, K. Gál, Z. Juhász, G. Kocsis, and S. Szatmári, “Polarization of harmonics generated by ultrashort KrF-laser pulses on solid surfaces,” *Europhys. Lett.* **48**, 390 (1999).
- [51] A. Ishizawa, K. Inaba, T. Kanai, T. Ozaki, and H. Kuroda, “High-order harmonic generation from a solid surface plasma by using a picosecond laser,” *IEEE J. Quantum Electron.* **35**, 60 (1999).
- [52] E. Rácz, I. B. Földes, G. Kocsis, G. Veres, K. Eidmann, and S. Szatmári, “On the effect of surface rippling on the generation of harmonics in laser plasmas,” *Appl. Phys. B* **82**, 13 (2006).
- [53] I. Watts, M. Zepf, E. L. Clark, M. Tatarakis, K. Krushelnick, A. E. Dangor, R. M. Allott, R. J. Clarke, D. Neely, and P. A. Norreys, “Dynamics of the critical surface in high-intensity laser-solid interactions: Modulation of the XUV harmonic spectra,” *Phys. Rev. A* **88**, 155001 (2002).
- [54] U. Teubner, G. Pretzler, Th. Schlegel, K. Eidmann, E. Förster, and K. Witte, “Anomalies in high-order harmonic generation at relativistic intensities,” *Phys. Rev. A* **67**, 013816 (2003).
- [55] L. Plaja, L. Roso, K. Rzażewski, and M. Lewenstein, “Generation of attosecond pulse trains during the reflection of a very intense laser on a solid surface,” *J. Opt. Soc. Am. B* **15**, 1904 (1998).
- [56] N. M. Naumova, J. A. Nees, I. V. Sokolov, B. Hou, and G. A. Mourou, “Relativistic generation of isolated attosecond pulses in a  $\lambda^3$  focal volume,” *Phys. Rev. Lett.* **92**, 063902 (2004).
- [57] S. Gordienko, A. Pukhov, O. Shorokhov, and T. Baeva, “Relativistic Doppler effect: Universal spectra and zeptosecond pulses,” *Phys. Rev. Lett.* **93**, 115002 (2004).
- [58] B. Dromey, S. Kar, C. Bellei, D. C. Carroll, R. J. Clarke, J. S. Green, S. Kneip, K. Markey, S. R. Nagel, P. T. Simpson, L. Willingale, P. McKenna, D. Neely, Z. Najmudin, K. Krushelnick, P. A. Norreys, and M. Zepf, “Bright multi-keV harmonic generation from relativistically oscillating plasma surfaces,” *Phys. Rev. Lett.* **99**, 085001 (2007).
- [59] C. Thaury, F. Quéré, J.-P. Geindre, A. Levy, T. Ceccotti, P. Monot, M. Bougeard, F. Réau, P. D’Oliveira, P. Audebert, R. Marjoribanks, and Ph. Martin, “Plasma mirrors for ultrahigh-intensity optics,” *Nature Phys.* **3**, 424 (2007).
- [60] A. Tarasevitch, K. Lobov, C. Wünsche, and D. von der Linde, “Transition to the relativistic regime in high order harmonic generation,” *Phys. Rev. Lett.* **98**, 103902 (2007).

- [61] L. D. Landau and E. M. Lifshitz, *The Classical Theory of Fields*, Vol. 2 of *Landau and Lifshitz Course of Theoretical Physics*, 4th revised English ed. (Pergamon Press, Oxford, 1975).
- [62] E. S. Sarachik and G. T. Schappert, “Classical theory of the scattering of intense laser radiation by free electrons,” *Phys. Rev. D* **1**, 2738 (1970).
- [63] F. Brunel, “Not-so-resonant, resonant absorption,” *Phys. Rev. Lett.* **59**, 52 (1987).
- [64] Z.-M. Sheng, K. Mima, J. Zhang, and H. Sanuki, “Emission of electromagnetic pulses from laser wakefields through linear mode conversion,” *Phys. Rev. Lett.* **94**, 095003 (2005).
- [65] K. Varjú, Y. Mairesse, B. Carré, M. B. Gaarde, P. Johnsson, S. Kazamias, R. López-Martens, J. Mauritsson, K. J. Schafer, Ph. Balcou, A. L’Huillier, and Salières, “Frequency chirp of harmonic and attosecond pulses,” *J. Mod. Opt.* **52**, 379 (2005).
- [66] L. Roso, L. Plaja, K. Rzażewski, and D. von der Linde, “Beyond the moving mirror model: Attosecond pulses from a relativistically moving plasma,” *Laser Part. Beams* **18**, 467 (2001).
- [67] M. Drescher, M. Hentschel, R. Kienberger, M. Uiberacker, V. Yakovlev, A. Scrinzi, Th. Westerwalbesloh, U. Kleineberg, U. Heinzmann, and F. Krausz, “Time-resolved atomic inner-shell spectroscopy,” *Nature* **419**, 803 (2002).
- [68] L. Xu, Ch. Spielmann, A. Poppe, T. Brabec, F. Krausz, and T. W. Hänsch, “Route to phase control of ultrashort light pulses,” *Opt. Lett.* **21**, 2008 (1996).
- [69] P. Dietrich, F. Krausz, and P. B. Corkum, “Determining the absolute carrier phase of a few-cycle laser pulse,” *Opt. Lett.* **25**, 16 (2000).
- [70] A. Baltuška, Th. Udem, M. Uiberacker, M. Hentschel, E. Goulielmakis, Ch. Gohle, R. Holzwarth, V. S. Yakovlev, A. Scrinzi, T. W. Hänsch, and F. Krausz, “Attosecond control of electronic processes by intense light fields,” *Nature* **421**, 611 (2003).
- [71] K. S. Budil, P. Salières, A. L’Huillier, T. Ditmire, and M. D. Perry, “Influence of ellipticity on harmonic generation,” *Phys. Rev. A* **48**, R3437 (1993).
- [72] Ph. Antoine, A. L’Huillier, M. Lewenstein, P. Salières, and B. Carré, “Theory of high-order harmonic generation by an elliptically polarized laser field,” *Phys. Rev. A* **53**, 1725 (1996).
- [73] N. A. Papadogiannis, E. Nersisyan, G. Goulielmakis, M. Decros, M. Tatarakis, E. Hertz, L. A. A. Nikolopoulos, and D. Charalambidis, *Attosecond science: Present status and prospects in XIV International Symposium on Gas Flow, Chemical Lasers, and High-Power Lasers*, Vol. 5120 of *Proceedings of SPIE*, edited by K. M. Abramski, E. F. Plinski, and W. Wolinski (SPIE, Bellingham, WA, 2003), pp. 269–274.

- [74] V. T. Platonenko and V. V. Strelkov, "Single attosecond soft-x-ray pulse generated with a limited laser beam," *J. Opt. Soc. Am. B* **16**, 435 (1999).
- [75] M. Kovačev, Y. Mairesse, E. Priori, H. Merdji, O. Tcherbakoff, P. Monchicourt, P. Breger, E. Mével, E. Constant, P. Salières, B. Carré, and P. Agostini, "Temporal confinement of the harmonic emission through polarization gating," *Eur. Phys. J. D* **26**, 79 (2003).
- [76] O. Tcherbakoff, E. Mével, D. Descamps, J. Plumridge, and E. Constant, "Time-gated high-order harmonic generation," *Phys. Rev. A* **68**, 043804 (2003).
- [77] P. Tzallas, E. Skantzakis, C. Kalpouzous, B. P. Benis, G. D. Tsakiris, and D. Charalambidis, "Generation of intense continuum extreme-ultraviolet radiation by many-cycle laser fields," *Nature Phys.* **3**, 846 (2007).
- [78] I. J. Sola, E. Mével, L. Elouga, E. Constant, V. Strelkov, L. Poletto, P. Villoresi, E. Benedetti, J.-P. Caumes, S. Stagira, C. Vozzi, G. Sansone, and M. Nisoli, "Controlling attosecond electron dynamics by phase-stabilized polarization gating," *Nature Phys.* **2**, 319 (2006).
- [79] D. Charalambidis, P. Tzallas, E. P. Benis, E. Skantzakis, G. Maravelias, L. A. A. Nikolopoulos, A. Peralta Conde, and G. D. Tsakiris, "Exploring intense attosecond pulses," *New J. Phys.* **10**, 025018 (2008).
- [80] T. Baeva, S. Gordienko, and A. Pukhov, "Relativistic plasma control for single attosecond x-ray burst generation," *Phys. Rev. E* **74**, 065401 (2006).
- [81] S. G. Rykovanov, M. Geissler, J. Meyer-ter-Vehn, and G. D. Tsakiris, "Intense single attosecond pulses from surface harmonics using the polarization gating technique," *New J. Phys.* **10**, 025025 (2008).
- [82] A. E. Siegman, *Lasers* (University Science Books, Sausalito, CA, 1986).
- [83] W. L. Kruer, *The Physics of Laser Plasma Interactions* (Addison-Wesley, Redwood City, CA, 1988).
- [84] R. Lichters, R. E. W. Pfund, and J. Meyer-ter-Vehn, *LPIC++: A Parallel One-dimensional Relativistic Electromagnetic Particle-in-cell Code for Simulating Laser Plasma Interaction* (Max-Planck-Institut für Quantenoptik, Garching, Germany, 1997), No. MPQ-225.
- [85] D. Strickland and G. Mourou, "Compression of amplified chirped optical pulses," *Opt. Commun.* **56**, 219 (1985).
- [86] B. C. Stuart, M. D. Feit, S. Herman, A. M. Rubenchik, B. W. Shore, and M. D. Perry, "Nanosecond-to-femtosecond laser-induced breakdown in dielectrics," *Phys. Rev. B* **53**, 1749 (1996).

- [87] A. Maksimchuk, S. Gu, K. Flippo, D. Umstadter, and V. Yu. Bychenkov, "Forward ion acceleration in thin films driven by a high-intensity laser," *Phys. Rev. Lett.* **84**, 4108 (2000).
- [88] B. M. Hegelich, B. J. Albright, J. Cobble, K. Flippo, S. Letzring, M. Paffett, H. Ruhl, J. Schreiber, R. K. Schulze, and J. C. Fernández, "Laser acceleration of quasi-monoenergetic MeV ion beams," *Nature* **439**, 441 (2006).
- [89] A. Renault, F. Augé-Rochereau, T. Planchon, P. D'Oliveira, T. Auguste, G. Chériaux, and J.-P. Chambaret, "ASE contrast improvement with a non-linear filtering Sagnac interferometer," *Opt. Commun.* **248**, 535 (2005).
- [90] D. Homoelle, A. L. Gaeta, V. Yanovsky, and G. Mourou, "Pulse contrast enhancement of high-energy pulses by use of a gas-filled hollow waveguide," *Opt. Lett.* **27**, 1646 (2002).
- [91] A. Jullien, F. Augé-Rochereau, G. Chériaux, J.-P. Chambaret, P. d'Oliveira, T. Auguste, and F. Falcoz, "High-efficiency, simple setup for pulse cleaning at the millijoule level by nonlinear induced birefringence," *Opt. Lett.* **29**, 2184 (2004).
- [92] M. P. Kalashnikov, E. Risse, H. Schönagel, A. Husakou, J. Herrmann, and W. Sandner, "Characterization of a nonlinear filter for the front-end of a high contrast double-CPA Ti:sapphire laser," *Opt. Express* **12**, 5088 (2004).
- [93] A. Jullien, O. Albert, F. Burgy, G. Hamoniaux, J.-P. Rousseau, J.-P. Chambaret, F. Augé-Rochereau, G. Chériaux, J. Etchepare, N. Minkovski, and S. M. Saitiel, " $10^{-10}$  temporal contrast for femtosecond ultraintense lasers by cross-polarized wave generation," *Opt. Lett.* **30**, 920 (2005).
- [94] V. Chvykov, P. Rousseau, S. Reed, G. Kalinchenko, and V. Yanovsky, "Generation of  $10^{11}$  contrast 50 TW laser pulses," *Opt. Lett.* **31**, 1456 (2006).
- [95] H. C. Kapteyn, M. M. Murnane, A. Szoke, and R. W. Falcone, "Prepulse energy suppression for high-energy ultrashort pulses using self-induced plasma shuttering," *Opt. Lett.* **16**, 490 (1991).
- [96] Ch. Ziener, P. S. Foster, E. J. Divall, C. J. Hooker, M. H. R. Hutchinson, A. J. Langley, and D. Neely, "Specular reflectivity of plasma mirrors as a function of intensity, pulse duration, and angle of incidence," *J. Appl. Phys.* **93**, 768 (2002).
- [97] G. Doumy, F. Quéré, O. Gobert, M. Perdrix, Ph. Martin, P. Audebert, J. C. Gauthier, J.-P. Geindre, and T. Wittmann, "Complete characterization of a plasma mirror for the production of high-contrast ultraintense laser pulses," *Phys. Rev. E* **69**, 026402 (2004).
- [98] B. Dromey, S. Kar, M. Zepf, and P. Foster, "The plasma mirror—a subpicosecond optical switch for ultrahigh power lasers," *Rev. Sci. Instrum.* **75**, 645 (2004).

- [99] T. Wittmann, J. P. Geindre, P. Audebert, R. Marjoribanks, J. P. Rousseau, F. Burgy, D. Douillet, T. Lefrou, K. Ta Phuoc, and J. P. Chambaret, “Towards ultrahigh-contrast ultraintense laser pulses—complete characterization of a double plasma-mirror pulse cleaner,” *Rev. Sci. Instrum.* **77**, 083109 (2006).
- [100] S. Backus, H. C. Kapteyn, M. M. Murnane, D. M. Gold, H. Nathel, and W. White, “Pre-pulse suppression for high-energy ultrashort pulses using self-induced plasma shuttering from a fluid target,” *Opt. Lett.* **18**, 134 (1993).
- [101] A. Lévy, T. Ceccotti, P. D’Oliveira, F. Réau, M. Perdrix, F. Quéré, P. Monot, M. Bougeard, H. Lagadec, P. Martin, J.-P. Geindre, and P. Audebert, “Double plasma mirror for ultrahigh temporal contrast ultraintense laser pulses,” *Opt. Lett.* **32**, 310 (2007).
- [102] M. Geissler, J. Schreiber, and J. Meyer-ter-Vehn, “Bubble acceleration of electrons with few-cycle laser pulses,” *New J. Phys.* **8**, 186 (2006).
- [103] A.-J. Verhoef, J. Seres, K. Schmid, Y. Nomura, G. Tempea, L. Veisz, and F. Krausz, “Compression of the pulses of a Ti:sapphire laser system to 5 femtoseconds at 0.2 terawatt level,” *Appl. Phys. B* **82**, 513 (2006).
- [104] N. K. Moncur, “Plasma spatial filter,” *Appl. Opt.* **16**, 1449 (1977).
- [105] F. Tavella, K. Schmid, N. Ishii, A. Marcinkevičius, L. Veisz, and F. Krausz, “High-dynamic range pulse-contrast measurements of a broadband optical parametric chirped-pulse amplifier,” *Appl. Phys. B* **81**, 753 (2005).
- [106] M. Hentschel, S. Uemura, Z. Cheng, S. Sartania, G. Tempea, Ch. Spielmann, and F. Krausz, “High-dynamic-range pulse-front steepening of amplified femtosecond pulses by third-order dispersion,” *Appl. Phys. B* **68**, 145 (1999).
- [107] J. P. Christiansen, D. E. T. F. Ashby, and K. V. Roberts, “MEDUSA a one-dimensional laser fusion code,” *Comput. Phys. Commun.* **7**, 271 (1974).
- [108] P. Gibbon and A. R. Bell, “Collisionless absorption in sharp-edged plasmas,” *Phys. Rev. Lett.* **68**, 1535 (1992).
- [109] H. Baumhacker, A. Böswald, H. Haas, K. J. Witte, U. Andiel, J. Bayerl, X. Dong, M. Dreher, K. Eidmann, M. Fischer, M. Hegelich, M. Kaluza, S. Karsch, G. Keller, G. Pretzler, H. Stehbeck, and G. Tsakiris, *Advanced Titanium Sapphire Laser ATLAS* (Max-Planck-Institut für Quantenoptik, Garching, Germany, 2002), No. MPQ-272.
- [110] M. Born and E. Wolf, *Principles of Optics: Electromagnetic Theory of Propagation, Interference and Diffraction of Light*, sixth ed. (Pergamon Press, Oxford, 1980).
- [111] E. G. Loewen and E. Popov, *Diffraction Gratings and Applications* (Marcel Dekker, Inc., New York, NY, 1997).

- [112] *CRC Handbook of Spectroscopy*, edited by J. W. Robinson (CRC Press, Cleveland, OH, 1974), Vol. 1.
- [113] *CRC Handbook of Chemistry and Physics*, 85th ed., edited by D. R. Lide (CRC Press, Boca Raton, FL, 2004–2005).
- [114] B. Dromey, D. Adams, R. Hörlein, Y. Nomura, S. G. Rykovanov, D. C. Carroll, P. S. Foster, S. Kar, K. Markey, P. McKenna, D. Neely, M. Geissler, G. D. Tsakiris, and M. Zepf, “Diffraction limited performance and focusing of high harmonics from relativistic plasmas,” *Nature Phys.* (submitted).
- [115] E. J. Takahashi, H. Hasegawa, Y. Nabekawa, and K. Midorikawa, “High-throughput, high-damage-threshold broadband beam splitter for high-order harmonics in the extreme-ultraviolet region,” *Opt. Lett.* **29**, 507 (2004).
- [116] N. A. Papadogiannis, L. A. A. Nikolopoulos, D. Charalambidis, G. D. Tsakiris, P. Tzallas, and K. Witte, “Two-photon ionization of He through a superposition of higher harmonics,” *Phys. Rev. Lett.* **90**, 133902 (2003).
- [117] P. Tzallas, D. Charalambidis, N. A. Papadogiannis, K. Witte, and G. D. Tsakiris, “Second-order autocorrelation measurements of attosecond XUV pulse trains,” *J. Mod. Opt.* **52**, 321 (2005).
- [118] J. Itatani, F. Quéré, G. L. Yudin, M. Yu. Ivanov, F. Krausz, and P. B. Corkum, “Attosecond streak camera,” *Phys. Rev. Lett.* **88**, 173903 (2002).
- [119] Y. Kobayashi, T. Sekikawa, Y. Nabekawa, and S. Watanabe, “27-fs extreme ultraviolet pulse generation by high-order harmonics,” *Opt. Lett.* **23**, 64 (1998).
- [120] T. Sekikawa, A. Kosuge, T. Kanai, and S. Watanabe, “Nonlinear optics in the extreme ultraviolet,” *Nature* **432**, 605 (2004).
- [121] Y. Nabekawa, T. Shimizu, T. Okino, K. Furusawa, H. Hasegawa, K. Yamanouchi, and K. Midorikawa, “Conclusive evidence of an attosecond pulse train observed with the mode-resolved autocorrelation technique,” *Phys. Rev. Lett.* **96**, 083901 (2006).
- [122] K. Furusawa, T. Okino, T. Shimizu, H. Hasegawa, Y. Nabekawa, K. Yamanouchi, and K. Midorikawa, “Photoelectron spectroscopy of two-photon ionisation of rare-gas atoms by multiple high order harmonics,” *Appl. Phys. B* **83**, 203 (2006).
- [123] Y. Nabekawa, H. Hasegawa, E. J. Takahashi, and K. Midorikawa, “Production of doubly charged helium ions by two-photon absorption of an intense sub-10-fs soft X-ray pulse at 42 eV photon energy,” *Phys. Rev. Lett.* **94**, 43001 (2005).
- [124] R. Trebino, K. W. DeLong, D. N. Fittinghoff, J. N. Sweetser, M. A. Krumbügel, B. A. Richman, and D. J. Kane, “Measuring ultrashort laser pulses in the time-frequency domain using frequency-resolved optical gating,” *Rev. Sci. Instrum.* **68**, 3277 (1997).



- [125] C. Iaconis and I. A. Walmsley, “Self-referencing spectral interferometry for measuring ultrashort optical pulses,” *IEEE J. Quantum Electron.* **35**, 501 (1999).
- [126] A. Kosuge, T. Sekikawa, X. Zhou, T. Kanai, S. Adachi, and S. Watanabe, “Frequency-resolved optical gating of isolated attosecond pulses in the extreme ultraviolet,” *Phys. Rev. Lett.* **97**, 263901 (2006).
- [127] Y. Mairesse and F. Quéré, “Frequency-resolved optical gating for complete reconstruction of attosecond bursts,” *Phys. Rev. A* **71**, 011401(R) (2005).
- [128] E. Cormier, I. A. Walmsley, E. M. Kosik, A. S. Wyatt, L. Corner, and L. F. DiMauro, “Self-referencing, spectrally, or spatially encoded spectral interferometry for the complete characterization of attosecond electromagnetic pulses,” *Phys. Rev. Lett.* **94**, 033905 (2005).
- [129] Y. Mairesse, O. Gobert, P. Breger, H. Merdji, P. Meynadier, P. Monchicourt, M. Perdrix, P. Salières, and B. Carré, “High harmonic XUV spectral phase interferometry for direct electric-field reconstruction,” *Phys. Rev. Lett.* **94**, 173903 (2005).
- [130] G. V. Marr and J. B. West, “Absolute photoionization cross-section tables for helium, neon, argon, and krypton in the VUV spectral regions,” *At. Data Nucl. Data Tables* **18**, 497 (1976).
- [131] A. Saenz and P. Lambropoulos, “Theoretical two-, three- and four-photon ionization cross sections of helium in the XUV range,” *J. Phys. B: At. Mol. Opt. Phys.* **32**, 5629 (1999).
- [132] P. Tzallas, K. Witte, G. D. Tsakiris, N. A. Papadogiannis, and D. Charalambidis, “Extending optical fs metrology to XUV attosecond pulses,” *Appl. Phys. A* **79**, 1673 (2004).
- [133] H. Mashiko, A. Suda, and K. Midorikawa, “All-reflective interferometric autocorrelator for the measurement of ultra-short optical pulses,” *Appl. Phys. B* **76**, 525 (2003).
- [134] E. Hecht, *Optics*, 3rd ed. (Addison-Wesley, Reading, MA, 1998).
- [135] F. Quéré, *Phase properties of high-order-harmonics from plasma mirrors*, Workshop on: “High temporal and spectral resolution at short wavelengths,” (FORTH-IESL, Crete, Greece), 2007.
- [136] F. Quéré, C. Thaury, J.-P. Geindre, G. Bonnaud, P. Monot, and Ph. Martin, “Phase properties of laser high-order harmonics generated on plasma mirrors,” *Phys. Rev. Lett.* **100**, 095004 (2008).
- [137] M. A. Kornberg and P. Lambropoulos, “Photoelectron energy spectrum in ‘direct’ two-photon double ionization of helium,” *J. Phys. B: At. Mol. Opt. Phys.* **32**, L603 (1999).
- [138] T. Nakajima and L. A. A. Nikolopoulos, “Use of helium double ionization for autocorrelation of an xuv pulse,” *Phys. Rev. A* **66**, 041402(R) (2002).

- 
- [139] E. P. Benis, D. Charalambidis, T. N. Kitsopoulos, G. D. Tsakiris, and P. Tzallas, “Two-photon double ionization of rare gases by a superposition of harmonics,” *Phys. Rev. A* **74**, 051402(R) (2006).
- [140] F. Tavella, Y. Nomura, L. Veisz, V. Pervak, A. Marcinkevičius, and F. Krausz, “Dispersion management for a sub-10-fs, 10 TW optical parametric chirped-pulse amplifier,” *Opt. Lett.* **32**, 2227 (2007).
- [141] R Development Core Team, *R: A Language and Environment for Statistical Computing*, R Foundation for Statistical Computing, Vienna, Austria, 2007, ISBN 3-900051-07-0.

# Acknowledgments

Here I would like to thank all the people who helped me during my doctoral study to achieve the results presented in this thesis.

First of all, I would like to thank Prof. Ferenc Krausz for giving me an opportunity to work in his group. The warm atmosphere and the stimulating environment were ideal for doing research as a PhD student.

I would like to thank George Tsakiris for supervising me during my study. He guided me with many thoughtful suggestions from his knowledge and experience, which helped me whenever I had problems. Grateful thanks are due to Rainer Hörlein, with whom I worked all the time, for sharing the burden of the work with me and undertaking an extra task of operating ATLAS laser system whenever we did an experiment. I would also like to thank Sergey Rykovanov for a lot of simulations he has made for our experiments and many valuable discussions.

I appreciate the help from Paris Tzallas and Brendan Dromey during the experiment of temporal characterization. Their passion and experience inspired me in many aspects. I would also like to acknowledge valuable discussions with Dimitrios Charalambidis.

I would like to thank László Veisz, Karl Schmid, and Tibor Wittmann for helping me in the experiment of the plasma mirror in Vienna. Special thanks goes to László Veisz and Karl Schmid, who have helped my life in Europe from the first day I started working in this group.

I am indebted to the members of the ATLAS team, namely Stefan Karsch, Zsuzsana Major, Jens Osterhoff, Andreas Henig, and Antonia Popp, for operating the laser whenever it was needed for the experiment.

I would also like to thank all the people who have helped me in the work not presented in the thesis, especially Franz Tavella, who helped me in every work related to LWS-10 from SPIDER development to the attempt to generate harmonics. The technical help from all the technicians and the workshop staff is also acknowledged.

At this point, I would like to thank George Tsakiris and László Veisz again for reading earlier versions of the manuscript and making many helpful comments to improve it. I would also like to thank Rainer Hörlein for translating the abstract of the thesis into German.

I wish to thank Takao Fuji and Nobuhisa Ishii, who “pioneered” to work in this group as Japanese and aided me many times during my stay in Europe.

I would like to express my gratitude to all the other colleagues, whom I couldn't mention here, for creating an excellent atmosphere to work in this group.

Last but not least, I would like to thank my family for encouraging me to study abroad and helping me any time in any possible way.



# Curriculum Vitae

Yutaka Nomura

## Current address

Max-Planck-Institut für Quantenoptik  
Hans-Kopfermann-Straße 1,  
D-85748 Garching, Germany

E-mail: [yutaka.nomura@mpq.mpg.de](mailto:yutaka.nomura@mpq.mpg.de)

Tel: +49 (0) 89 32905 601

Fax: +49 (0) 89 32905 649

## Personal data

Date of birth: 04. Oct. 1979

Place of birth: Chiba, Japan

Nationality Japan

## Education

### Oct. 2004 – present

Ph.D. student (continued) at Max-Planck-Institute für Quantenoptik, Garching, Germany, and Ludwig-Maximilians-Universität, München, Germany

Thesis: “Temporal characterization of harmonic radiation generated by intense laser–plasma interaction”

Supervisor: Prof. Ferenc Krausz

(Three semesters enrollment at LMU from Summer of 2005 to Summer of 2006.)

**Apr. 2004 – Sep. 2004**

Ph.D. student at Institut für Photonik, Technische Universität Wien, Vienna, Austria  
Supervisor: Prof. Ferenc Krausz

**Apr. 2002 – Mar. 2004**

Master of Science from Department of Physics, Graduate School of Science, the University of Tokyo, Tokyo, Japan  
Thesis: “Control of High-Order Harmonics Generated in Atoms and Molecules”  
Supervisor: Prof. Hirofumi Sakai

**Apr. 1998 – Mar. 2002**

Bachelor of Science from Department of Physics, Faculty of Science, the University of Tokyo, Tokyo, Japan

# List of publications

Publications included in the thesis are marked with \*.

- 1\* R. Hörlein, **Y. Nomura**, J. Osterhoff, Zs. Major, S. Karsch, F. Krausz, and G. D. Tsakiris, “High harmonics from solid surfaces as a source of ultra-bright XUV radiation for experiments,” (submitted).
- 2\* **Y. Nomura**, R. Hörlein, P. Tzallas, B. Dromey, S. Rykovanov, Zs. Major, J. Osterhoff, S. Karsch, L. Veisz, M. Zepf, D. Charalambidis, F. Krausz, and G. D. Tsakiris, “Attosecond phase locking of harmonics emitted from laser-produced plasmas,” (submitted).
- 3 R. Hörlein, B. Dromey, D. Adams, **Y. Nomura**, S. Kar, P. Foster, D. Neely, F. Krausz, G. D. Tsakiris, and M. Zepf, “High contrast plasma mirror: spatial filtering and second harmonic generation at  $10^{19}$  W cm<sup>-2</sup>,” (submitted).
- 4 B. Dromey, D. Adams, R. Hörlein, **Y. Nomura**, S. G. Rykovanov, D. C. Carroll, P. S. Foster, S. Kar, K. Markey, P. McKenna, D. Neely, M. Geissler, G. D. Tsakiris, and M. Zepf, “Diffraction limited performance and focusing of high harmonics from relativistic plasmas,” (submitted).
- 5 F. Tavella, **Y. Nomura**, L. Veisz, V. Pervak, A. Marcinkevičius, and F. Krausz, “Dispersion management for a sub-10-fs, 10 TW optical parametric chirped-pulse amplifier,” *Opt. Lett.* **32**, 2227 (2007).
- 6 **Y. Nomura**, T. Kanai, S. Minemoto, and H. Sakai, “Efficient generation of high-order sum and difference frequencies in the xuv region by combining a weak longer-wavelength field,” *Phys. Rev. A* **75**, 041801(R) (2007).
- 7\* **Y. Nomura**, L. Veisz, K. Schmid, T. Wittmann, J. Wild, and F. Krausz, “Time-resolved reflectivity measurements on a plasma mirror with few-cycle laser pulses,” *New J. Phys.* **9**, 9 (2007).
- 8 A.-J. Verhoef, J. Seres, K. Schmid, **Y. Nomura**, G. Tempea, L. Veisz, and F. Krausz, “Compression of the pulses of a Ti:sapphire laser system to 5 femtoseconds at 0.2 terawatt level,” *Appl. Phys. B* **82**, 513 (2006).